Novel materials and techniques for renewable energy and biosensing applications

by

Yongki Choi

A dissertation submitted to the Graduate Faculty in Physics in partial fulfillment of the
requirements for the degree of Doctor of Philosophy, The City University of New York

2010

This manuscript has been read and accepted for the
Graduate Faculty in Physics in satisfaction of the
dissertation requirement for the degree of Doctor of Philosophy.

Professor Ramzi R. Khuri

Date
Chair of Examining Committee

Professor Steven G. Greenbaum

Date
Executive Officer

Professor Siu-Tung Yau

Professor Raymond Tung

Professor Yuhang Ren
Supervisory Committee

THE CITY UNIVERSITY OF NEW YORK

Abstract

Novel materials and techniques for renewable energy and biosensing applications

by

Yongki Choi

Advisor: Professor Siu-Tung Yau and Professor Ramzi R. Khuri

Ultrasmall (1 nm and 2.8 nm) colloidal silicon nanoparticles behave as electrocatalysts for the electrooxidation of the renewable energy sources such as ethanol, methanol and glucose. Particle-immobilized electrodes show an onset of electrocatalysis occurring at potentials between -0.4 V and 0.05 V vs. Ag/AgCl at neutral pH. Both the onset potential and the strength of electrocatalysis are dependent on particle size. Tafel measurements show that electrooxidation of the fuels is a first order reaction with the transfer of one electron. The electrocatalytic activity of the particles to the fuels undergoes at least a 50-fold increase under alkaline condition compared to under acidic condition. A significant increase in the electrocatalytic current is obtained when the electrocatalysis is performed in darkness. Prototype single-compartment and double-compartment hybrid fuel cells have been constructed and tested, using the particles as the anode electrocatalyst, in order to demonstrate the potential of the particles in fuel cell applications.

Voltage-controlled amplification of the output current of an enzymatic transistor has been demonstrated. By applying external voltage between the gating and the working electrode on which the enzyme glucose oxidase was immobilized, the biocatalytic output current was increased significantly, allowing the detection limit of glucose to be lowered from the milli-molar to the zepto-molar level. The current amplification was reversibly controlled by the applied voltage. Applying this technique to the ethanol-alcohol dehydrogenase system showed similar results. The enzyme's bio-specificity was preserved in the presence of the field. The detector, with its output current controlled by the voltage applied at a third electrode, behaves as a field-effect transistor, whose current-generating mechanism is the conversion of analytes to products using an enzyme as catalyst. In addition, voltage-controlled reaction kinetics of biological catalysis is achieved using the microperoxidase-11 and hydrogen peroxide system. The interfacial electron transfer of the system was manipulated by applying the voltage to the electrode. The manipulated electron transfer causes kinetic parameters of the catalysis to acquire nonlinear dependences on the voltage. The nonlinearity indicates the feasibility of effectively controlling the efficiency of a bio-catalytic reaction or a conversion process using the voltage

Acknowledgments

First, I would like to thank my advisor, Professor Siu-Tung Yau. He taught and encouraged me with his professional guidance, excellent knowledge and patience throughout my research work. I also would like to thank my advisor, Professor Ramzi R. Khuri, for his valuable advice and constant support over the years. I am very grateful to my committee members, Professor Raymond Tung and Professor Yuhang Ren, for their advice and comments on this dissertation.

Next, I would like to thank Professor Munir H. Nayfeh who provided the silicon nanoparticles used in this work and valuable discussion.

Special thanks go to Korea Science and Engineering Foundation (KOSEF) for several years of "Graduate Study Abroad Scholarship" support.

I also would like to acknowledge all of my friends for their academic and personal advice, support and help.

Finally, I would like to thank my parents for their unconditional and unlimited love, support and trust. I am deeply grateful to my brothers, sister and sister-in-law for their love, support and caring of all. I also deeply appreciate JungHee's family including brother-in-law for their strong support and love. Mostly, I would like to thank my wife, JungHee, for her sacrifice, love and support.

Again, I would like to thank every one of you!

Table of Contents

Lists of Tables

Lists of Figures

Chapter 1 Introduction

1.1 Overview

Studies of novel nanoscale materials have been one of the most important and challenging areas in modern technology. Compared to conventional bulk materials, nanoscale materials show unique physical and chemical properties due to their sizes on the nanometer scale [1,2]. Recent advances of nanotechnology have made it possible to utilize nanoscale materials in functional applications and to construct nanoscale devices [2]. It is generally accepted that the solutions to some of the most pressing technological problems exist in nanoscale materials. On the other hand, using conventional means to alter the properties of conventional materials on the nanoscale is an alternative to using nanoscale materials in solving important problems.

In the 21st century, one of the formidable problems facing the world is the impending shortage of petroleum. Presently, renewable energy resources are being investigated for possible complete or partial substitution of petroleum. To utilize renewable energy resources such as organic fuels (ethanol, methanol, etc), new electrocatalysts, especially those with novel properties due to their nanoscale characteristic dimensions, need to be discovered for energy-harvesting applications [3]. The most obvious application of nanoscale electrocatalysts is in the construction of fuel cells. Fuel cells convert chemical energy stored in organic fuels to electrical energy with little harmful emission. Research on improved conventional electrocatalysts and nanoscale electrocatalysts is one of the focused areas in the development of both high-power generation fuel cells for energy source and low-power generation fuel cells for implantable power supply.

The 21st century is the time when people are expected to have a longer life with improved quality. Many diseases that were considered untreatable or could be treated only marginally previously will experience unprecedented development using new approaches. A critical step in the treatment of the diseases is detection of them at their early stage of development. Thus, techniques for detecting small ensembles of molecules will find a spectrum of biomedical applications. In fact, ultrasensitive detection techniques have already been applied to the detection of proteins, the study of Alzheimer's disease [4], bioassay of antibodies [5], the detection of glucose [6], and early detection of many diseases [7]. The ultimate application of the techniques will be in the single-molecule regime. An important requirement for the detection techniques is, in addition to being ultrasensitive, substance selectivity. In this regard, bio-electrochemical sensing appears as a suitable approach. Electrochemical detection using enzymes as sensing elements provides substance selectivity due to the enzyme-analyte interaction. However, the inherent low level of interfacial charge transfer of this detection approach due to the embedment of enzymes' active sites by protein environment creates fundamental limit to the sensitivity of this approach.

1.2 Review of the state-of-the-art of materials and techniques related to dissertation

Pure platinum has been widely used as an electrocatalyst for electrooxidation of renewable energy sources such as methanol, ethanol and glucose in fuel cells. Electrooxidation of ethanol and methanol on the Pt electrode is known to proceed by initial adsorption of fuel fragments on the electrode [8,9]. The peak observed in the anodic current of the cyclic voltammogram is caused by initial electrode poisoning (permanent adsorption) due to adsorption of CO in the low potential range and subsequent oxidation of the Pt electrode at a higher potential [10]. The oxidation of the two fuels on the Pt electrode starts at a high potential of 0.6 V vs. RHE [10-12] in acidic electrolytes. Electrode poisoning makes the catalytic activity of pure platinum inefficient to be useful in fuel cells so that there has been an intensive search for more active materials.

The alloys of platinum with different metals such as Pt/Ru, Pt/Sn and Pt/Ir are used to enhance oxidative activity. To date, Pt/Ru showed the largest effect on the catalysis of the energy sources [12]. The Pt/Ru alloy system provides a bi-functional mechanism, in which the fuel fragments adsorbe on Pt and Ru provides oxygen-containing adsorbates such as OH, which gives rise to oxidative removal of CO at nearby Pt sites at a lower potential (~ 0.4 V vs. RHE), therefore lowering the onset of oxidation [13-15]. It was found that the activity of Pt and Pt/Ru for ethanol and methanol oxidation at room temperature is stronger under alkaline condition than under acid condition [10,11].

Although rare-metal-based fuel cells are commercially available, the high cost of rare metals and their limited supply make this kind of fuel cells economically unviable [16]. One of the frontiers in fuel cell research is to find non-precious-metal catalysts for both anode and cathode catalytic reactions. Two types of catalytic reactions, oxidation reaction of fuels at the anode and reduction reaction of oxygen at the cathode, take place in proton exchange membrane fuel cells. However, Pt as a cathode catalyst shows low catalytic activity of oxygen reduction reaction (ORR), which makes energy conversion inefficient [17]. Substitution of Pt cathodes by alternative non-precious-metal electrocatalysts will not only reduce the cost of fuel cells but will also improve the kinetics of ORR at the cathode to match the fast fuel oxidation at the anode [18]. Therefore, searching alternative materials to replace Pt has been studied to reduce cost and to improve fuel cell efficiency, performance and durability. Pure metal (copper and nickel), metal oxide (TiO_2) and metal alloy (tungsten carbide/tantalum) have been studied for their catalytic activities of ORR [19]. Organo-metallic complexes such as porphyrin complexes are known to catalyze oxygen reduction reaction under physiological conditions. Cobalt, iron or zinc porphyrin complex showed high catalytic activities for reduction of oxygen to water [20]. In addition, a cobalt-polypyrrole-carbon composite synthesized via a simple chemical method is reported as a new class of non-precious-metal composite catalysts showing good activity and remarkable stability of ORR in polymer electrolyte fuel cell [17].

Nanoscale materials with their novel properties such as large specific surface area provide feasibility for catalysis, sensing, and fuel cells. Metal nanoparticles, especially gold and platinum nanoparticles, have been studied for electrocatalytic activity to methanol and carbon monoxide [21]. One of the advantages of the composite nanoscale materials is multi-properties corresponding to each one. A composite electrode consisting of platinum nanoparticles and Nafion polymer has been studied for the catalysis of the oxidation of dopamine [22,23], which is neurotransmitter and has many functions in the brain. In addition, the carbon nanotubes which have remarkable electrical, chemical, and physical properties are used for supporting nanoparticles to make a non-enzyme sensor [24].

Bioelectrochemical detection of substances is usually performed using enzyme-based biosensors, which utilize redox enzymes as electrocatalysts (sensing elements). The enzymes catalyze the electrooxidation of the analytes while providing selectivity for the detection. In a traditional electrochemical glucose sensor, the enzyme glucose oxidase (GOx) is immobilized on an electrode to catalyze the oxidation of glucose with oxygen so that gluconolactone and hydrogen peroxide are produced in this reaction. Then, hydrogen peroxide is oxidized using a platinum electrode to generate an electric current, whose magnitude is proportional to the glucose concentration. This is an indirect glucose-detection method. The sensor shows glucose detection range of 0 ~ 30 mM with a detection limit of 0.4 mM [25] .

Several methods for achieving enhanced detection limit of glucose have been attempted. These methods are based on introducing foreign materials into the enzyme in order to increase the rate of electron transfer. Research efforts have been made in "bridging" the active site to the sensing electrode using foreign materials. A noted example is the insertion of electron relays within an enzyme. By attaching electron relays such as ferrocene to the three dimensional protein structure of the enzyme, a glucose oxidase (GOx), direct transfer of electrons from the active site through the relays to the electrode was observed at glucose detection range of 0 ~ 100 μM with a detection limit of 5 μM [26]. The linear range of glucose detection from 0.01 mM to 1 mM with 5 μM detection limit was obtained in a glassy carbon electrode on which GOx was co-immobilized with a layer of poly p-pherrylenediamine [27]. Also, metal nanoparticles as a mediator were used to connect the active site of GOx and an electrode to enhance electron transfer. The metal nanoparticles assembled electrode showed a glucose detection range of 0.5 ~ 16 mM with a detection limit of 7.0 μM [28]. A 1.4-nm gold nanoparticle was inserted between GOx and a gold electrode. The gold nanoparticle acted as an electron relay or "electrical nanoplug" for the electrical wiring of the active site of the enzyme with wide glucose detection range of 0 ~ 120 mM [29]. An extremely high electron transfer turnover rate of 5000 (electrons generated by one enzyme per second) was obtained.

Since nanoparticles have large specific surface area and compatibility to biomaterials, they are widely used in constructing biosensors. GOx adsorbed on a CdS nanoparticles modified graphite electrode was investigated, where the GOx demonstrated significantly enhanced electron-transfer activity. The detection range of glucose concentration was from 0 to 33.3 mM and a detection limit was 0.05 mM [30]. GOx attached covalently to a gold nanoparticle monolayer modified electrode was fabricated as a glucose sensor and the sensor provide a linear response to glucose the range of 20 μM ~ 5.7 mM and a detection limit of 8.2 μM [31]. An ethanol sensor based on partial sulfonation of sol-gel network with gold nanoparticles and alcohol dehydrogenase showed a linear ethanol concentration range of 5 μM to 5.2 mM with a detection limit of 12 nM [32].

When the nanotubes were inserted into sensing layer, the biosensor performance was enhanced significantly. Single welled carbon nanotubes (CNT) are used as bridge between self assembled monolayer and GOx. This aligned nanotube-enzyme electrode showed the electron transfer turnover rate of 4100 and a glucose detection limit of 5 mM [33]. A glucose biosensor assembled a nano electrode with GOx and CNT detected glucose up to 30 mM with a detection limit of 0.08 mM [15]. An alcohol biosensor based on carbon nanotube/Teflon composite electrodes showed amperometic response to alcohol up to 5 mM with a detection limit of 0.1 mM [34].

1.3 Outline of dissertation

The work presented in this dissertation will discuss nanoscale materials and techniques for renewable energy and biosensing applications.

In chapter 1, we address an introduction and a review of nanoscale materials and techniques for their applications.

Chapter 2 discusses basic theory of electron transfer in biological systems and fundamental background of biosensors and biofuel cells with their characteristics.

Chapter 3 presents that ultrasmall colloidal silicon nanoparticles behave as electrocatalysts for the electro-oxidation of renewable energy sources such as glucose, ethanol and methanol and demonstrates a prototype hybrid fuel cell, using the particles as the anode catalyst, the potentiality of the particles in low-power generation for the biomedical applications. In addition, we discuss an intriguing feature of the particle induced catalysis, which is an unexpected light dependence that a significant increase in the catalytic current is obtained when the catalysis is performed in darkness.

In chapter 4, we present a simple approach to modulate the electron transfer between an active site of enzyme and an electrode without using foreign materials. Additionally, we discuss an enzymatic amplifying bio-detection system with pico molar detection limit and a field induced modulation of electron transfer in relation to the operation of an enzymatic transistor.

In chapter 5, we summarize this dissertation and suggest future studies.

Chapter 2 Electron transfer at electrodes and related applications

2.1 Electrochemistry and electrochemical characterization of electrodes

Since electrochemistry is the technique that has been used in all the experimental work of this dissertation, its principle and application to the characterization of electrodes are briefly outlined.

2.1.1 Voltammetry and amperometry

The conventional electrochemical system consists of an external power supply and three electrodes: the working, the reference and the counter (auxiliary) electrodes. The electrodes are contained in a glass cell, which also contains an ionic solution. When performing voltammetry, the potential of the working electrode versus the reference electrode is varied by external power supply, and the current flowing between the working electrode and the counter electrode is recorded [35].

In linear sweep voltammetry (LSV), the potential E is changed linearly with time (scan rate $v = dE / dt$) meanwhile the current is recorded as a function of potential as shown by the red part of Figure 2.1(a). The red part of Figure 2.1(b) shows a typical current vs. potential curve (i-E) of LSV for adsorbed (immobilized) redox biomolecules system ($O + e^- \rightleftharpoons R$). Figure 2.1(c) shows the energy levels of the electrode and the active site for the adsorbed biomolecules at equilibrium ($E_F = E_{redox}$) where E_F, E_{ox}, E_{red} and E_{redox} are Fermi energy of electrode, most probable energies for the occupied and unoccupied quantum states of the active site, and the standard redox Fermi level defined as $E_{redox} = ½ (E_{ox} - E_{red}) = E^{0}$. When the electrode potential energy approaches the occupied electronic states of the biomolecules (E_{red}) as shown in Figure 2.1(d), electrons can flow from the biomolecules to the electrode, which is the oxidation current (red curve in Figures 2.1(a) and 2.1(b)). The oxidation current is maximized at the $E_F = E_{red}$. After the electrode potential passes E_{red}, the oxidation current decreases because of less probable energy states of the biomolecules.

Scanning the potential in opposite directions is called cyclic voltammetry (CV). The red and blue parts of Figures 2.1 (a) and (b) describe this technique. The CV is one of the most widely used methods in the study of electrochemical reactions. When the electrode potential is reversed after reaching E_{max}, a maximum potential applied, a reduction current flows as shown by the blue parts in Figure 2.1(a) and (b) because the energy level of the electrode is high enough to transfer the electrons to the vacant electronic states of the biomolecules as described in Figure 2.1(e). In the CV, the redox peak current of adsorbed biomolecules system is,

$$i_p = \frac{n^2 F^2}{4RT} vA\Gamma \qquad (2.1)$$

where n, F, R, T, A and Γ is number of electron transferred, Faraday number, temperature, gas constant, working electrode area and surface concentration of adsorbed biomolecules, respectably [35]. Instead of sweeping the electrode potential, chronoamperometry (i-t) technique records the current as a function of time at a constant electrode potential. This technique is useful for catalyst and biosensors studies.

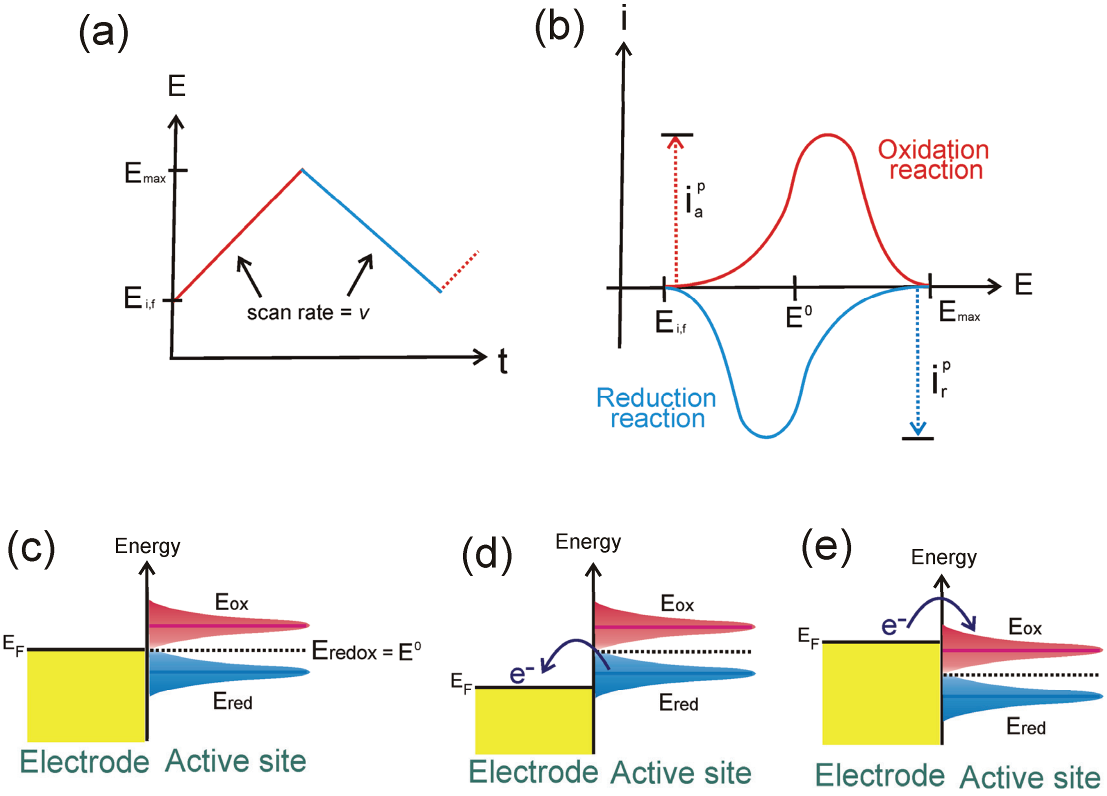

Figure 2.1 Cyclic voltammetry and its corresponding electron transfer (a) Cyclic potential sweep from E_i to E_{max} then to E_f as function of time with constant scan rate, $v = dE/dt$. E_i, E_f and E_{max} are initial, final and maximum potential. (b) Cyclic voltammograms of (a). Red curve is oxidation current generated by oxidation reaction during $E_i \sim E_{max}$ and blue curve is reduction current generated by reduction reaction during $E_{max} \sim E_f$. $i^p{}_a$ and $i^p{}_r$ are oxidation and reduction peak current. (c) Energy level of the electrode and the most probable energies for the occupied and unoccupied states of active site for the biomolecules at equilibrium (d) Oxidation reaction (current) occurs when the electrode energy is lower than the occupied energy states of the biomolecules. (e) Reduction reaction occurs when the electrode energy is higher than the unoccupied energy state of the biomolecules.

2.1.2 The electrical double layer and charging current

The contribution of the electrode-solution interface to the measured electrochemical current should be described for the characterization of an electrode. The electrical double layer is formed at the interface between the electrode and electrolyte (ionic) solution due to distribution of charge (segregation of positive and negative charges) and electrical potential [35]. Figure 2.2 is a schematic model of the double layer showing the ions, charge and potential distribution [36]. When a negative potential is applied to the metal electrode, the negative charges and positive ions or molecules will be accumulated at the metal side and the solution side, respectively. On the solution side of the electrical double layer, there are several layers. The inner Helmholtz plane (IHP) consists of the ions or molecules that are specifically adsorbed. The freely moveable ions or molecules can approach to the electrode by long range electrostatic force out of the inner layer, forming the outer Helmholtz plane (OHP) [35]. Diffusion layer is defined from OHP to the bulk solution where the nonspecifically adsorbed ions are distributed in the solution. The electrical double layer behaves like a capacitor with capacitance C_d which is generally a function of potential [37]. The charging current i_c of the double layer capacitor initiated by the potential step E is,

$$i_c = \frac{E}{R_s}\exp(-t / R_s C_d) \qquad (2.2)$$

where E is the potential step width and R_s is the solution resistance. Therefore, the total current measured is made up of the charging current and the faradaic current. The faradaic current is the current generated by the electron transfer of oxidation or reduction reaction of reactants at the working electrode. The electrode reaction to reactants is faster than the supply by diffusion of the reactants from bulk solution. For one dimensional linear diffusion case at a planar electrode, the faradaic current is,

$$i_f = \frac{nFAD_o^{1/2}C_o}{\pi^{1/2}t^{1/2}} \qquad (2.3)$$

where n, F, A, C_o and D_o are number of electron transferred, Faraday number, working electrode area, bulk concentration and diffusion constant, respectably [37]. From Equations 2.2 and 2.3, the charging current decreases exponentially while the faradaic current decreases according to $t^{-1/2}$. Thus, the contribution of charging current effect in the measured current is neglected by measuring the current at a sufficiently long time after the potential step, where the charging current has largely decayed, whereas the faradaic current is still significant [37,38].

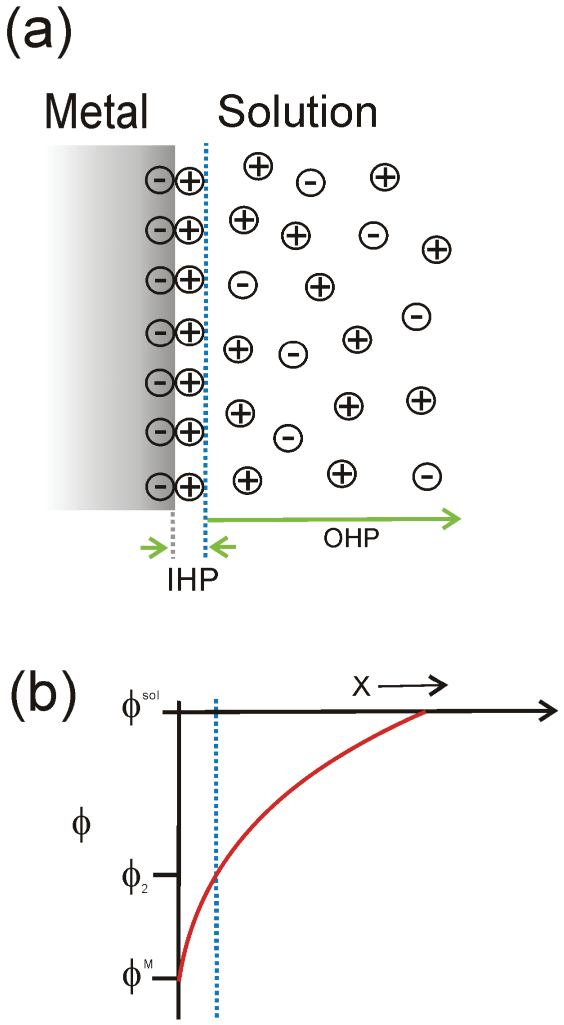

Figure 2.2 Charge and ion distribution at the interface of an electrode and an electrolyte (a) Electrical double layer formed by IHP on which ions and molecules are adsorbed and OHP in which freely movable ions and molecules are distributed. (b) Potential profile across the electrical double layer of (a) where ϕ^M, ϕ_2 and ϕ^{sol} are potential at a metal electrode, potential at IHP and potential in bulk solution after IHP, respectively.

2.2 Electron tunneling between two electrodes (FN theory)

Electron tunneling between two metal electrodes through an insulator (tunnel/energy barrier) is described by the Fowler-Nordheim theory (FN theory) [39]. In the context of tunneling in biomolecules (see section 2.3), the two electrodes can be considered as a donor and acceptor pair in the biomolecular system. At the interface between an electrode and a biomolecule, one electrode corresponds to the redox center of the molecule. Electronic tunnel current can flow through the insulating region between the two electrodes if the barrier is thin enough to permit the penetration of electron wavefunctions [40]. Figures 2.3(a) and 2.3(b) show the energy band diagrams of the FN tunneling for two different energy barriers. The first barrier is a trapezoidal formed at intermediate voltage range ($0 < V < \Phi_B/e$) as shown Figure 2.3(a) and the second is a triangular formed at high biasing voltage range ($V > \Phi_B/e$) as shown Figure 2.3(b). The tunnel current density for the triangular shape tunnel barrier is,

$$j = \frac{e^3F^2}{8\pi h\Phi_B}\exp\left[-\frac{8\pi\sqrt{2m\Phi_B^3}}{3heF}\right] \tag{2.4}$$

where e, m, Φ_B and F are the electron charge, the electron effective mass, effective tunnel barrier height and the electric field, respectively [41]. Equation 2.4 shows that when the barrier height is high, the tunneling current decreases based on the relation $j \propto \Phi_B^{-1}\times\exp(-\Phi_B^{3/2})$ [42]. For the trapezoidal tunnel barrier as shown Figure 2.3(a), the current density is

$$j = \frac{e}{2\pi h d^2}\left\{\Phi_B^- \exp\left[-\frac{4\pi d\sqrt{2m\Phi_B^-}}{h}\right] - \Phi_B^+ \exp\left[-\frac{4\pi d\sqrt{2m\Phi_B^+}}{h}\right]\right\} \quad (2.5)$$

where V is voltage across barrier, d is distance between two electrodes, and $\Phi^+_B = (\Phi_B + eV/2)$ and $\Phi^-_B = (\Phi_B - eV/2)$, respectively [43]. In addition, the current density at very low voltage range ($V \approx 0$) is

$$j = \frac{3\sqrt{2m\Phi_B}e^2V}{2dh^2}\exp\left[-\frac{4\pi d\sqrt{2m\Phi_B}}{h}\right] \qquad (2.6).$$

Thus, electron tunneling between two metal electrodes through thin insulating tunnel barrier takes place at any energy levels of electrodes [43].

The metal/insulator tunnel junction transistor (MITT), a novel tunneling device, is one example of real physical devices utilizing FN tunneling [44]. A cross sectional view of the MITT is schematically shown in Figure 2.3(c). In the MITT, the source and drain are metals instead of doped semiconductors. A nanometer scale insulating region, the tunnel barrier, is formed between metal source and drain electrodes. On the top of tunnel barrier, a metal gate electrode is formed over a gate insulating film. A gate voltage (V_G) is applied between the gate and the source electrode. In the absence of a gate electrode, the MITT is just a simple metal/insulator/metal diode. The tunnel current between source and drain through the tunnel barrier in the absence of gate voltage ($V_G = 0$) follows FN theory, $j \propto \Phi_B^{-1} \times \exp(-\Phi_B^{3/2})$. However, when the gate voltage is applied, the electric field generated by gate voltage lowers (or raises) the effective tunnel barrier height between source and drain, so that the tunnel current is modulated by the gate voltage as shown Figure 2.3(d) [45].

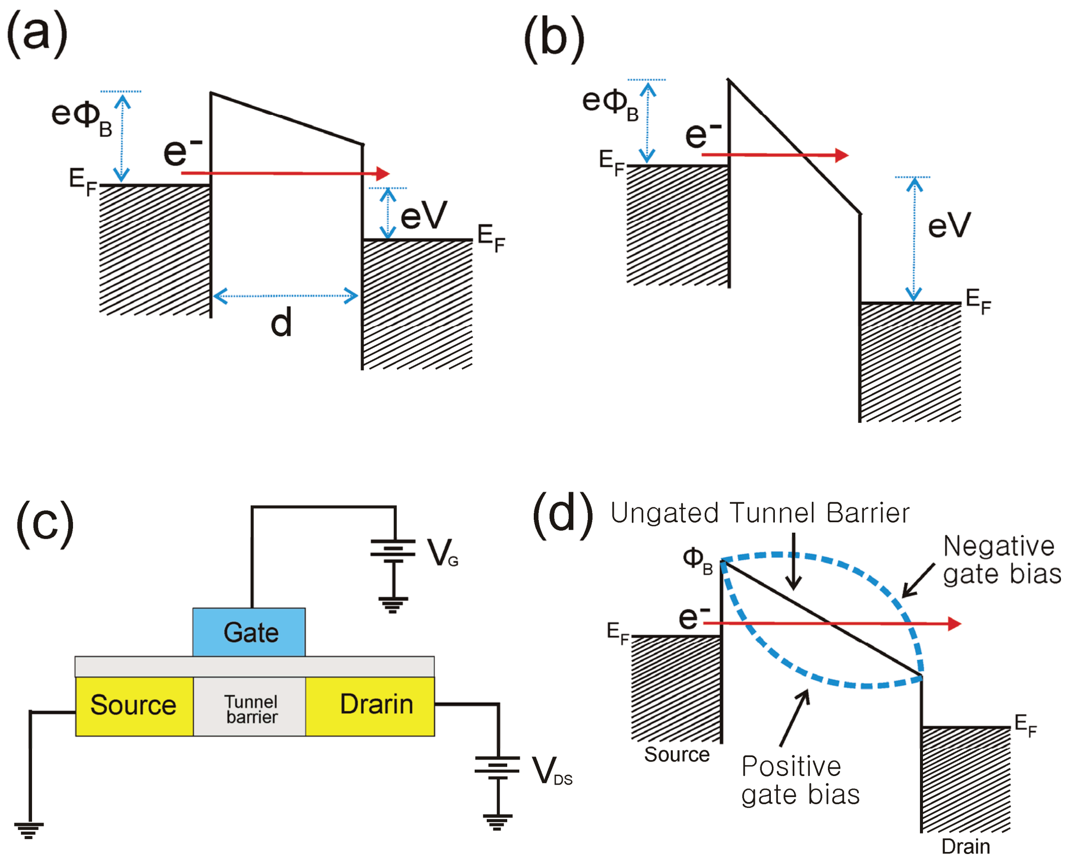

Figure 2.3 Schematic diagram of energy barrier. (a) Trapezoidal shape tunnel barrier when the metal electrodes are at intermediate voltage range ($0 < V < \Phi_B/e$). (b) Triangular shape tunnel barrier when the metal electrodes are at high voltage range ($V > \Phi_B/e$). (c) Schematic diagram of metal/insulator/metal tunneling transistor. (d) Electric field generated by the gate voltage lowers (or raises) the tunnel barrier height (Φ_B) between the source and the drain, so that the tunnel current is modulated by the gate voltage.

The potential profile of MITT can be calculated by solving Laplace's equation ($\partial^2\phi/\partial x^2 + \partial^2\phi/\partial y^2$) due to the absence of space change. With appropriate boundary conditions, the potential profile is shown in Figure 2.3(d), where Φ_B and E_F refer to the barrier height and the Fermi level energy, respectively [45]. When a positive or negative voltage is applied to the gate electrode, the potential profile should be distorted by the electric field from the gate electrode as shown in Figure 2.3(d). The band profile inside the insulator is changed as shown by the dashed curve by the applied gate voltage. Thus, the variation in the band profile near the source electrode changes the tunneling probability for electrons through the potential barrier.

2.3 Electron tunneling in biological system (Marcus theory)

One of the most important aspects of biology and biochemistry is electron transfer reactions. Biological phenomena such as respiration, photosynthesis and metabolism depend on electron transfer reactions between donors and acceptors pair through insulating protein networks [46]. Electron transfer in biological systems is described by the formalism of long-range electron transfer (LRET), which occurs over a distance on the order of 10 Å [47]. Recently, it was proposed that, by controlling the rate of LRET in metabolic systems using certain chemical reactions, metabolism can be regulated to avoid detrimental effects [48]. In bioelectronics, fast direct transfer of electrons between active centers of enzymes and electrodes is required for effective operation of biosensors and biofuel cells [49].

The rate constant of electron tunneling in weakly coupled donors and acceptors pair is,

$$k_{et} = \frac{2\pi}{\hbar} V_d^2 (FC) \qquad (2.7)$$

where V_d is electronic coupling factor, *FC* is Frank-Condon nuclear factor associated with the activated nuclear process, and ← is Plank's constant [50]. The V_d falls off with the term exp($-\beta d$), where d is the distance through the insulating barrier between a donor and an acceptor and β is the attenuation coefficient which is proportional to the square root of the tunnel barrier height ($\beta \propto (\Phi_B)^{1/2}$) [50,51]. The rates reach their maximum values when *FC* is optimized so that the rate constant depends only on V_d [46]. Thus, the overall rate of electron tunneling falls off exponentially with d and β ($k_{et} \propto \exp(-\beta d)$). The rate is significantly modulated by the intervening medium such as electron tunneling between covalently bridged redox centers in synthetic systems [52] and electron tunneling through vacuum [47]. In particular, the pathway model in the protein medium describes that the rate constant is proportional to the coupling strength along the dominant through-bond and through-space coupling routs for electrons from donor to acceptor [53].

Figure 2.4(a) represents classical view of free energy changes during reaction described by Marcus theory [51], showing overlap of harmonic oscillator, where ΔG^0 is the free energy change between the reactants on the left and the products on the right, ΔG^* is the activation energy and λ is reorganization energy. A key aspect of Marcus theory is ΔG^* and its parabolic dependence on ΔG^0 and λ. In the Figure 2.4(a), two parabolas represent the energy of the reactant as the nuclei moved around and the energy of the product as the nuclei moved around. Due to the harmonic oscillator wavefunctions (a parabola), the energy is proportional to the square of the distance from their equilibrium positions. The reactant and the product have different equilibrium nuclear positions because the charge on the atoms or molecules changes in electron transfer reaction. The change of free energy, ΔG^0, is the energy it would take to force the reactants (on the left) to have the same nuclear configuration as the products (on the right) without the electron transfer. Thus, Equation 2.7 can be rewritten as,

$$k_{et} = \frac{2\pi}{\hbar} V_R^2 \frac{1}{\sqrt{4\pi\lambda RT}} \cdot \exp[-(\Delta G^0 + \lambda)^2 / (4\lambda RT)] \qquad (2.8)$$

where R and T are gas constant and temperature, respectively [51]. As mentioned above, V_d decreases exponentially with distance, so Equation 2.8 can be rewritten as,

$$k_{et} = k_0 \exp(-\beta d) \cdot \exp[-(\Delta G^0 + \lambda)^2 / (4\lambda RT)] \qquad (2.9)$$

where k_0 is a reassigned constant, and d is distance between the molecule or group that donates the electron and the one that accepts it. From Equation 2.9, the overlap of the reactant and the product will be maximal when $-\Delta G^0$ equals λ. Experiments show Gaussian dependence of electron transfer rates on $-\Delta G^0$ [51]. The rate constant reaches a maximum when $-\Delta G^0 = \lambda$ and falls with $-\Delta G^0$ values greater than λ. Therefore, the overall rate constant of electron tunneling falls off exponentially with a electron tunneling distance and a tunneling barrier height ($k_{et} \propto \exp(-\beta d)$) when the free energy is optimized. When the quantum mechanics is used to an idealized potential barrier between two metal electrodes separated by tunneling barrier with a biased voltage, β equals $(2/\hbar)(2m\Phi_B)^{1/2}$ in relation to electron tunneling through vacuum, where m is the mass of the electron, Φ_B is the height of the potential barrier [51,54]. Since the electrode and the enzyme redox center can be considered as donors and acceptors pair, in Figure 2.4(b), the protein shell between enzyme redox center and electrode corresponds to tunnel barrier.

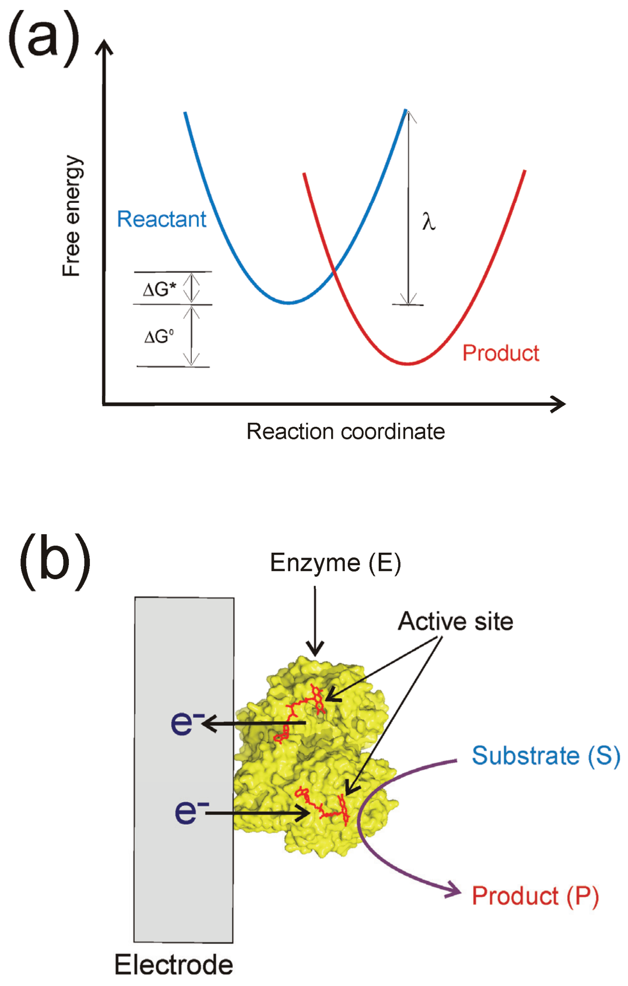

Figure 2.4 Electron transfer reaction. (a) ΔG^0 is the free energy change between the reactants on the left and the products on the right. ΔG^* is the activation energy and λ is reorganization energy. The change of free energy, ΔG^0, is the energy that would take to force the reactants to have the same nuclear configuration as the products without the electron transfer. (b) Electron transfer in biomolecular system, an enzymatic biosensor. An electrode and the active center of an enzyme are considered as a donor and acceptor pair in this enzymatic biosensor. The red color structure (FAD) in the yellow color enzyme (GOx) is the active center.

2.4 Principles of Biosensors

2.4.1 Structures of Biosensors

A biosensor, a device used to detect substances, consists of biological sensing elements, a transducer and associated electronics. The sensing elements are immobilized on the transducer to convert a biological response to a measurable signal, which is sent to the electronics for processing. Enzymatic electrochemical biosensors detect chemical and biological substances (analytes) using biological sensing elements such as enzymes to produce an electric signal as shown in Figure 2.4(b). There are critical performance factors for biosensors such as selectivity, sensitivity, and time factor [55]. The selectivity to only the analyte is the most essential one and the sensitivity is important in relation to concentration range of detection and detection limit. The response, recovering and life time of the biosensors are also desirable for reliable biosensors.

In order to make a practical biosensor, the biological sensing elements such as enzymes have to be properly attached to an electrode by means of immobilization. Many physical and chemical approaches have been used to immobilize biomolecules onto electrodes. As one of the simplest approaches, adsorption is used via the formation of van der Walls interaction, hydrodynamic interaction, electrostatic interaction, hydrogen bond, or chemical adsorption [56]. Adsorbed biomolecules are very sensitive to pH, temperature, and ionic strength. The biomolecules can also be entrapped and then polymerized to a gel by being mixed with conducting polymers such as polyacrylamide, polypyrroles and polyaniline [56]. Covalent bonding between a function group in the biomolecules and the modified electrode is designed as alternative method [57].

2.4.2 Biological recognition and enzyme kinetics

The major advantage of the biosensor is the biological recognition of a particular analyte. Basically, an enzyme interacts with (recognizes) only one substance (its substrate). The enzyme is used as the sensing element, the main biological component, of a biosensor. Thus, the enzyme provides the sensor's selectivity. The enzymes used in electrochemical enzymatic biosensors are redox enzymes, which give rise to reduction and oxidation chemical reactions when immobilized on electrodes. Redox enzymes contain prosthetic molecular complexes, called cofactors, which are responsible for the catalytic activities of the enzymes [58]. Cofactors are simple inorganic metal ions such as Mg^{2+} and Fe^{2+} or complex organic molecules such as coenzyme flavin adenine dinucleotide (FAD) and nicotinamide adenine dinucleotide (NAD).

The kinetics of a typical enzymatic catalysis mechanism is,

$$S + E \underset{k_{-1}}{\overset{k_1}{\rightleftharpoons}} SE \xrightarrow{k_2} E + P \qquad (2.10)$$

where S is the substrate (or the analyte), E is the enzyme (or the catalyst), ES is the enzyme-substrate complex, and P is the product [59]. Assuming that the concentration of SE remains constant during the steady state while the concentrations of S and P change substantially, the rate of the formation of the complex (k_1[S][E]) is balanced by the rate of its breakdown back to enzyme and product ($-k_{-1}$[SE] + k_2[SE]) [59]. From Equation 2.10, the velocity of the formation of E and P from SE is v = d[P]/dt = k_2[SE]. By setting $K_m = (k_{-1} + k_2) / k_1$, where K_m is the Michaelis constant, we obtain following equation

$$\frac{1}{v} = \frac{K_m}{V_{\max}} \frac{1}{[S]} + \frac{1}{V_{\max}} \qquad (2.11).$$

where V_{max} is the maximum value of v. This is known as a Lineweaver-Burk equation (plot) [59,60], i.e. when $1 / v$ is plotted versus 1 / [S], a straight line is obtained with a slope of K_m / V_{max} and an intercept of $1 / V_{max}$. Hence, both K_m and V_{max} can be determined from the plot. The K_m has the dimensions of a concentration (M) and is the substrate concentration at which the velocity is half maximum ($v = V_{max} / 2$). In addition, the K_m value also implies the concentration of [S] required for significant catalysis to take place. The turnover number of constant, $k_{cat} = V_{max}$ / [E_0], is the maximum number of molecules of substrate that could be converted to the product each second per active site where [E_0] is total concentration of enzyme. The k_{cat} implies the enzyme activity when all active sites of enzymes are occupied with substrate because the maximum rate is obtained at high substrate concentrations. In addition, the ratio k_{cat}/K_M is called as the specificity constant providing a measure of how rapidly an enzyme can work at low [S].

2.5 Fuel cells and biofuel cells

2.5.1 Fuel (biofuel) cell principles, systems and applications

A fuel cell is a device that converts chemical energy stored in fuels to electrical energy. In a conventional two-compartment fuel cell, the anode compartment is separated from the cathode compartment by a permeable membrane, through which ions can pass through. The oxidation of the fuel occurs at the anode and the reduction of an oxidant such as oxygen occurs at the cathode [61]. The anode and the cathode are connected through an external wire. The electrons by the oxidation of fuels at the anode flow to the cathode through external circuit, as shown Figure 2.5(a).

Inorganic and organic electrocatalysts are used for the anode and cathode reactions. In direct alcohol fuel cells, the anode oxidizes methanol or ethanol using platinum based alloys according to

$$CH_3OH + H_2O + (\text{Pt or Pt/Ru as anode}) \longrightarrow CO_2 + 6H^+ + 6e^- \quad (2.12)$$

$$3/2O_2 + 6H^+ + 6e^- + (\text{Pt or Pt/Ru as cathode}) \longrightarrow 3H_2O \quad (2.13)$$

For biofuel cells, enzymes are used as electrocatalysts based on their redox reactions. For example, the reaction of a biofuel cell consisted of a GOx/PQQ immobilized anode and a COx/Cytc immobilized cathode with glucose and oxygen as the fuel and the reducing agent, respectively, is

$$\text{Glucose} + (\text{GOx/PQQ at anode}) \longrightarrow \text{Gluconic acid} + 2H^+\ 2e^- \quad (2.14)$$

$$1/2O_2 + 2H^+ + 2e^- + (\text{COx/Cytc at cathode}) \longrightarrow H_2O \quad (2.15)$$

where PQQ, COx and Cytc are pyrroloquinoline quinone, cytochrome c oxidase and cytochrome c, respectively [62]. There are several advantages for the biofuel cells to be developed. One is that the biofuel cells operate at room temperature and near neutral pH. The biological electrocatalysts, enzymes, lower the cost of the biofuel cells to less than that of precious-metal electrocatalysts. In addition, due to enzymes' excellent selectivity to the specific substrates, the fuel and the oxidant can be contained in a single compartment without using membrane to separate them. These features allow us to miniaturize the biofuel cells for implantable power source and biomedical applications [63].

2.5.2 Characteristics of biofuel cells

The overall chemical reactions in the biofuel cells are described thermodynamically by Gibbs free energy [64]. In general, the cell voltage of biofuel cells is simply described as,

$$E_{cell} = \mathrm{OCV} - IR_{int} \qquad (2.17)$$

where IR_{int} is the sum of all internal losses of the biofuel cell, which is proportional to the generated current and internal resistance of the system (R_{int}) [64]. An open circuit voltage (OCV) is a maximum cell voltage that can be measured without flowing current through the external circuit as shown in Figure 2.5.

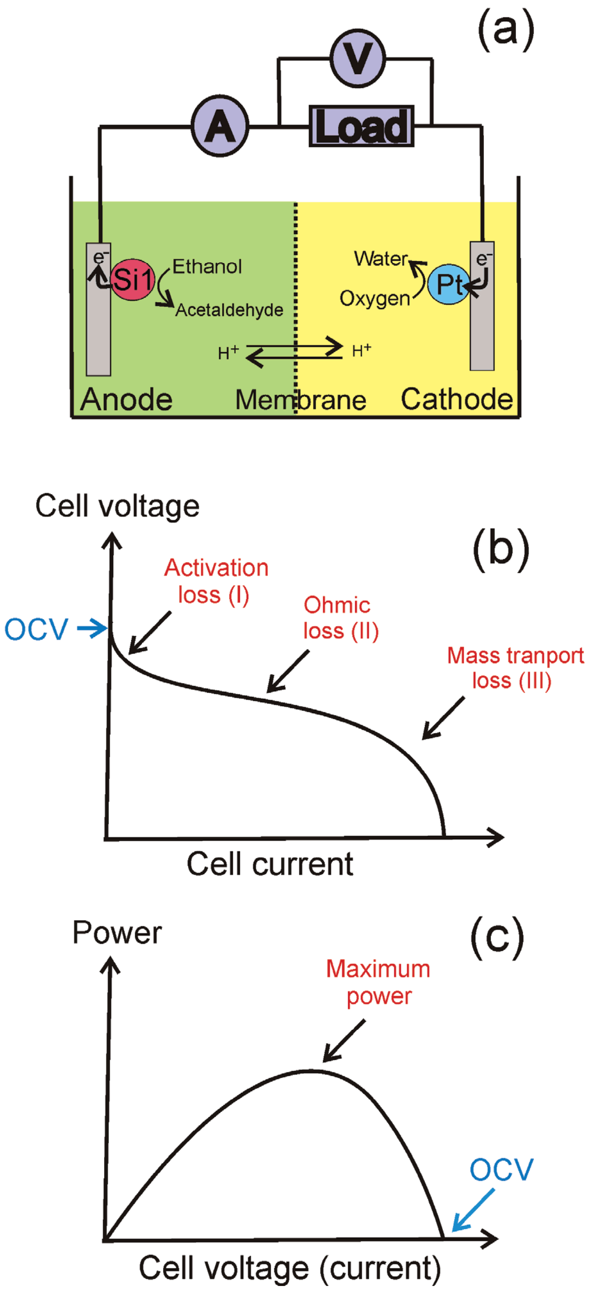

Figure 2.5 Characteristics of (bio) fuel cell (a) Double compartments fuel cell. Ethanol is oxidized to acetaldehyde at silicon nanoparticle-carbon anode and oxygen is reduced to water at platinum-carbon electrode where hydrogen ions are freely passing through membrane. (b) Polarization curve (I-V) showing activation, ohmic and mass transport loss region. The open circuit voltage (OCV) is the maximum cell voltage that can be measured without flowing current through the external circuit. (c) Power curve as a function of cell voltage or cell current. After OCV, power reaches its maximum which is defined as the maximum extractable power of the biofuel cell. Then, power decreases to zero due to ohmic losses and electrode overpotentials.

The polarization curves of biofuel cells, which represent the cell voltage as a function of the cell current, can be obtained by measuring the cell voltage using multi-meter with variable external resistances (IR_{ext}). The voltage is converted to the current by Ohm's law ($I = E_{cell} / R_{ext}$). A typical polarization curve is presented in Figure 2.5(b) with various potential loss factors such as activation, concentration, and ohmic overpotentials [63,65]. Due to lack of electrocatalysis at below activation energy, the activation losses occur during oxidation and reduction reaction at the electrode surface in the region (I). The linear potential drop due to ohmic losses in the fuel cell involves the resistance in solution or electrolytes between anode and cathode as shown in the region (II). Concentration losses take place in the region (III) due to mass transport limitation caused by the diffusion limitation of fuels, which is slower than catalytic reaction. In addition, other factors such as slow electron transfer rate and coupling of mediators can lead to less cell potential as well. With all losses the overall polarization curves are generally of linear shape.

The overall performance of biofuel cells is estimated by power,

$$P = IE_{cell} = E^2_{cell} / R_{ext} \qquad (2.18).$$

The power curve shows the power as a function of the current or the cell voltage as shown in Figure 2.5(c). Power is zero at the OCV condition because no current flows. After OCV, power reaches its maximum with current, which is defined as the maximum extractable power of the biofuel cell [64]. Then, power decreases to zero due to ohmic losses and electrode overpotentials at the short circuit condition [65].

2.6 Importance of electrocatalysts in relation to electron transfer

Study of improved electrocatalysts and new electrocatalysts is one of the key areas in the development of bioelectronic devices and their applications. The basic requirements for bioelectrocatalysts, in addition to selectivity and life time, also include effective electron transfer between electrocatalysts and electrodes for efficient energy conversion [55]. Enzymes, most widely used as electrocatalysts, provide high selectivity for their substrates. However, the disadvantages of enzymes as electrocatalysts are as follows [63]. First of all, the active site of enzymes is buried in the insulating protein matrixes so that electron transfer between the active site and electrodes is ineffective. Foreign materials are used as intrinsic electron relays or extrinsic mediators in the protein to overcome the barrier of electron tunneling at the interface [66]. These techniques rely on foreign materials whose selection is limited by the redox potential of enzymes and by other important factors such as stability, toxicity and biocompatibility. Second, enzymes tend to denature (to lose their bio-activities) under non-native conditions such as high temperature and acidic or alkaline pH values due to their inherent instability. Therefore, long-term applications using enzymes as electrocatalysts are unrealistic [67]. Third, enzymes are still expensive due to the fact that they need to be extracted from nature. So, new electrocatalysts with better electron transfer ability, much longer life-time and low production cost are urgently needed in the area of biomedical and energy-harvesting applications.

Chapter 3 Ultrasmall silicon nanoparticles as electrocatalysts

3.1 Introduction

Discovering novel nanoscale electrocatalysts is presently a frontier in material research. Nanoscale electrocatalysts with novel properties provide improved device performance for sensing and fuel cell applications. Nanoparticles of noble metals such as gold have been studied and showed high electrocatalytic activity for oxidation of methanol and carbon monoxide [21]. Copper nanoparticles used with carbon nanotubes exhibited electrocatalytic activity to various carbohydrates including glucose [68]. A nanocomposite composed of carbon nanotubes and platinum-lead alloy nanoparticles is used as a sensing element for glucose sensor [69]. A Nafion and nanostructured platinum composite coated on a carbon electrode showed electrocatalytic activities to dopamine [23].

An important area of application for nanoscale electrocatalysts is the construction of low-power micro-direct alcohol fuel cells that have recently gained significant attention due to the explosive growth of portable and wireless consumer electronics over the past few years [70]. Micro-fuel cells are expected to deliver power from milli-watt level to a few watts [71]. An area with great potential that exists at the low-end of micro-fuel cells is the implantable power supply for biomedical applications [72]. For implantable applications, the enzyme-based biofuel cell is envisaged to use physiologically ambient glucose as fuel to power implanted biomedical devices such as cardiac pacemakers [73] and artificial hearing [74] and vision devices [75]. A typical power level of ~ 1 μW is required for the operation of the cardiac pacemaker [76]. An important requirement for implantable fuel cells is the adaptation of the single-compartment (membrane-less) configuration, which relies on the selectivity of the electrocatalysts used as the anode and the cathode. For this reason, enzymes are used as electrocatalysts for implantable fuel cells due to their selectivities for their substrates. However, enzymes become unstable under the non-native conditions of the fuel cell environment, making long-term implanted applications unattainable [77]. In a recent study, we have demonstrated that ultrasmall silicon nanoparticles behave as an electrocatalyst for the oxidation of glucose [78,79]. The particles, compared to the enzyme GOx, showed fast substrate conversion kinetic characteristics and particle-immobilized electrodes exhibited stable long-term current output.

In this chapter, we show that colloidal ultrasmall silicon nanoparticles behave as an electrocatalyst for the electrooxidation of renewable fuels, namely, ethanol, methanol and glucose. Electrochemical characterization using voltammetric techniques shows that the onset of the electrocatalysis occurs between -0.4 V and 0.0 V vs. Ag/AgCl (between 0.21 V and 0.61 V vs. RHE) at neutral pH. Chronoamperometric (i-t) measurements were performed to differentiate the oxidation current from charging current in the reaction. Both the onset potential and the strength of electrocatalysis are dependent on particle size. Tafel measurements show that electrooxidation of the fuels is a first order reaction with the transfer of one electron. The nanoparticle-catalyzed oxidation of the fuels has been studied under acidic and alkaline conditions. It was found that the electrocatalytic activity undergoes at least a 50-fold increase under alkaline condition compared to under acidic condition. An intriguing feature of the particle-induced electrocatalysis is an unexpected light-dependence of the electrocatalytic current. A significant increase in the electrocatalytic current is obtained when the electrocatalysis is performed in darkness.

To demonstrate the potential of the particles in fuel cell applications, we have used the particles as the anode catalyst to construct prototype fuel cells. The first prototype fuel cell was a double-compartment direct ethanol fuel cell. Pt particles were used as the cathode catalyst for the reduction of oxygen. The second prototype is a single-compartment hybrid biofuel cell which requires only one fuel (or oxidizer), glucose, for both electrodes. The third is a single-compartment hybrid biofuel cell, which operated on two fuels, glucose and hydrogen peroxide (H_2O_2). The enzyme horseradish peroxidase (HRP) or microperoxidase-11 (MP-11) was used as the cathode catalyst. The long-term stability of the cell was characterized by monitoring the cell voltage for 5 days. A comparison between the hybrid cell and a glucose-based biofuel cell shows that the hybrid cell provides a much better performance in terms of output power density and stability presumably due to fast kinetics and the robustness of the silicon nanoparticle.

3.2 Experimental

3.2.1 Materials and electrodes

Silicon nanoparticles

The silicon nanoparticles were made by electrochemical etching of a (100)-oriented p-type (1~10 Ω-cm) silicon wafer in hydrofluoric acid and hydrogen peroxide. The silicon wafer anode, placed at a certain distance from a platinum cathode, was anodized with a constant current (150 mA) while being vertically immersed in the etchant at a reduced speed of ~1 mm per hour. The anodized wafer was then transferred to an ultrasound bath containing either water or organic solvents such as benzene, isopropyl alcohol or tetrahydrofuran (THF) for a brief treatment, which resulted in crumbling of particles from the wafer into the solvent to form a colloid suspension [80]. This etching technique can be used to prepare 1-nanometer particles (Si1) and 2.8-nanometer particles (Si2.8), depending on etching conditions. The hydrogen atoms passivate the silicon so that subsequent oxidation of silicon is prevented. The silicon nanoparticles used in this work were either provided by Prof. Munir Nayfeh group at University of Illinois at Urbana-Champaign or purchased from NanoSi Advance Technology (Illinois, USA). Monte Carlo simulation of the Si1 particle suggests a filled fullerene structure of $Si_{29}H_{24}$, in which a central core silicon atom and four other silicon atoms are arranged in a tetrahedral coordination and the 24 remaining silicon atoms undergo a H-terminated bulk-like (2×1) reconstruction of dimer pairs on (001) facets (6 reconstructed surface dimers) [81]. The particles exhibit interesting optical properties such as luminescence in the visible part of the spectrum [80], second harmonic generation [82] and laser oscillation [83]. Under UV excitation, the Si1 particle generates blue spontaneous emission with a measured band-gap of 3 eV and the Si2.8 particle generates red emission with a 2 eV band-gap [81]. Figure 3.1(a) shows the spontaneous emission of the two kinds of silicon particles. Figures 3.1(b) is schematic model of Si1, showing the hydrogen passivation of the particle. Figure 3.1(c) and 3.1(d) are the electron micrographs of the particles.

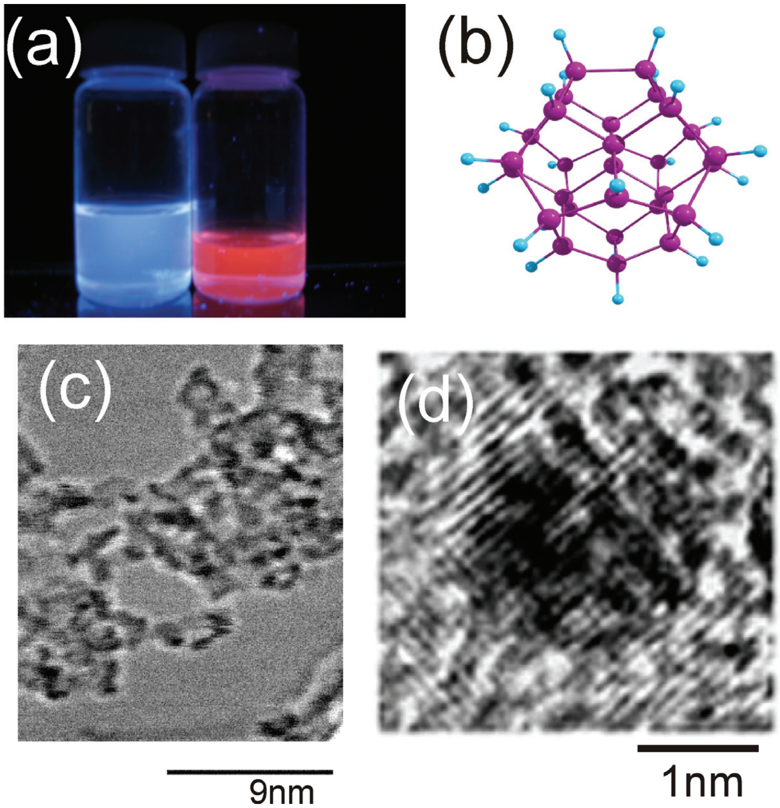

Figure 3.1 The 1 nm and 2.8 nm silicon colloidal nanoparticles (a) When excited by UV radiation, the 1 nm particle emits blue light and the 2.8 nm particle emits red light. (b) Schematic description of the 1 nm particle. The purple and blue spheres represent the silicon atom and the hydrogen atom, respectively. (c) Electron micrograph of the 1 nm silicon particles. Each dark region has a size of 1 nm, indicating a single particle. (d) Electron micrograph of a single 2.8 nm particle.

Glucose oxidase (GOx)

GOx, an enzyme, catalyzes the oxidation of glucose to glucono lactone. GOx molecule is a dimer consisting of two monomers, each of which contains a flavin adenine dinucleotide (FAD), the active site of the molecule as shown in Figure 3.2(a). The dimensions of the GOx monomer and dimer are 60 Å × 52 Å × 37 Å and 60 Å × 52 Å × 77 Å, respectively [84]. GOx, having an isoelectric point (IEP) of 4.2 [85], carries a net positive charge at pH 4 due to the lysine residues. GOx is one of the most commonly used redox enzymes in biosensors. GOx is used in biosensors for quantitative determination of glucose in body fluids, food, beverage, and fermentation liquors. GOx is regarded as an ideal model enzyme [86] for use in a biosensor.

Horseradish peroxidase (HRP)

HRP is a conjugated protein consisting of a single polypeptide chain with a molecular weight of 40000 Da. This globular enzyme has molecular dimension of 62 Å × 43 Å × 12 Å with an IEP of 7.0 [87]. The optimum pH for HRP is 7.0. Figure 3.2(b) shows the molecular structure of HRP. The active site of HRP involves the heme group containing iron atom (Fe^{3+}/Fe^{2+}) at the center of a porphyrin ring (see MP-11) as shown Figure 3.2(d). HRP is also one of the key enzymes used in biosensors for the detection of hydrogen peroxide due to catalytic activity for reduction of hydrogen peroxide to water [88].

Microperoxidase-11 (MP-11)

MP-11 is a heme-containing oligopeptide that consists of the active site microenvironment of cytochrome c, an electron transfer protein for many redox enzymes as shown in Figure 3.2(c). The size of MP-11 is approximately 25 Å × 1.3 Å × 15 Å [89]. Heme-containing (iron-porphyrin complexes) proteins have a wide range of biological functions, including simple electron transfer reactions, oxygen transport and storage, oxygen reduction to the level of hydrogen peroxide or water, oxygenations of organic substrates, and the reduction of peroxides [90]. Biomolecule such as MP-11 and HRP catalyzes the reduction of H_2O_2, a strong oxidizing agent, produced in organisms as a byproduct of oxygen metabolism [90] and therefore reduces oxidative stress.

Highly oriented pyrolytic graphite (HOPG) and graphite rod (G)

The ZYH grade HOPG was purchased from GE Advanced Ceramics and was used to support the silicon nanoparticles and enzymes as electrodes. A fresh basal plane of HOPG was obtained by cleaving the basal plane with common adhesive tape. The edge plane of HOPG was prepared by soft scratching the basal plane using a wood rod. The fresh edge plane of HOPG surface was then blown with compressed air to remove debris. Graphite rods (3 mm diameter, Sigma) were polished with slurries of 0.3-μm alumina particles. The polished rods were sequentially sonicated with 1 M NaOH, 0.5 M H_2SO_4, ethanol and deionized water for 10 min, respectively.

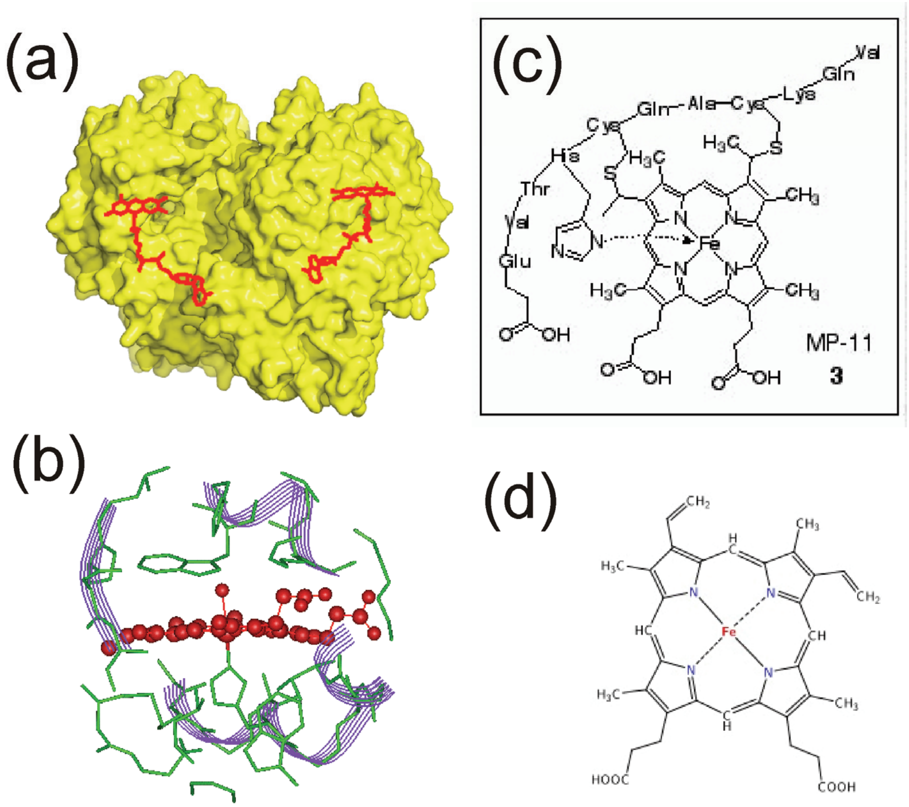

Figure 3.2 Biomolecules (a) Three-dimensional view of GOx. The active center, FAD, is indicated by red structure, which is buried in the protein. (b) Schematic description of HRP [91]. Red-circle-structure in the HRP is heme, the active center. (c) Schematic description of MP-11 containing heme group [57]. (d) Heme [92]. Iron ion at the center of porphyrin ring is oxidized (Fe^{3+}) or reduced (Fe^{2+}).

Silicon wafer

Heavily doped (0.001 ~ 0.005 Ω-cm) n-type silicon wafers with (111) orientation (SQI, California) were used to immobilize silicon nanoparticles. The silicon wafer with its surface containing the native oxide was cleaned with ethanol, isopropanol and deionized water to remove organic and inorganic contaminants. The IEP of Si and SiO_2 are 4 and 2, respectively [93].

Carbon paper and carbon cloth (CP and CC)

Carbon paper (Toray, TGPH) and carbon cloth (A/B, BASF) were purchased from BASF and used as electrodes for its porosity which leads to improved particle-loading. The CC and CP electrodes are rinsed with deionized water before loading particles. Four different thickness of CPs and two different wet proofing percentages of CPs are used for the particle loading.

Enzyme-HOPG electrode

GOx (G6125, Sigma) solution was made by dissolving 10 mg of GOx in 1 mL of 10 mM phosphate buffer solution (PBS) at pH 4. MP-11 (M6756, Sigma) solution was made by dissolving 1 mg of MP-11 in 1 mL of 10 mM PBS at pH 7. HRP (M6756, Sigma) solution was made by dissolving 1 mg of HRP in 1 mL of 10 mM PBS at pH 7. Other chemicals used in this work were of analytical grade. Deionized water (18.2 MΩ-cm, Direct Q3, Millipore) was used to prepare solutions. The enzymes (GOx, MP-11, and HRP) were immobilized on the HOPG. A 0.1 ml drop of the enzyme solution was deposited on the fresh HOPG surface, which was then incubated at room temperature for 4 hours. The electrode was then rinsed with deionized water. Previously, it has been demonstrated that enzymes are able to retain their bioactivities when immobilized on the HOPG electrodes [94-96].

SiNP-Si, SiNP-HOPG, SiNP-G and SiNP-CP electrodes

Silicon nanoparticles (SiNP) used in this work was isopropanol alcohol - based Si1 and Si2.8 (molecular weight = 838.3) colloid with a concentration of 10 μM and was immobilized on various supporting electrodes such as HOPG, silicon wafer and carbon paper. To prepare particle immobilized silicon electrodes (Si1-Si and Si2.8-Si) and HOPG electrodes (Si1-HOPG and Si2.8-HOPG), a 0.1 ml drop of the SiNp colloid was spread on the wafer surface and the HOPG surface, and then the sample was incubated in a container under moisture for 10 hours and then rinsed with deionized water. To prepare particle immobilized graphite electrodes (Si1-G and Si2.8G) and carbon paper electrodes (Si1-CP and Si2.8-CP), three 0.1 ml drops of the SiNP colloid were deposited on a surface of graphite rod and the carbon paper followed by incubation of 10 hours and ringing with deionized water. The surface of electrodes was covered with a mask to form a working area of 1 mm × 1 mm, 2 mm × 5 mm or 3 mm × 3 mm. The SiNP immobilized carbon paper electrodes have a particle surface density of 27.96 $\mu g/cm^2$.

3.2.2 Methods

Electrochemical measurements were performed with a 1-ml conventional three-electrode electrochemical cell controlled by an electrochemical workstation (CH Instrument 660C, Austin, USA). The SiNP-immobilized electrodes and enzyme-immobilized electrodes were used as the working electrode. A commercial Ag/AgCl (saturated KCl) electrode was used as the reference electrode, and a platinum wire was used as the counter electrode. The Ag/AgCl reference potential is converted to the reversible hydrogen electrode (RHE) according to $E_{RHE} = [(E_{Ag/AgCl} + 0.059\text{pH}) + E^{0}_{Ag/AgCl}(0.197)]$ [97].

Cyclic voltammograms (CV) and linear sweep voltammograms (LSV) were obtained at various scan rates, pH values and buffer solutions. The cell potential was scanned from a lower potential in the direction toward higher values for LSV measurement. The buffer solution, if it needed, was deaerated by purging with pure nitrogen gas. The Tafel measurement was used to determine kinetic parameters of an electrochemical reaction. In our work, we use it to estimate the number of electron transferred in the oxidation of glucose, ethanol and methanol. A Tafel plot is obtained by measuring the logarithm of the current or current density of a working electrode while varying the overpotential. In a typical Tafel plot generated using a commercial electrochemical workstation, the vertical axis represents the total potential E applied to the working electrode and the overpotential is the difference between the equilibrium potential, the potential at which no or very little current flows, and the total applied potential E. Tafel measurement was performed at 1 mV/s. Chronoamperometric (I-t) and chronovoltametric (V-t) measurements were performed at constant electrode potential and at constant current, respectively, as function of time. All measurements were made at room temperature.

Control experiments performed with bare (silicon wafer, HOPG , graphite and carbon paper) working electrodes, the reference electrode and the platinum counter electrode showed no electrochemical response to organic fuels, hydrogen peroxides and oxygen from a potential -1 V up to a potential as high as 1.6 V. Note that the results of electrochemical measurements presented in this work have been produced with several electrodes in repeated experimental runs and therefore reflect the typical characteristics of the electrodes used in making the corresponding measurements.

A 3-ml plastic cell was used to contain the anode, the cathode and the solution, forming the single-compartment fuel cell as shown in Figure 3.3(a). The Si1-HOPG electrode and the GOx-HOPG electrode were used as the anodes for the hybrid fuel cell and the biofuel cell, respectively. The HRP-HOPG and the MP-11-HOPG electrodes were used individually as the cathodes for the hybrid fuel cell and the biofuel cell. The anode and the cathode were connected by an external circuit through a set of variable resistors with resistances ranging from 0 Ω to 2 MΩ. The anode is negative terminal and the cathode is positive terminal for the cell voltage measurement. The cell voltage between the electrodes were measured with a multimeter (K2000, Keithley Instruments, USA) interfaced with a personal computer utilizing LabView software. Normally, the cell voltage is measured across a fixed external resistor from 0 Ω to 2 MΩ and then the current is calculated by Ohm's law ($V = IR$). The power is calculated by $P = IV$.

In the construction of the double-compartment prototype fuel cell, an ELAT (carbon paper) electrode containing 0.5 mg/cm^2 Pt particles on Vulcan (E-TEK, XC-72) was used as the cathode, the Si1-CP electrode was used anode, and Nafion membrane (N-115, 125 microns thick, Alfa Aesar) was used as the membrane separating the two glass compartments. The Nafion membrane was pretreated in hot (~ 80 °C) 3% H_2O_2 solution (3% H_2O_2 and 97% water) for 2 hours followed by cooling and rinsing in deionized water [98]. The membrane was then soaked in hot (~ 80 °C) 0.5 M H_2SO_4 for 1 hour to get rid of metallic impurities. The membrane was further rinsed with hot (~ 80 °C) deionized water three times to remove the final traces of acid. The double-compartment cell was constructed by joining two glass cells (each has volume of 30 ml) with the Nafion membrane clamped between the flattened ends of the glass cells as shown in Figure 3.3(b). Enamel coated copper wire (278-1345B, Radio Shack, TX) used to connect external circuit and the electrode. The connected surface between the wire and electrode was sealed using a nonconductive epoxy (Dexter Corp. NJ). The cell voltage was measured across a external resistor by multimeter and converted to current ($I = V/R$) and power ($P = V^2/R$).

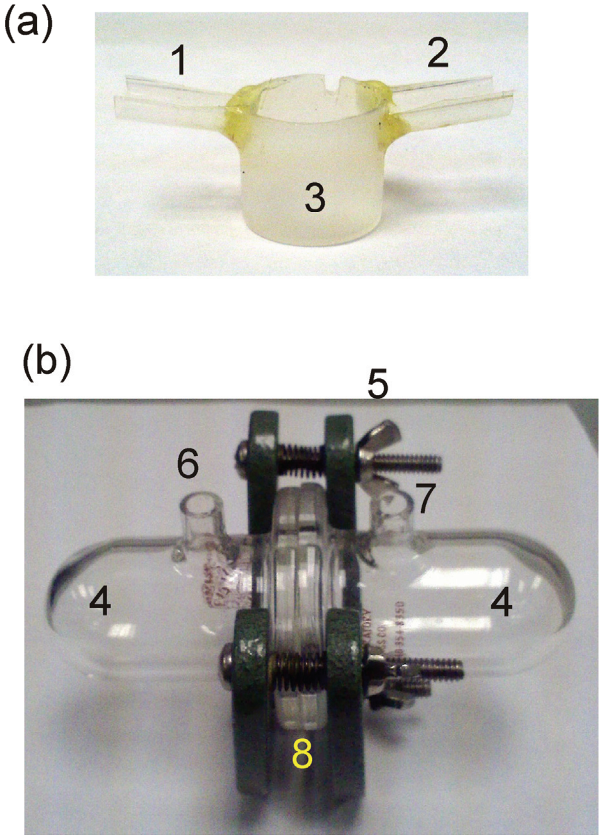

Figure 3.3 Fuel cells (a) The single-compartment fuel cell. 1: an anode electrode holder. 2: a cathode electrode holder. 3: a plastic cell (3 ml) (b) The double-compartment fuel cell. 4: each glass compartment (30 ml). 5: clamp. 6, 7: gas (or electrodes) injection hole. 8: Nafion membrane clamped between the flattened ends of the glass cells to separate them.

3.3 Results and Discussion

3.3.1 Particle-catalyzed electrooxidation of organic fuels

Silicon nanoparticles deposited on silicon electrodes appeared to catalyze the oxidation of ethanol and methanol as shown using cyclic voltammetry (CV). The CVs of a Si1-Si electrode and a Si2.8-Si electrode obtained in ethanol and methanol are shown in Figures 3.4(a) and Figure 3.4(b), respectively. The black CV is the electrodes' background signal obtained in PBS at pH 7. The background signals of the two types of electrodes are identical. The blue CV and the red CV were obtained with the Si1-Si electrode and the Si2.8-Si electrode, respectively, in 20 mM of ethanol and methanol dissolved in the PBS. In Figure 3.4(a), the increase in the blue and red CVs above the background starts at -0.4 V and 0 V vs. Ag/AgCl (0.21 V and 0.61 V vs. RHE), respectively, and the positive scan direction of the potential indicates that ethanol is oxidized by the electrodes. For the oxidation of methanol as shown Figure 3.4(b), the onset potentials for the blue and red CVs are -0.3 V and -0.2 V. Ag/AgCl (0.31 and 0.41 V vs. RHE). As mentioned above, the bare silicon wafer shows no response to ethanol and methanol. Thus, the silicon particles exhibit a catalytic character in the electrooxidation of ethanol and methanol. The calibration curves of these electrodes for ethanol and methanol as shown in Figure 3.4(c) indicate that the Si1 particle, compared to the Si2.8 particle, generates a greater amount of current. Thus, both the onset potential and the strength of the catalysis depend on the particle size. The shape of the electrodes' calibration curves, i.e. a linear region at low fuel concentrations followed a saturation region at higher concentrations, resembles that of enzymes and is indicative of the Michaelis-Menten kinetics, which implies the limited amount of particle (the catalytic unit) on the electrode.

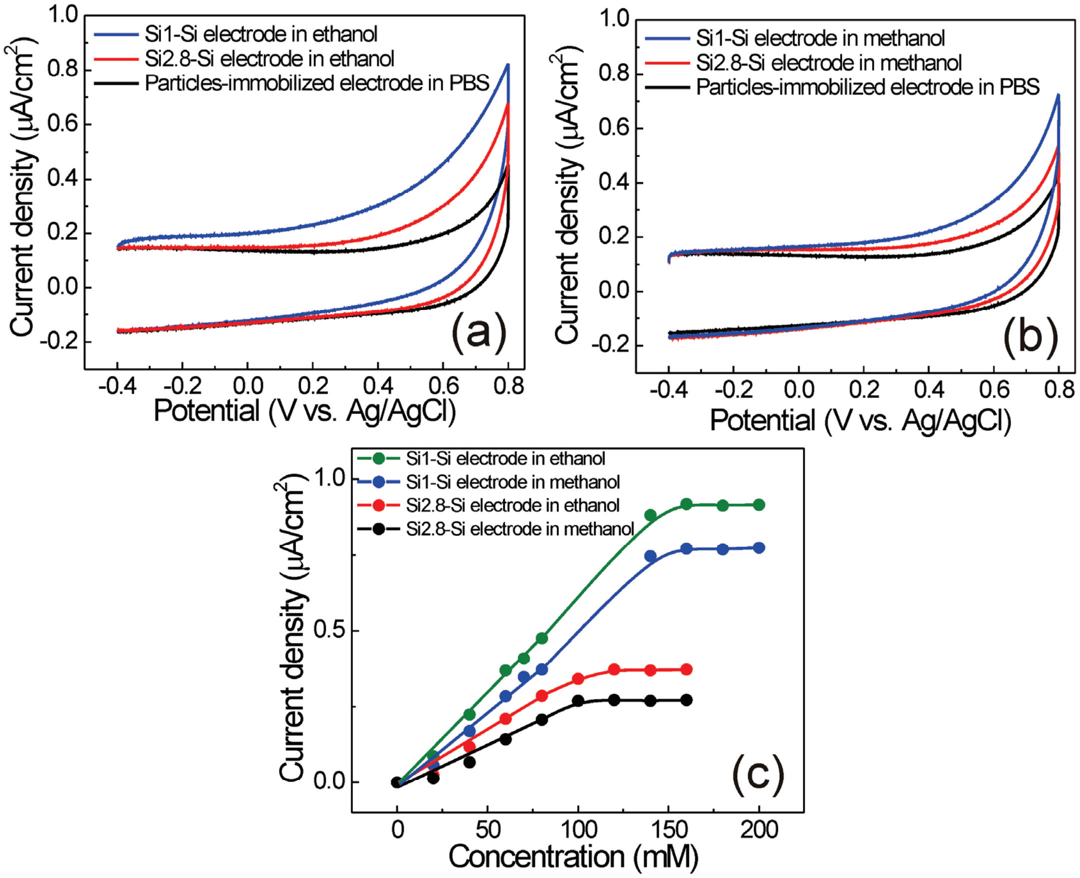

Figure 3.4 Electrochemical characterization of the particle-immobilized silicon electrodes in ethanol and methanol. (a) CVs of a Si1-Si electrode and a Si2.8-Si electrode in PBS (the background) at pH 7 and in the same PBS containing 20 mM ethanol. (b) CVs of a Si1-Si electrode and a Si2.8-Si electrode in PBS containing 20 mM methanol. (c) The ethanol and methanol calibration curves of the same electrodes as in (a) and (b). The ethanol and methanol calibration curves were obtained at potentials of 0.2 V and 0.3 V for the Si1-Si electrode and the Si2.8-Si electrode, respectively. Each data point shows the fuel oxidation current obtained by subtracting the background current from the total anodic current. Similar calibration results were obtained with different electrodes.

The electrochemical responses of particle-immobilized carbon paper electrodes to the fuel molecules also have been studied due to the importance of carbon paper electrodes in fuel cells. The typical linear sweep voltammograms (LSVs) of the Si1-CP and Si2.8-CP electrodes obtained in ethanol are shown in Figure 3.5(a). The electrodes show almost identical background signal (the electrodes' responses in 100 mM PBS at pH 7). The black LSV is representative of the electrodes' background signal. The peak at 0.1 V vs. Ag/AgCl is a characteristic of the carbon paper electrode [9]. The blue LSV and the red LSV were obtained with a Si1-CP electrode and a Si2.8-CP electrode, respectively, in 250 mM of ethanol dissolved in 100 mM PBS. The red LSV (the LSV of the Si2.8-CP electrode) starts increasing above the background at -0.15 V vs. Ag/AgCl. The fact that red LSV increases with a slope while the slope of the black LSV is almost zero within a major portion of the potential range scanned indicates that ethanol is oxidized by the electrode. Therefore, the onset of oxidation occurs at -0.15 V vs. Ag/AgCl (0.46 V vs. RHE) for the Si2.8-CP electrode. The blue LSV (the LSV of the Si1-CP electrode) indicates an onset of oxidation at -0.3 V vs. Ag/AgCl (0.31 V vs. RHE). Figure 3.5(b) shows the typical LSVs of the Si1-CP and Si2.8-CP electrodes obtained in methanol. Thus, both the onset potential and the strength of the catalysis depend on the particle size. As mentioned above, bare CP shows no response to ethanol and methanol within the potential range scanned. The calibration curves of the Si1-CP electrode for ethanol and methanol are shown in Figure 3.5(c). The shapes of the calibration curves are characterized by a linear region at low fuel concentrations followed a saturation region at higher concentrations, implying the limited amount of particle (the catalytic unit) on the electrode. The calibration curves of the Si2.8-CP electrode for the two fuels show similar features. Note that the properties shown in Figure 3.5 have been observed with several Si1-CP and Si2.8-CP electrodes.

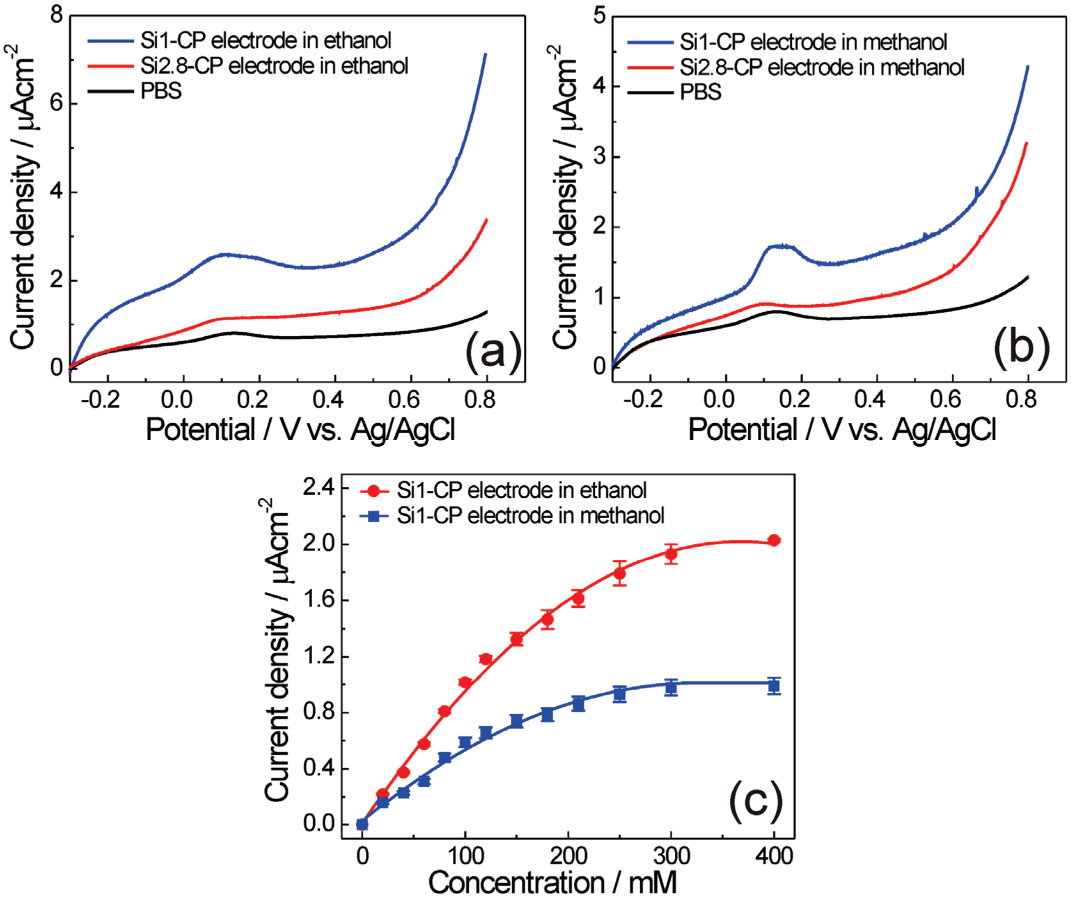

Figure 3.5 Electrochemical characterization of the particle-immobilized carbon paper electrodes in ethanol and methanol. (a) LSVs of the Si1-CP electrode and the Si2.8-CP electrode in 100 mM PBS (the background) at pH 7 and in the same PBS containing 250 mM ethanol. (b) LSVs of the Si1-CP electrode and the Si2.8-CP electrode in 100 mM PBS (the background) at pH 7 and in the same PBS containing 250 mM methanol. (c) The calibration curves of the Si1-CP electrode for ethanol and methanol at pH 7. The curve was obtained with 4 electrodes made under identical conditions. The calibration curves were obtained at potentials of 0.1 V. Each data point shows the fuel oxidation current obtained by subtracting the background current from the total anodic current.

The particle-immobilized graphite electrodes exhibit complex catalytic characteristics as displayed in Figures 3.6(a) and 3.6(b). In the Figure 3.6(a), the CV of the bare graphite electrode in PBS at pH 7 (the black CV) is featureless in the potential range scanned. Under the same condition, the CV of the Si2.8-G electrode (the red CV) shows a pair of redox peaks at 0 V and 0.1 V, indicating that the particle behaves as a redox species on the graphite surface. The redox peaks could be caused by the particle's interaction with the graphite surface, the nature of the interaction being unclear at the present. As ethanol is introduced to the PBS, the current of the oxidation peak at 0.1 V increases and the peak potential shifts slightly to the positive direction. At higher ethanol concentrations, the oxidation peak current increases further and two new oxidation peaks appear at 0.55 V and 0.8 V as shown by the green and the purple CVs in Figure 3.6(a). All of the oxidation peak currents increase with further increase in ethanol concentration. Therefore, new catalysis pathways at higher potentials are triggered. The same phenomenon has been observed with methanol as shown in Figure 3.6(b). Figure 3.6(c) shows the ethanol and methanol calibration curves of the Si2.8-G electrode obtained at the 0.1 V. The curves are also indicative of the Michaelis-Menten kinetics. Note that the same properties have not been observed with the Si1-G electrode.

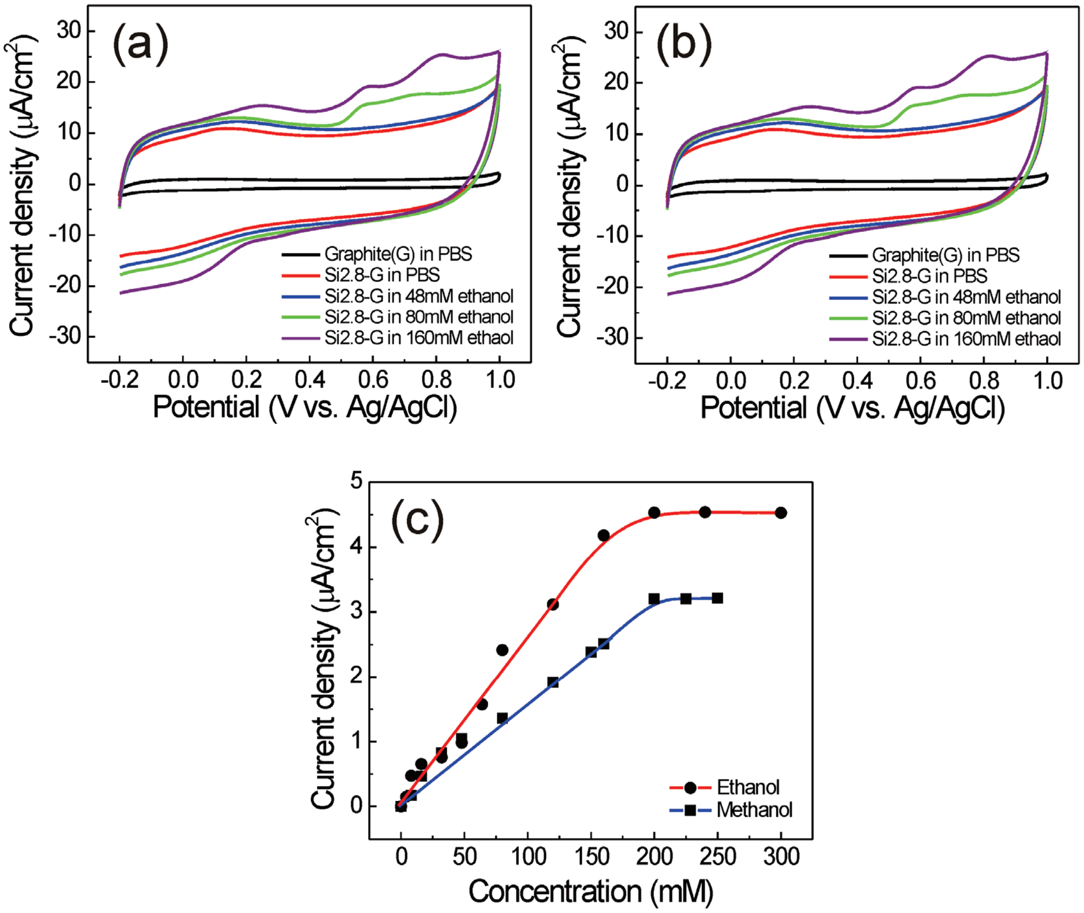

Figure 3.6 Electrochemical characterization of the Si2.8-G electrode. (a) The CV of a bare graphite electrode obtained in PBS is displayed with those of the Si2.8-G electrode obtained in PBS and ethanol. All curves were obtained at pH 7. Two new oxidation peaks appear at high ethanol concentrations. (b) The CV of a bare graphite electrode obtained in PBS and the Si2.8-G electrode obtained in PBS and methanol. All curves were obtained at pH 7. (c) Calibration curves of the Si2.8-G electrode for ethanol and methanol at pH 7. The curves were obtained at the potential of 0.1 V, where the first oxidation peak is located.

To characterize the kinetic properties of the electrooxidation process induced by the particles, we obtained Tafel plots of the particle-immobilized silicon electrodes in the fuels. Figures 3.7(a) and 3.7(b) show the Tafel plot of the Si2.8-Si electrode obtained in ethanol and methanol, respectively. Figures 3.7(a) and 3.7(b) are obtained in 60 mM of ethanol and 60 mM of methanol dissolved in a 10 mM PBS at pH 7, respectively. The Tafel slopes of the plot are listed in Table 3.1. The Tafel slopes shown in Table 3.1 yield, for their corresponding electrocatalytic reactions, the values of the product, αn ($= 2.3RT / F\cdot slope$), where α, n, R, T and F are the electron transfer coefficient, the number of electrons transferred in the reaction, gas constant, temperature and the Faraday constant [35]. The slop of 212 mV/decade for ethanol gives the αn value of 0.28 and the slop of 178 mV/decade for methanol gives the αn value of 0.33. The αn values for ethanol and methanol suggest a most probable value of $n = 1$ because the α value lies between 0.3 and 0.7 in most systems. The insets of Figures 3.8(a) and 3.8(b) show the log plot of the electrode's oxidation current density as a function of substance concentration at a constant electrode potential (0.8 V) to determine the reaction order (= slope). The values of reaction order as shown in Table 3.1 also suggest the electrooxidation of ethanol and methanol is the first order reaction. Thus, the electrooxidation of ethanol and methanol as catalyzed by the Si2.8-Si electrode is a first order reaction which involves the transfer of one electron.

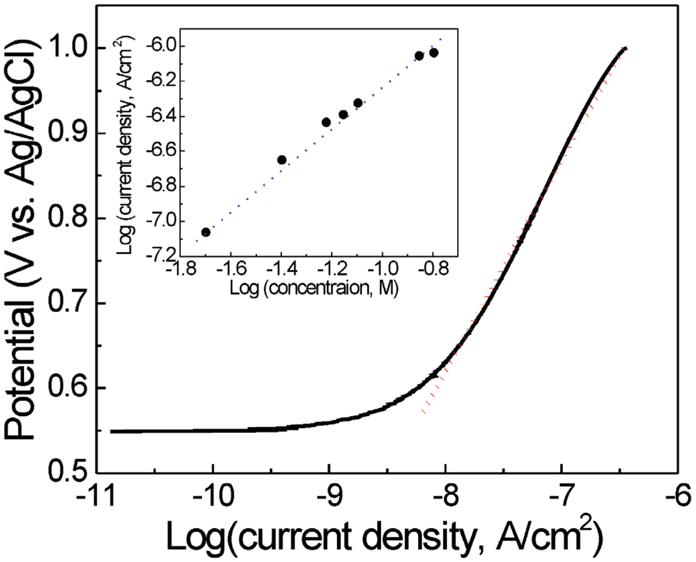

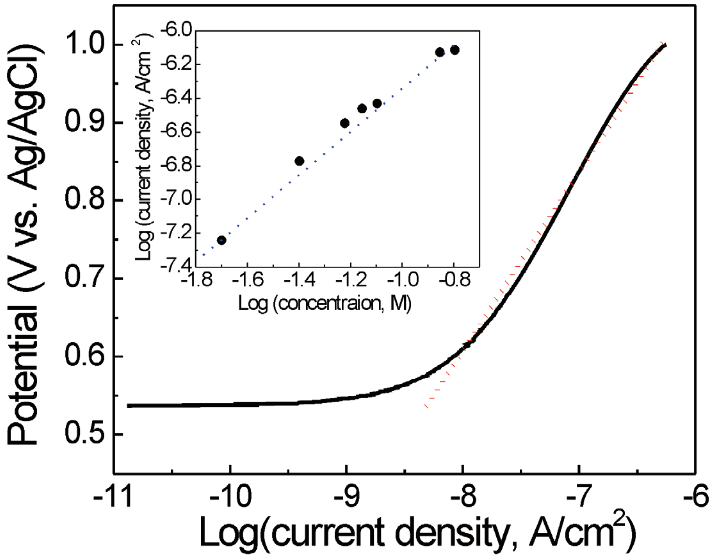

Figure 3.7 Kinetic properties of particle immobilized silicon electrode to alcohol. (a) The Tafel plot of the Si2.8-Si electrode in 60 mM of ethanol dissolved in a 10 mM PBS at pH 7. The dotted line is used to determine the slope of the plot. The inset is the log-log plot of the electrode's catalytic current density vs. ethanol concentration obtained at 0.8 V of the Tafel plot. (b) The Tafel plot of the Si2.8-Si electrode in 60 mM of methanol dissolved in a 10 mM PBS at pH 7. Other conditions are same as (a).

Table 3.1 Kinetic parameters of the electrocatalytic processes of the three fuels using the particle-immobilized silicon electrode, where α is the electron transfer coefficient and n is the number of electrons transferred per molecule.

	Tafel slope (mV/decade)	αn	n	Reaction order
Ethanol	212	0.28	1	1.03
Methanol	178	0.33	1	1.29
Glucose	180	0.33	1	1.07

Electrooxidation of ethanol and methanol on the Pt electrode is known to proceed by initial adsorption of fuel fragments on the electrode [8,9]. The peak observed in the anodic current of the CV is caused by initial electrode poisoning due to adsorption of CO in the low potential range and subsequent oxidation of the Pt electrode at a higher potential [10]. The oxidation of the two fuels on the Pt electrode starts at a high potential of 0.6 V vs. RHE [9-11] in acidic electrolytes. The Pt/Ru system provides a bi-functional mechanism, in which the fuel fragments adsorb on Pt and Ru provides oxygen-containing adsorbates such as OH, which gives rise to oxidative removal of CO at nearby Pt sites at a lower potential (~ 0.4 V vs. RHE), therefore lowering the onset of oxidation [13-15]. It was found that the activities of Pt and Pt/Ru for ethanol and methanol oxidation at room temperature is stronger under alkaline condition than under acid condition [10,11]. As shown above, the oxidation of the fuels catalyzed by the particle-immobilized electrodes produces a smooth increase in the anodic current with an onset potential in the CV of the electrodes. The monotonous increase suggests a direct catalysis pathway [15]: the fuel molecules are oxidized due to the presence of the particle so that electrons are transferred directly from the molecules to the electrode. In the present work *n* = 1 from Tafel analysis while *n* = 6 for the Pt and Pt/Ru systems where *n* is the number of electrons transferred in the reaction. The small value of *n* may imply the absence of long-term adsorption and adsorption-induced electrode poisoning of the particle-immobilized electrodes.

In addition to catalytic activities to ethanol and methanol, the silicon nanoparticles were also able to catalyze the oxidation of glucose. We have performed CVs of the particle-immobilized silicon electrodes to study the electrocatalytic properties of the particle for glucose oxidation. The CVs that indicate the particle-catalyzed electrooxidation of glucose at pH 7 are shown in Figure 3.8(a). The CV (black dashed) obtained with a bare silicon electrode in PBS without glucose coincides with that (blue dash-dotted) obtained with the same electrode in the presence of glucose. The green dotted CV is the background signal of the Si1-Si electrode obtained in PBS. When glucose was added to the PBS resulting in 2 mM solution, the response of the electrode is indicated by the red solid CV, which shows an increase in the anodic current above the background. This increase indicates the direct oxidation of glucose by the electrode. Note that the bare silicon wafer shows no response to glucose within the range of potential used in the experiment. Thus, the solid CV indicates the electrooxidation of glucose catalyzed by Si1. Shown in Figure 3.8(b) is the glucose calibration curve of the electrode obtained at pH 7. Several characteristics of the catalytic process should be noted. The oxidation, as shown by the solid CV of Figure 3.8(a), occurs at potentials as low as -0.40 V versus Ag/AgCl (0.21 V vs. RHE). The glucose calibration curve of the electrode is linear in the low concentration range, followed by a saturation region for higher glucose concentrations. This shape resembles those of enzymes and is indicative of the Michaelis-Menten kinetics. Note that we have not observed the electrooxidation of glucose with the Si2.8-Si electrode. Figure 3.8(c) shows the Tafel plot of a Si1-Si electrode obtained in 2 mM glucose solution at pH 7. The Tafel slope of the plot is listed in Table 3.1. Figure 3.8(c) shows that, with the slope being 180 mV/decade, the value of αn is 0.33, suggesting a most probable value of $n = 1$ for the electrocatalysis. The slope of the plot yields the order of the electrocatalytic reaction, which is 1.07. Thus, the electrooxidation of glucose as catalyzed by Si1 is a first order reaction which involves the transfer of 1 electron. Possible products of the oxidation of glucose observed here include different kinds of carboxylic acids as previously observed on platinum electrodes [99]. Future work includes identifying the products.

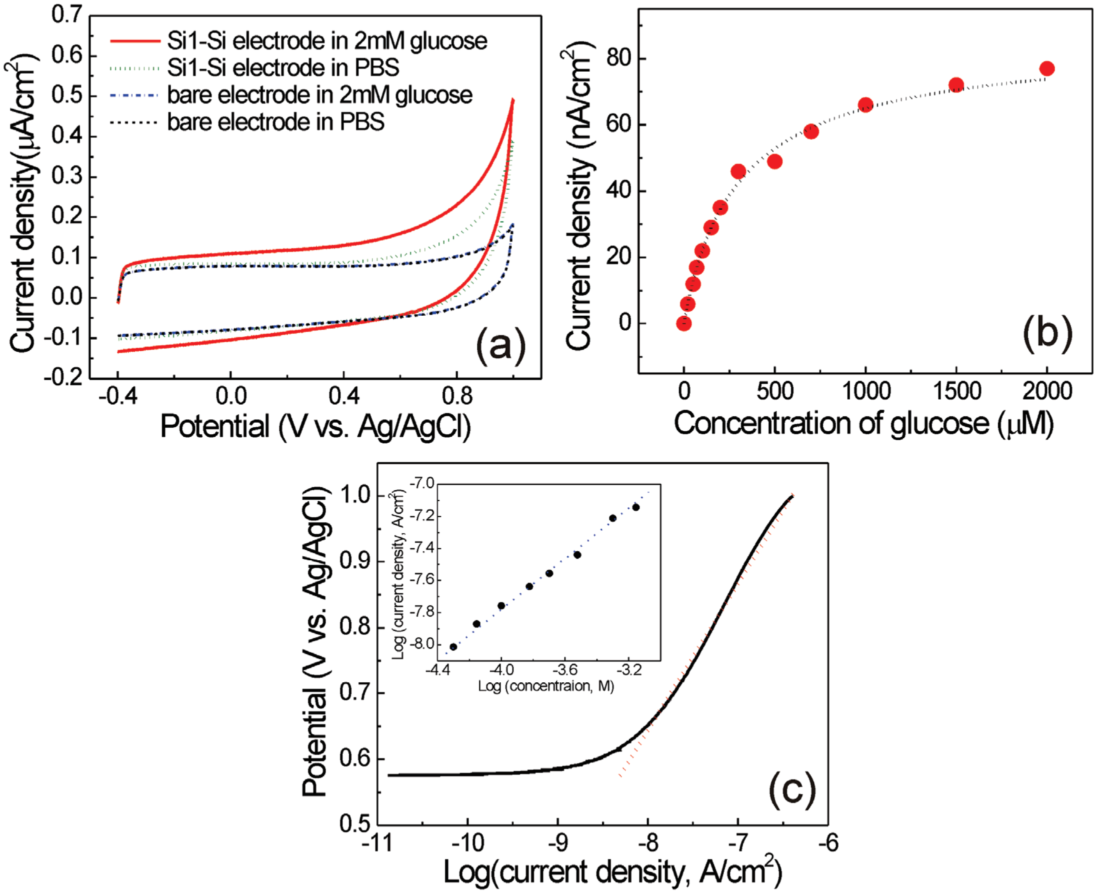

Figure 3.8 Electrooxidation of glucose using the Si1-Si electrode. (a) The dashed CV was obtained with a bare silicon electrode in PBS without glucose while the dash-dotted CV was obtained with the same electrode in the presence of 2 mM glucose. The dotted CV, the background signal, was obtained with the electrode in a 50 mM PBS at pH 7. The solid CV is the electrode's response to adding 2 mM glucose to the PBS. (b) The electrode's glucose calibration curve obtained at 0.8 V at pH 7. Each data point shows the oxidation current obtained by subtracting the background current from the total anodic current. (c) The Tafel plot of the Si1-Si electrode in 2 mM of glucose dissolved in a 50 mM PBS at pH 7. The dotted line is used to determine the slope of the plot. The inset is the log-log plot of the electrode's catalytic current density vs. glucose concentration obtained at 0.8 V of the Tafel plot.

We have studied the particle-catalyzed oxidation of ethanol and methanol under acidic and alkaline conditions. Figures 3.9(a) and 3.9(b) obtained with the Si1-CP electrode show the LSVs of the silicon nanoparticles in ethanol and methanol under acidic, neutral and alkaline conditions, respectively. The LSVs show a significantly larger activity of the silicon particle under alkaline condition than under acidic condition for both ethanol and methanol. At low potentials the catalytic activity shows a 50-fold with ethanol and a 250-fold with methanol increase under alkaline condition compared to under acidic condition. Therefore, the pH dependence of the catalytic activity of the silicon nanoparticles is qualitatively the same as those of Pt and Pt/Ru. In the Pt and Pt/Ru case, the pH dependence is attributed to the pH competitive adsorption of oxygenated species with anions from supporting electrolytes [11], while, in the present study, the cause is not clear yet. The observation presented here reflects a general property of the particle-immobilized carbon paper electrode.

In summary, we show that the particles exhibit electrocatalytic activities to the three fuels and that the onset potential and electrooxidation strength depend on the particle size. The onset potentials of the particle-catalyzed electrooxidation to ethanol and methanol are ~ 0.2 V lower than those of the Pt-catalyzed electrooxidation, suggesting the absence of initial electrode poisoning due to adsorption of fuel fragments. The monotonous increase of the oxidation current suggests the absence of the oxidation of the catalyst, which occurs in the Pt case. However, the number of electrons transferred during the particle-catalyzed electrocatalytic reaction is one while the Pt-catalyzed electrocatalytic reaction is six. In addition, the lower onset potential gives rise to large potential difference between the anode and the cathode in the fuel cell applications.

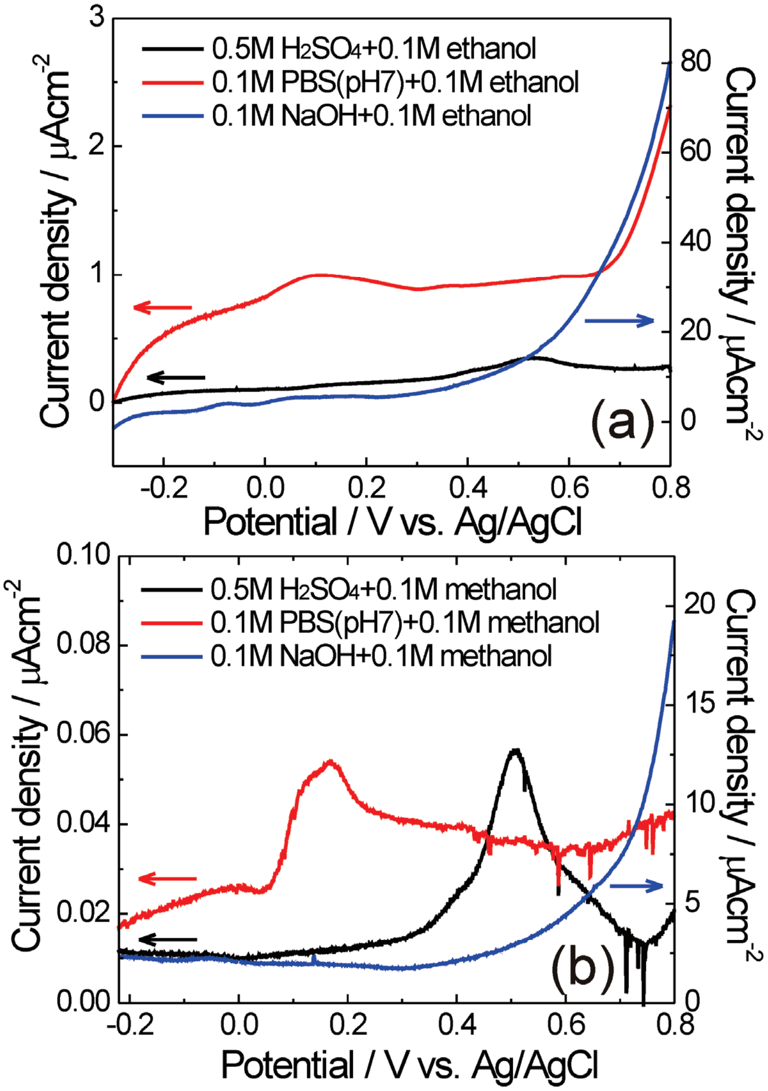

Figure 3.9 The pH-dependence of the particle-catalyzed electro-oxidation. (a) The LSVs were obtained with a Si1-CP electrode with ethanol. Each LSV shows the fuel oxidation current obtained by subtracting the background current from the total anodic current. (b) The LSVs were obtained with a Si1-CP electrode with methanol. Each LSV shows the fuel oxidation current obtained by subtracting the background current from the total anodic current.

3.3.2 Chronoamperometric study of catalysis

In order to gain insight into the nature of the electrodes' response to the fuel molecules, experiments were designed and performed to distinguish the oxidation current from the electrodes' charging current as shown in Figures 3.10(a) and 3.10(b). In general, when the electrode potential is scanned at a given rate, the charging current due to the double-layer capacitance is independent of the electrode potential within the potential range used here [38]. This implies that, in Figure 3.10(a), the observed fast increase in the anodic current (see the red CV) when ethanol is introduced into the cell is due to the oxidation of ethanol. Note that, in electrooxidation of ethanol and methanol, the presence of current peaks in CVs is not the only indication of the oxidation process. In many cases, the oxidation of the fuel molecules causes a continuous increase in the anodic current without producing peaks as the molecules are introduced to the electrode [100,101]. In fact, the peak appearing in the anodic current associated with the oxidation of methanol and ethanol using pure Pt electrodes is caused by the oxidation of the Pt electrode (see below), being indirectly caused by the catalytic process.

In Figure 3.10(a), the black CV was obtained at a low PBS concentration of 1 mM, and the CV shows a near-rectangle shape, which is indicative of the charging current. When 200 mM ethanol is added to the solution, the anodic current for the low potential range (from -0.4 V to about 0.05 V) shows a near-constant increase of ~ 0.07 $\mu A/cm^2$ above the black CV. This increase should be due to the additional charging of the electrode caused by ethanol. The fast increase in the anodic current beyond this potential range is caused by the oxidation of ethanol. Therefore, 0.05 V vs. Ag/AgCl is the onset potential for the oxidation of ethanol using the Si2.8-Si electrode. The presence of the oxidation current is also demonstrated using chronoamperometric (I-t) measurement. Figure 3.10(b) shows the temporal responses of the Si2.8-Si electrode in PBS and in ethanol. The current of the electrode is monitored as a function of time separately in 1 mM PBS (black dot) and in 200 mM ethanol dissolved in 1 mM PBS (red dot) at a potential of 0.7 V vs. Ag/AgCl. In PBS, the time response as traced using the black dots decreases exponentially, following the charging current equation ($i_c \propto \exp(-t)$) [37]. The solid curve (the blue curve) in inset of Figure 3.10(b) is the exponential fitting curve. The time response to ethanol is traced by the red dots. In general, the faradaic current due to the electrode's reaction to an analyte follows the Cottrell equation ($i_f \propto t^{-0.5}$) for linear diffusion case [37]. The red solid curve is the fitting curve to the time trace, showing that the current decreases according to $t^{-0.32}$. Thus, we attribute the observed non-exponential dependence of the electrode current on time to the presence of the electrooxidation current of ethanol. The difference in the exponents of t between the observed value of 0.32 and the theoretical value of 0.5 is due to several effects such as nature of electrode, electrode reaction rate, convection and migration [37].

In summary, we have performed chronoamperometric experiments in order to distinguish the oxidation current produced by the fuel molecules from the charging current of the catalytic electrode. The chronoaperometry results clearly show the two components of the total electrode current, confirming the presence of the fuel oxidation reaction.

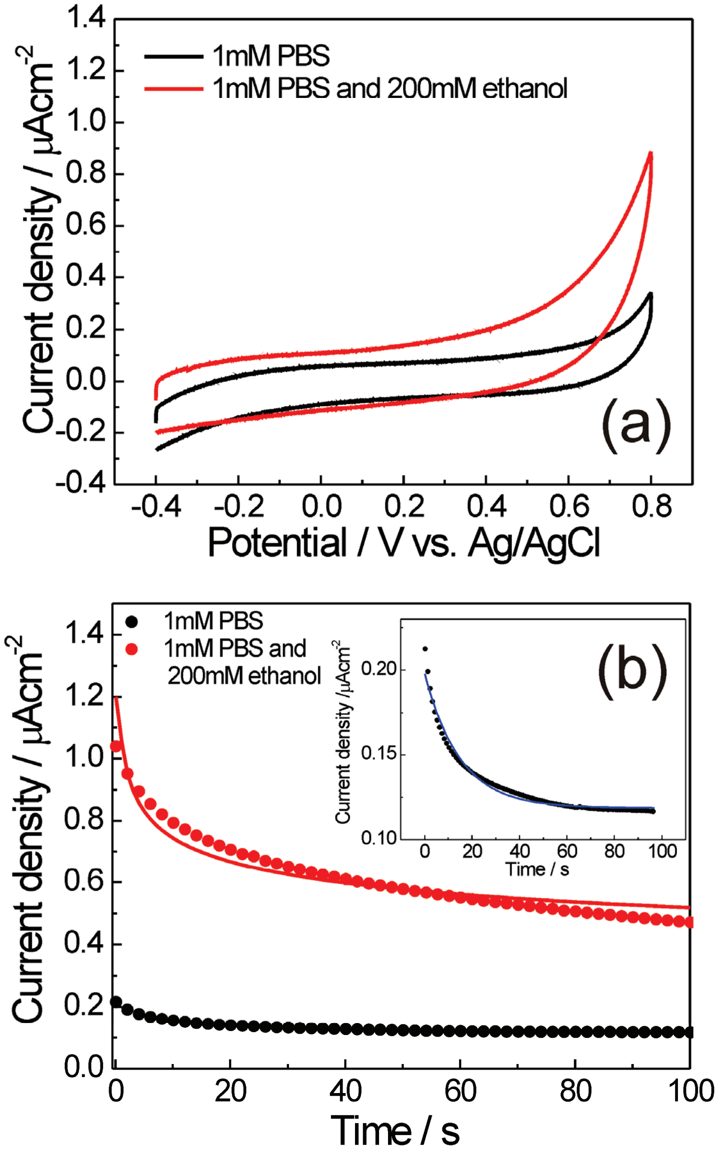

Figure 3.10 Electrochemical characterization of the Si2.8-Si electrode in ethanol. (a) CVs of a Si2.8-Si electrode in 1mM PBS (the black CV), and 200 mM ethanol (the red CV) dissolved in 1 mM PBS at pH 7. (b) Chronoamperograms of the Si2.8-Si electrode in 1 mM PBS (black dots) and in 200 mM ethanol dissolved in 1 mM PBS (red dots) obtained at a potential of 0.7 V and pH 7. The solid curves are the corresponding fitted curves. The inset is a detailed chronoamperogram obtained in PBS.

3.3.3 Light dependence of particle-immobilized electrode

In this study of electrocatalysis, an unexpected light-dependent phenomenon was observed. In the electrocatalysis of the fuels using the silicon particles, the catalytic current shows substantial and persistent increase when the catalytic process is performed in darkness as compared to performing the same experiment in light. This phenomenon was studied with the room light of the laboratory or a 13-watt fluorescent lamp. Figure 3.11(a) shows the CVs obtained in an ethanol experiment with a Si1-Si electrode in room light and darkness at pH 7. The catalytic current shows on the average a two-fold increase due to darkness as compared to the current measured in room light (white fluorescent light with intensity 0.5 mW/cm^2). The inset of Figure 3.11(a) shows this effect in a time trace. Turning off the light caused an increase of 35 nA/cm^2 in the electrooxidation current density above that observed in the light. Figure 3.11(b) shows this light-dependent effect observed with a Si1-CP electrode in ethanol at pH 13. In the low potential range, the catalytic current is doubled due to darkness. Subsequent exposure to light brings the current close to the original level. Figure 3.12(a) shows the light-induced (using the lamp) "switching" effect in the catalytic current observed in the time domain with a Si1-CP electrode in ethanol at pH 7. The time trace shows two steady states of the current due to the change in the state of illumination together with two characteristic transient quantities. The rise time (T_r) is the transient time for the current to reach the high current state from the low state after light is turned off. The time it takes the current to decrease from the high state to the low state after light is turned on is the fall time (T_f). The time trace shows that T_r is noticeably greater than T_f. This dynamic characteristic of the light-induced switching in the electrocatalytic current was also observed under alkaline condition as shown in Figure 3.12(b).

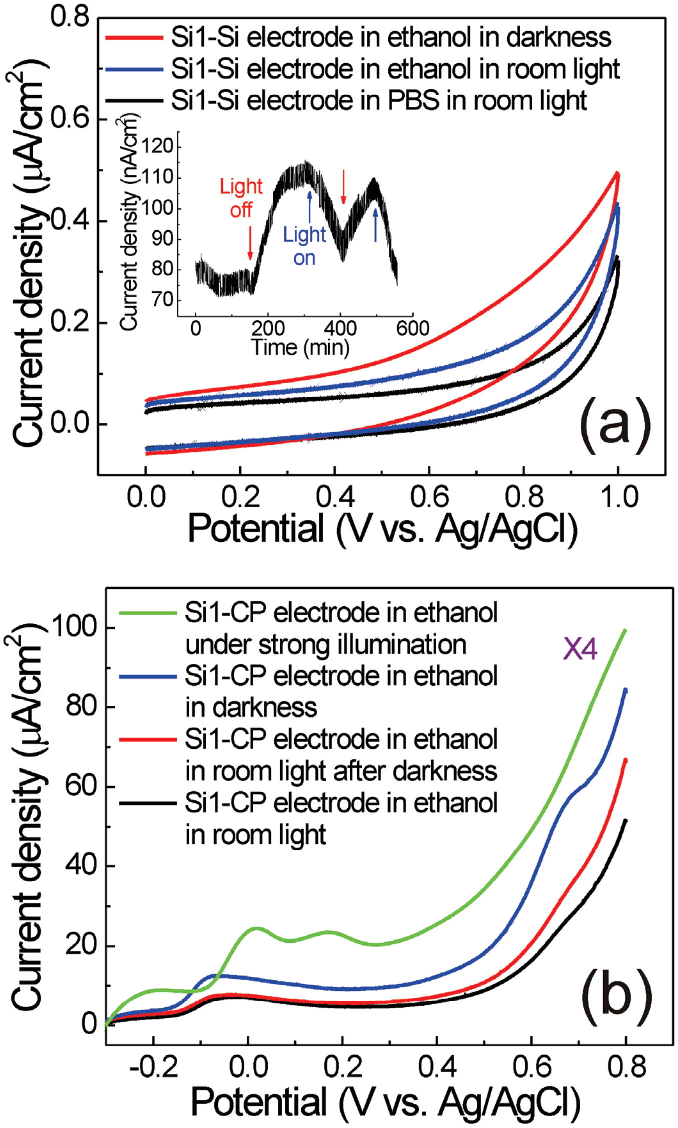

Figure 3.11 The effect of white light illumination and darkness on ethanol oxidation current. (a) The current density produced by a Si1-Si electrode in 200 mM ethanol at pH 7 shows an increase in darkness as compared to that produced in room light (0.5 mW/cm^2). The inset is a current-time trace, showing the effect of turning-off and turning-on the light. The trace was obtained using a different electrode at 0.3 V and 200 mM of ethanol. (b) The catalytic current produced by a Si1-CP electrode in 200 mM ethanol at pH 13 in room light, in darkness and under strong illumination of 200 mW/cm^2 at pH 13.

In order to appreciate this unusual light-dependent phenomenon described above from another perspective, we have performed the electrocatalysis under much stronger illumination. Figure 3.12(c) is the time trace of a Si1-CP electrode in methanol at pH 7 under the illumination of a 40 ~ 200-watt light source (200 mW/cm^2). The electrode's response to the illumination appears as a significant increase in the catalytic current. The magnitude of the current pulses should be compared to that of Figure 3.12(b). Figure 3.12(c) shows that the strong illumination has caused a 14-fold increase in the current as compared to the room-light case. This behavior of increasing catalytic current caused by light illumination is conceptually expected since the heat generated in the system by light can be used as energy to overcome the activation barrier to enhance the rate of catalysis. However, low-intensity light may excite excitons across the 3-eV band gap of the Si1 particle with a long recombination lifetime, a characteristic feature of the ultrasmall silicon nanoparticles [102]. The formation of excitons tends to block the conduction of electrons from the ionized molecules and hence diminishes the oxidation current. The mechanism of the light-dependent oxidation current is subjected to future studies.

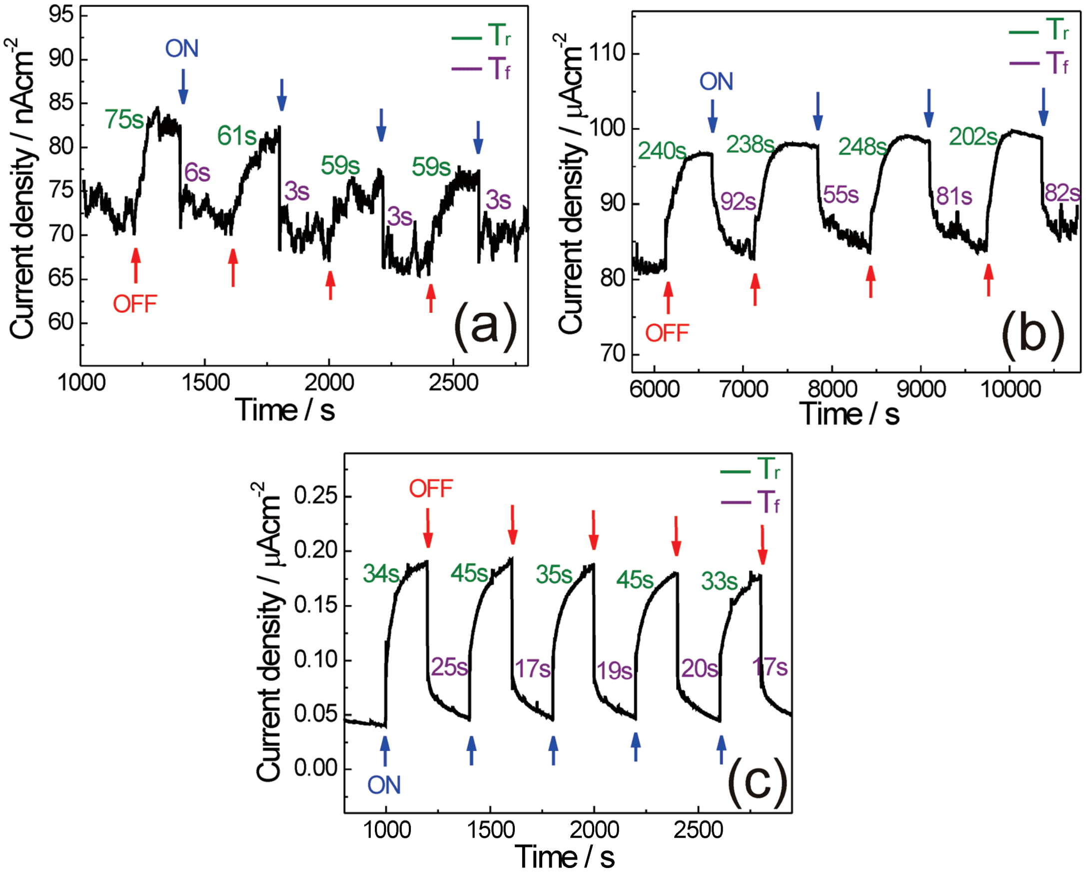

Figure 3.12 Time-resolved responses of the catalytic current to the state of illumination. (a) The time trace of a Si1-CP electrode in 200 mM of ethanol at pH 7 shows the switching of the catalytic current due to the ON/OFF of white light of 0.5 W/cm^2. Trace was obtained at 0.7 V. (b) The time trace of the electrode in (a) at pH 13 with other conditions unchanged. (c) The time trace of the electrode in (a) in strong illumination of 200 W/cm^2 with all other conditions unchanged.

3.3.4 Prototype fuel cells

To demonstrate the potential of the silicon nanoparticles in fuel cell applications, we have constructed three kinds of prototype fuel cells using the silicon nanoparticles as the anode electrocatalyst. The first prototype fuel cell was a hybrid fuel cell, whose anode was a Si1-HOPG electrode and the cathode was a HRP-HOPG electrode as shown Figure 3.13(a). The anode and cathode were immersed in a PBS contained in a plastic cell and electrically connected through a load resistance R_L. This prototype single-compartment fuel cell operated on glucose and H_2O_2, which were dissolved in the PBS. Glucose was oxidized by Si1 and H_2O_2 was reduced by HRP. It is known that HRP in the presence of an electron donor (in our case, the cathode) catalyzes the reduction of H_2O_2 to water [103]. Figure 3.13(b) shows the electrode potential vs. substrate concentration curves of the hybrid cell. The saturation of the curves at high concentrations indicates the Nernstian behavior. The saturated potential values reflect an open-circuit voltage of 0.33 V. The curves can be used to optimize the cell performance. The CVs in Figure 3.13(c) show the bio-electroreduction of H_2O_2 brought about using a HRP-HOPG electrode. The CVs indicate that the onset of the reduction occurs at -0.15 V vs. Ag/AgCl. Note that the particle-catalyzed oxidation of glucose occurs at or below -0.4 V vs. Ag/AgCl as shown in Figure 3.8. Thus, the reduction reaction occurs at a higher potential than the oxidation reaction and the electrode potentials satisfy the requirement for the operating condition of fuel cells.

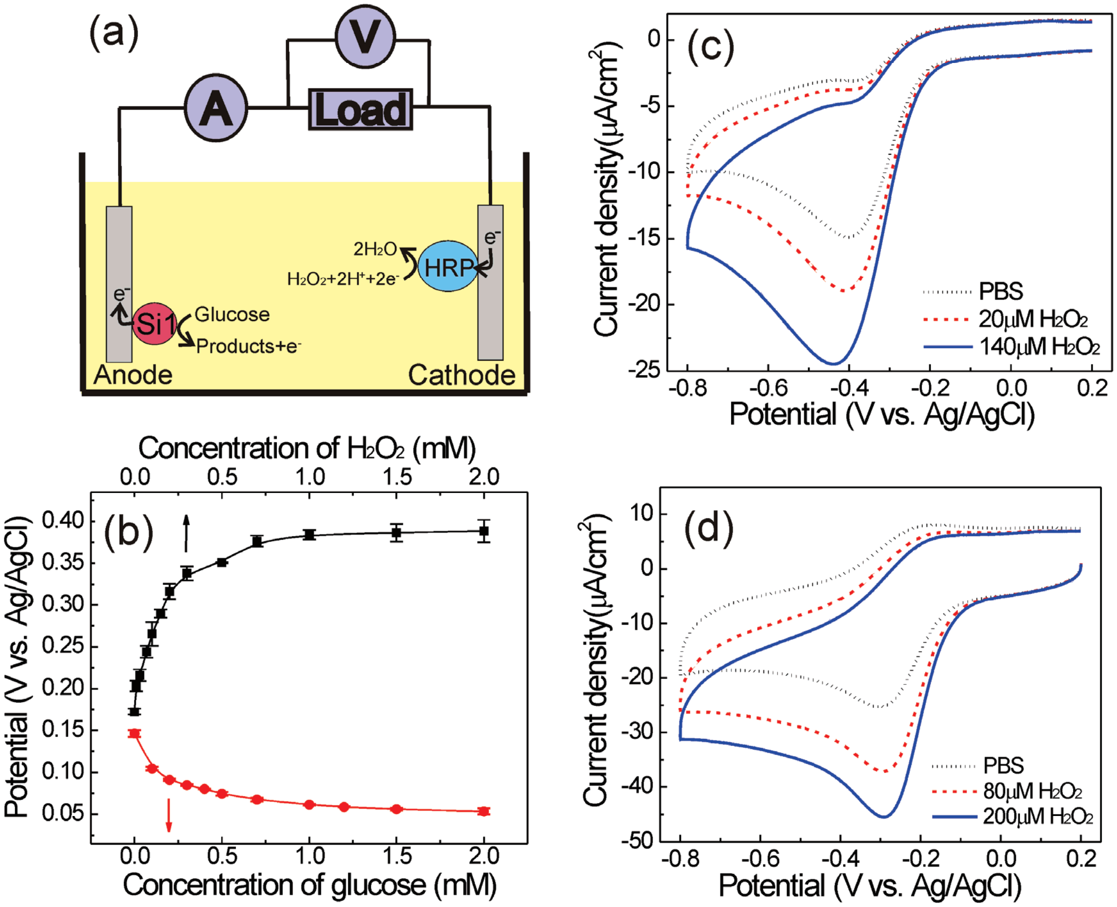

Figure 3.13 Characteristic of the prototype single-compartment hybrid biofuel cell. (a) A schematic description of the hybrid biofuel cell. Glucose and H_2O_2 are used as the fuel and oxidizer, respectively. (b) The plots of electrode potentials as a function of the fuel and the oxidizer concentrations. The lower plot shows the potential of a Si1-HOPG electrode vs. an Ag/AgCl reference electrode as a function of glucose. The upper plot shows the potential of a HRP-HOPG electrode vs. an Ag/AgCl reference electrode as a function of H_2O_2. (c) CVs were obtained with a HRP-immobilized HOPG electrode in PBS and in two different H_2O_2 concentrations. (d) The CVs were obtained with a MP-11-immobilized HOPG electrode in PBS and in two different H_2O_2 concentrations. MP-11 produced more reduction current and a more positive reduction onset potential.

The hybrid fuel cell was tested with a PBS containing 2 mM glucose and 2 mM H_2O_2 at pH 7 and room temperature. Figure 3.14(a) shows the cell current vs. cell voltage (I-V) and the power density vs. cell current (P-I) characteristics of the cell. The open-circuit voltage (OCV) is 0.16 V. The peak power density is 1.3 $\mu W/cm^2$. Figure 3.14(b) indicate that the I-V characteristics of the hybrid fuel cell deviate from the ideal rectangular behavior [104]. The deviation shows the typical three-region characteristics: the activation polarization in the low current region, the ohmic polarization region and the concentration polarization region in higher current regions [105]. The deviation reduces cell voltage below its reversible thermodynamic value [106].

To improve the output power of the hybrid cell, we replaced HRP by the heme-containing polypeptide microperoxidase-11 (MP-11) to reduce H_2O_2 at the cathode. Compared to HRP, MP-11 has a more compact structure, which allows effective direct electrical communication with electrodes. The CVs in Figure 3.13(d) show the largely increased reduction current of H_2O_2 using MP-11-HOPG than that of the HRP-HOPG electrode. The MP-11-electrocatalyzed reduction of H_2O_2 also shows a more positive onset of -0.05 V vs. Ag/AgCl. Figure 3.14(b) shows the I-V characteristics of the fuel cell obtained at 2 mM glucose and several concentrations of H_2O_2 and Figure 3.14(c) shows the corresponding P-I characteristics. The characteristics corresponding to the condition of 2 mM glucose and 2 mM H_2O_2 are to be compared to those obtained with HRP as shown in Figure 3.13(a). Note that the remaining three characteristics in Figures 3.14(b) and 3.14(c) were obtained under the physiological concentrations of glucose and H_2O_2 [107]. Figures 3.14(b) and 3.14(c) show that the output power increases with increasing concentration of H_2O_2 with a glucose concentration of 2 mM. This behavior qualitatively agrees with the result shown in Figure 3.13(b). Figure 3.14(b) indicates that the region of activation polarization is absent in the I-V characteristics. We attribute this absence to the enhanced direct electrical communication at the cathode caused by the use of MP-11. The improvement in cell performance is reflected in OCV of 0.28 V, which is close to the predicted value of 0.33 V, and the peak power density of 3.7 $\mu W/cm^2$.

We have also constructed a biofuel cell by replacing the anode of the hybrid fuel cell with a GOx-immobilized HOPG and using MP-11 as the cathode catalyst. Note that the enzymes are in direct contact to the bare electrode [96]. The I-V and P-I characteristics of the biofuel cell obtained at 2 mM glucose and 2 mM H_2O_2 are shown in Figure 3.14(d). The I-V characteristics show the three characteristic regions due to deviation from the Nernstian behavior. The peak power density of the biofuel cell is about 5 times less than that obtained with the hybrid fuel cell. Previously, the kinetic properties of the electrooxidation of glucose catalyzed by the particle-immobilized electrode have been compared to those catalyzed by the GOx-immobilized electrode [78]. It was found that the silicon particle is more efficient than GOx in performing the oxidation of glucose with enhanced kinetic rate constants. We attribute the improved performance of the hybrid fuel cell as compared to that of the biofuel cell observed in this work to the enhanced kinetic properties of the particle-catalyzed glucose oxidation. Note that the current and power levels of the biofuel cell at the physiological concentrations (2 mM glucose and less than 1 mM H_2O_2) are extremely low.

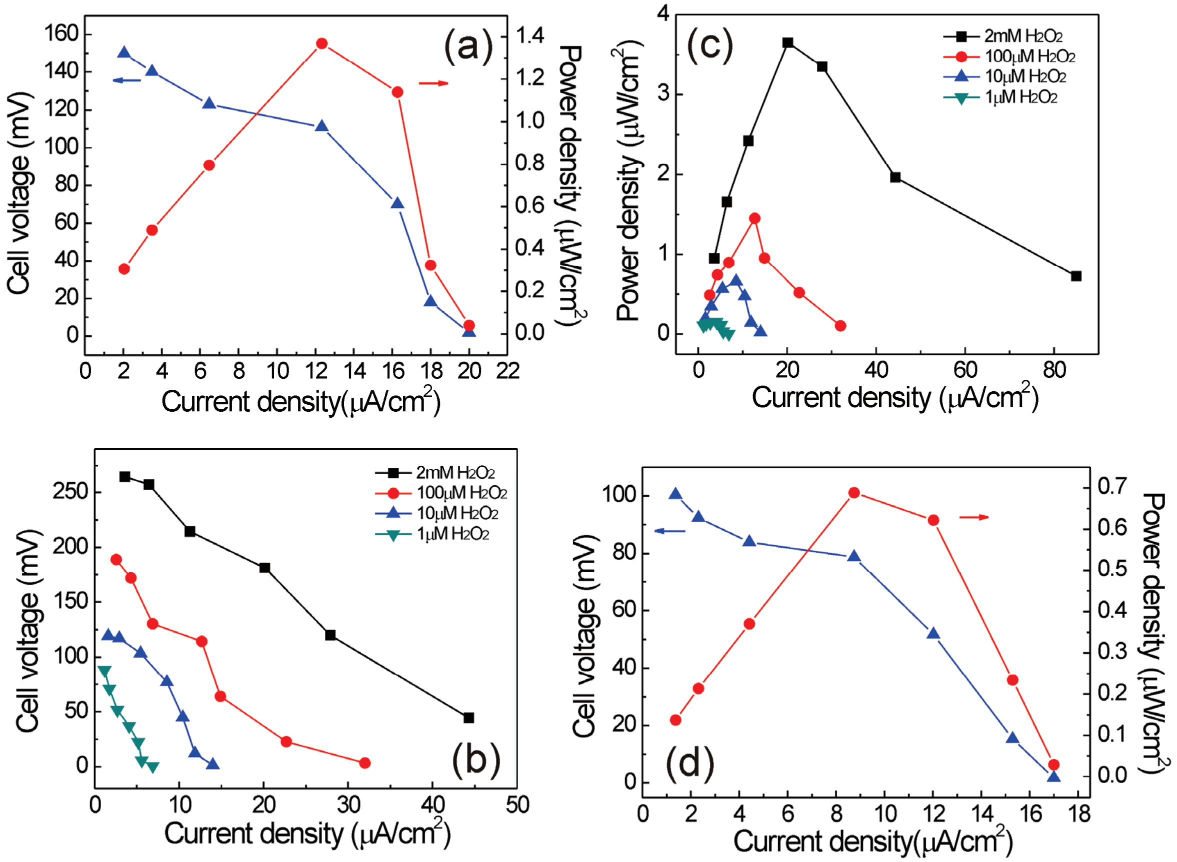

Figure 3.14 Characteristics of hybrid biofuel cells and a biofuel cell. (a) The I-V and P-I characteristics of the hybrid cell with a HRP-HOPG cathode operating on 2 mM glucose and 2 mM H_2O_2. (b) and (c), respectively, show the I-V and P-I characteristics of the hybrid cell with a MP-11-HOPG cathode operating on 2 mM glucose and different H_2O_2 concentrations. (d) The I-V and P-I characteristics of a biofuel cell with a GOx-HOPG anode and a MP-11-HOPG cathode operating on 2 mM glucose and 2 mM H_2O_2.

The long-term stability of the hybrid fuel cell has been characterized by monitoring the cell voltage for R_L = 1 MΩ. Monitoring the cell voltage using a large load resistance [108] eliminates the effect of the depletion of fuel and oxidizer. Figure 3.15 shows the changes in the cell voltage during a period of five days at the fuel concentrations giving maximum power (2 mM glucose and 2 mM H_2O_2) and at the physiological concentrations (2 mM glucose and 10 μM H_2O_2). The plot for 2 mM glucose and 2 mM H_2O_2 shows a fast decrease in the cell voltage (82 % of the initial value) during the first day. The plot corresponding to the physiological concentrations shows a slow decrease in the cell voltage from its initial value at an average rate of 13% per day. Figure 3.15 is the time plot of the cell voltage of the biofuel cell operating on 2 mM glucose and 2 mM H_2O_2. The cell voltage dropped to an extremely small value within 8 hours. Since the depletion of fuel and oxidizer can be ruled out, the decrease in the cell voltage of the biofuel cell is likely to be caused by the degradation of the enzymes due to the fact that the enzymes are subjected to a non-native environment, i.e. the solution and the electrode. In particular, the presence of H_2O_2 may produce detrimental effects on the enzymes since it is known that H_2O_2 damages cells and tissues. This possibility is supported by the results shown in Figure 3.15 that, for the hybrid fuel cell, the voltage in the high H_2O_2 concentration case decrease much faster than in the low H_2O_2 concentration case. This could be due to the detrimental effect of H_2O_2 on MP-11. However, the even faster decrease in the biofuel cell case indicates that H_2O_2 could also make a detrimental effect on GOx, the anode catalyst. Therefore, the improved electrode stability of the hybrid cell compared to biofuel cell could be attributed to the integrity of the silicon particles.

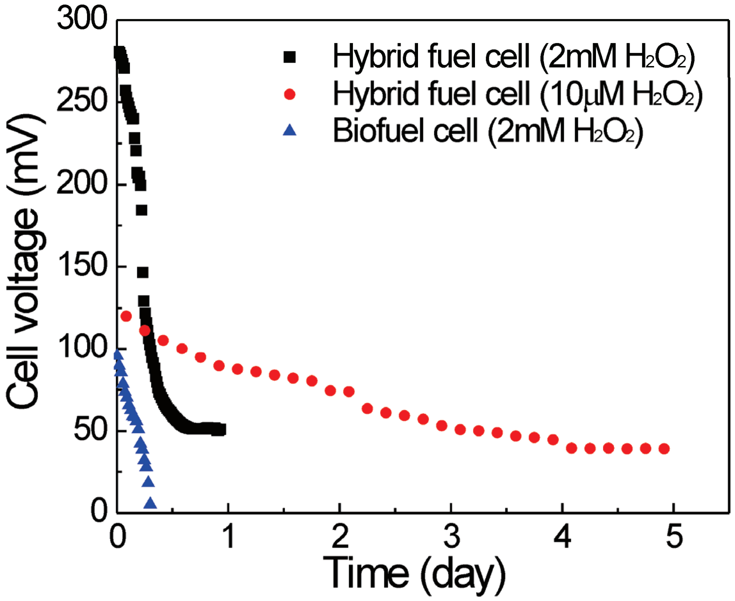

Figure 3.15 The stability of the hybrid fuel cell and the biofuel cell as demonstrated by monitoring the cell voltage in time. Both cells contained 2 mM glucose. The hybrid cell contained physiological concentration of H_2O_2 (10 μM).

Figure 3.16 shows another prototype hybrid biofuel cell. The Si1 particles on an HOPG electrode were used as the anode catalyst for the electrooxidation of glucose to produce electrons, which generate a current in the external circuit. Two enzymes, MP-11 and GOx, were co-immobilized on a HOPG electrode as the cathode catalyst. The anode and cathode electrodes were in a 3 ml plastic cell which contained 20 mM glucose dissolved in PBS. GOx catalyzed the oxidation of glucose to produce H_2O_2, which diffused to MP-11 to be reduced to water as shown Figure 3.16. The advantage of this cell is that both anode and cathode use same fuel (or oxidant). Figure 3.16 shows cell current versus voltage (I-V) and the power density versus cell voltage (P-V) characteristics of the fuel cell. The cell's OCV is 0.2 V and the peak power density is 1.3 μW/cm^2. The I-V characteristic shows a deviation from the ideal rectangular shape. This deviation could be a result of mass transport losses, reducing the cell voltage below its reversible thermodynamic value. The power output of the fuel cell can be improved by employing a more efficient cathode reaction such as the reduction of oxygen to water using bilirubin oxidase [106].

Comparing the output power of the hybrid fuel cell operating on glucose only to that of the hybrid fuel cell operating on glucose and 1 μM H_2O_2, the performance of the former fuel cell is enhanced by co-immobilization of two enzymes. These prototype hybrid fuel cells are constructed in the single-compartment cell using physiologically ambient glucose and H_2O_2 as fuels so that the hybrid fuel cells can be used as an implantable power source for biomedical applications such as power supply for biosensors [109], cardiac pacemakers [73] artificial hearing [104] and vision devices [75]. A typical power level of ~ 1 μW is required for the operation of the cardiac pacemaker [76]. In addition, the hybrid fuel cells show high output power density and long-term stability because the particles, compared to the enzyme GOx, show fast substrate conversion kinetic characteristics and the particle-immobilized electrodes exhibit stable long-term current output.

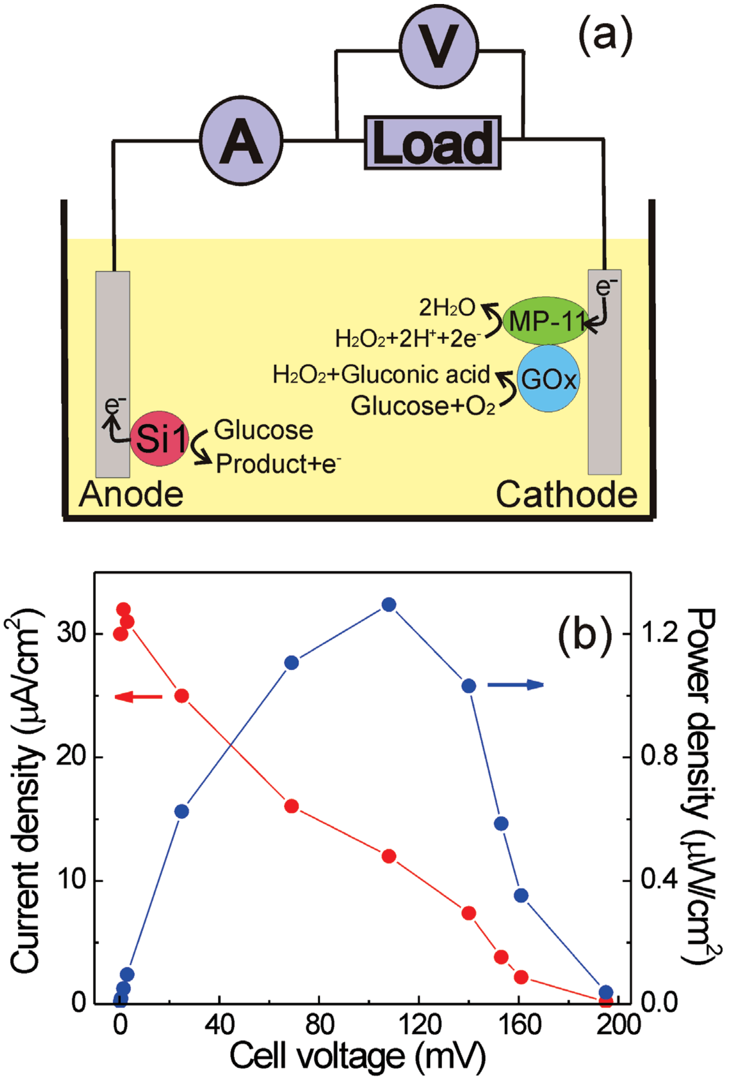

Figure 3.16 The second prototype single-compartment hybrid biofuel cell. (a) A schematic description of the hybrid biofuel cell. The Si1-HOPG electrode is used for anode and the GOx and MP-11 co-immobilized on HOPG electrode is used for cathode. (b) The I-V and P-V characteristics of the hybrid biofuel cell as described in (a) obtained in 20 mM glucose dissolved in PBS at room-temperature.

As shown Figure 3.5, the particle-immobilized carbon paper electrodes show an onset of oxidation for the fuels between -0.3 V and -0.15 V vs. Ag/AgCl, which is equivalent to 0.31 V and 0.46 V vs. RHE. The oxygen reduction reaction on Pt electrodes occurs at about 0.6 V vs. RHE [104,110]. Therefore, in principle, the particles can be used as the anode catalyst in direct alcohol fuel cells. To demonstrate the feasibility of the silicon particles in the double-compartment fuel cell, we have constructed a prototype direct ethanol fuel cell as describe schematically in Figure 3.17(a), using the Si1 as the anode catalyst in PBS containing 200 mM ethanol at pH 6. Pt particles were used as the cathode catalyst for the reduction of oxygen dissolved in 100 mM PBS at pH 6. The open-circuit voltage of the cell is 0.48 V. Figure 3.17(b) shows the cell density vs. current voltage (I-V) and the power density vs. cell voltage density (P-V) characteristics of the fuel cell. As shown in the literature [111,112], the I-V characteristics of the fuel cells show a deviation from the ideal rectangular shape. This deviation could be a result of mass transport losses, reducing the cell voltage below its reversible thermodynamic value. The maximum power density for the double-compartment cell is about 35 $\mu W/cm^2$. It is expected that the power output of the double-compartment fuel cell can be increased by employing a membrane-electrode assembly, which has been treated using hot press. The output power of the prototype fuel cell is expected to improve with optimized operating conditions such as the pH values of the compartments, buffer concentration and particle loading.

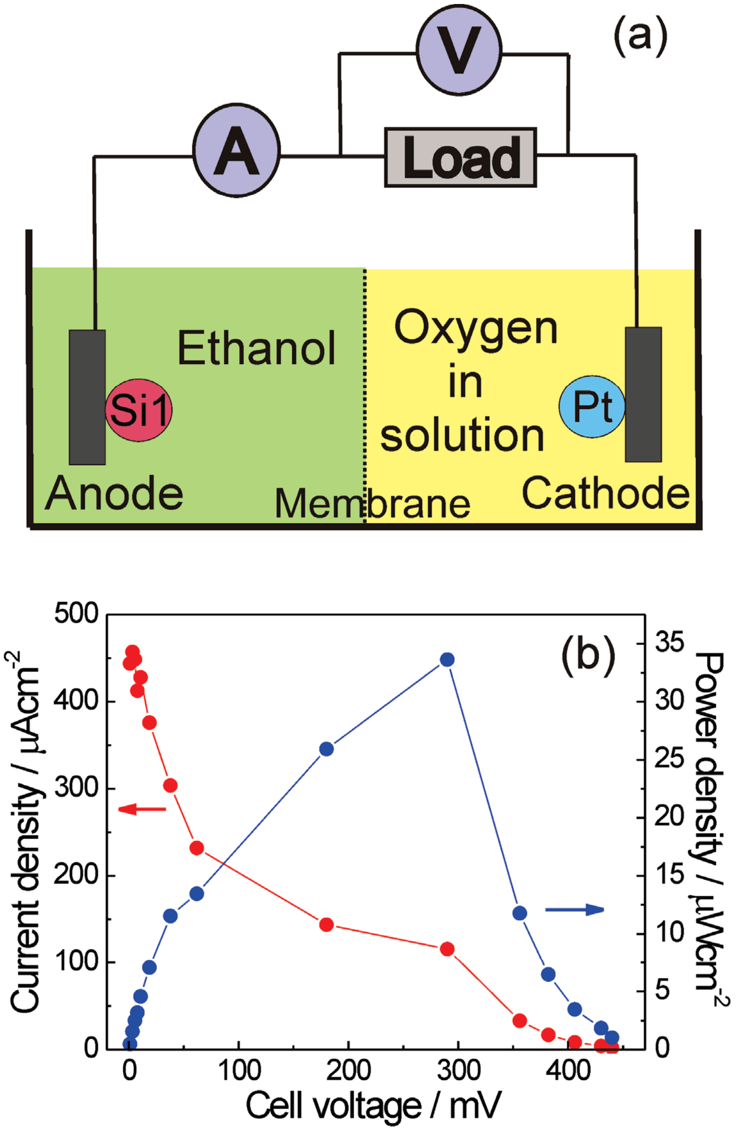

Figure 3.17 The prototype double-compartment fuel cell (a) A schematic description of the double-compartment ethanol fuel cell. A Si1-CP electrode and a Pt-containing ELAT electrode were used as the anode and the cathode, respectively. Each glass compartment had a volume of 30 ml. The cathode solution was saturated with oxygen. (b) The I-V and P-V characteristics of the fuel cell as described in (a) obtained at room-temperature.

Chapter 4 Ultrasensitive biodetection - the enzymatic transistor

4.1 Introduction

Bio-detection or bio-sensing is based on the chemical interaction between a biological molecule (a redox enzyme in the present work) and a substance of interest (the analyte or the substrate of the enzyme). The enzyme is used as the sensing element and the chemical reaction between the enzyme and the analyte produces the electrical current, which is used for the qualitative or quantitative determination of the analyte. Because of the specific interaction between the enzyme and its substrate, bio-sensing provides substance selectivity. Ultra-sensitive bio-detection techniques for the detection of extremely low analyte concentration have been intensively studied for many areas such as biomedical and environmental applications [55]. In particular, ultra-sensitive, highly-selective and fast-responsive bio-detection methods are required for early detection of important analytes such as disease related substances [7], carbon dioxide and oxygen in human body, blood, air, water, soils and other environmental situations [113]. Bio-electrochemical sensing appears as a suitable approach for these areas. However, the inherent low level of interfacial charge transfer of this detection approach due to the embedment of enzymes' active sites by the insulating protein environment creates a fundamental limit to the detection limit of this approach.

Several techniques have been proposed to overcome the inefficient electron transfer between the active site of the enzyme and the electrode. By attaching ferrocene, an electron relay, to glucose oxidase (GOx), direct transfer of electrons from the active site through the relays to the electrode resulted in a glucose detection limit of 5 μM [26]. However, the catalytic effect of the enzyme is decreased due to the introduced foreign materials and modification of protein. Also, mediators can be introduced to shuttle electrons between the enzyme active site and the electrode. The enzyme, GOx, was attached to self assembled monolayers of alkanethiols on gold electrode and the mediator molecule (p-benzoquinone) diffused from solution to the GOx, transporting electrons from the active sites of GOx to the electrode [114]. This sensor has a linear glucose response range of 0 ~ 50 mM with a detection limit of 1 mM [114]. However, the selection of mediators for the desired system is limited due to the fact that redox potential of mediator should be closed to that of the enzyme. Also, metal nanoparticles were used as a immobilized mediator to connect the active site of GOx and an electrode to enhance electron transfer [29]. For example, GOx adsorbed on a CdS nanoparticle modified electrode showed a linear glucose detection range of 0 ~ 33.3 mM with a detection limit of 50 μM [30]. An ethanol sensor assembled with alcohol dehydrogenase (ADH) and gold nanoparticles on tin oxide electrode was developed and the sensor detected as low as 3.3 μM of ethanol [115]. An immobilization method to attach the enzyme on the electrode utilizing conductive polymer (polypyrrole and ployaniline) or hydrogels (polyacrylamide) has been studied. The linear range of glucose detection from 0.01 mM to 1 mM with 5 μM detection limit was obtained in a glassy carbon electrode on which GOx was co-immobilized with a layer of poly p-pherrylenediamine [27]. However, these techniques rely on foreign materials whose selection is limited by the redox potential of enzyme and by other important factors such as stability, toxicity and biocompatibility.

In addition to using foreign materials to enhance electron transfer and detection limit, the ion-selective field-effect transistor (ISFET) [116] has been used as a sensing device for improved detection, using redox enzymes as sensing elements. The principle of ISFET is described in section 4.3.1. A ISFET-based glucose biosensor, in which GOx is immobilized on the membrane covering the gate, showed a linear detection range of 0.25 ~ 2 mM and a detection limit of 150 μM [117]. A silicon nano-channel ISFET biosensor has been developed for glucose detection. The glucose biosensor response was linear in the 0 ~ 8 mM range with a detection limit of 0.5 mM [118]. Also, an ISFET biosensor using ADH as the sensing element for the detection of ethanol and nicotinamide adenine dinucleotide (NAD^+), a cofactor of ADH, allowed a detection limit of 0.4 μM NAD^+ and 20 mM ethanol, respectively [119]. Hydrogen peroxide (H_2O_2) sensors based on ISFET using inorganic and organic materials were developed. The sensors utilizing iridium oxide, prussian blue and Os-polyvinylpyridine containing HRP as hydrogen peroxide sensing materials showed a H_2O_2 detection limit of 100 μM, 10 μM and 0.1 μM, respectively [120].

This chapter describes an ultrasensitive detection method using the basic biosensing scheme modified with gating electrodes for applying a voltage to the redox enzymes immobilized on the working electrode. This technique does not require the use of foreign materials to modify the enzyme. By applying an external voltage between the gating electrode and the working electrode on which GOx was immobilized, the biocatalytic output current of the detector was increased significantly, demonstrating a voltage-controlled amplification of the output current of the detector. The voltage-controlled amplification allowed the detection limit of glucose to be lowered from the milli-molar level to the zepto-molar level. The current amplification could be reversibly controlled by the applied voltage. Applying this technique to the ethanol-ADH system showed similar results. The enzyme's bio-specificity was preserved in the presence of the field. In fact, the detector turns out a field-effect transistor, whose current generating mechanism is the conversion of the analyte to the product. Additionally, field-controlled reaction kinetics of biological catalysis is achieved using MP-11 and H_2O_2 system. The manipulated electron transfer by the applied voltage causes kinetic parameters of the catalysis to acquire nonlinear dependences on the applied voltage, implying an efficiently controlled substance conversion process.

4.2 Experimental

4.2.1 Materials

Alcohol dehydrogenase (ADH)

ADH oxidizes alcohol (ethanol) to aldehydes or ketones [58]. This reaction requires a conenzyme nicotinamide adenine dinucleotide (NAD^+) as a hydrogen acceptor and has a broad specificity for alcohol substrates. ADH falls into a group of dehydrogenases that have a nucleotide binding domain. ADH is a homo-dimer and each monomer has 374 residues with molecular weight of 74000 Da. The active site of ADH has two binding domains, the coenzyme binding site, where NAD^+ binds, and the substrate binding site, where the alcohol binds [121]. Most of the binding site for NAD^+ is hydrophobic. Figure 4.1(a) shows a schematic diagram of ADH.

Coenzymes (FAD and NAD^+)

Flavin adenine dinucleotide (FAD) is a coenzyme which functions as oxidation-reduction catalysts in the biological systems [122]. FAD is usually tightly bound to proteins and cycle between the reduced and the oxidized state while remaining attached to the same protein molecule. Depending upon the nature of the flavoprotein, the redox potential of FAD will vary [123]. Once in the reduced state, $FADH_2$ can be re-oxidized back to FAD by molecular oxygen [124]. The Figure 4.1(b) shows a chemical structure of FAD/$FADH_2$ and its redox reaction [58]. The redox reaction of FAD is [$FAD + 2e^- + 2H^+ \rightleftharpoons FADH_2$].

Nicotinamide adenine dinucleotide (NAD^+) is a coenzyme involving redox reactions in metabolism. The main function of NAD^+ is the transfer of electrons from one redox reaction to another [119]. NAD^+, an oxidizing agent, is reduced in the form of NADH by accepting an electron and hydrogen from other molecules and then NADH, a reducing agent, can be re-oxidized to NAD^+ by donating an electron and hydrogen [125]. Figure 4.1(c) shows a chemical structure of NAD^+/NADH and its redox reaction. The redox reaction of NAD^+ is [$NAD^+ + 2e^- + H^+ \rightleftharpoons NADH$].

Iron-protoporphyrin IX (FePP)

FePP, known as a heme, is a prosthetic group consisted of an iron ion (Fe^{2+}/Fe^{3+}) in the middle of a porphyrin ring as shown in Figure 4.1(d) [90]. The iron can be reduced or oxidized during the electron transfer reaction. FePP has an electrocatalytic property for reducing oxygen [126]. Metallo-proteins containing the heme exhibit wide range of biological functions such as an electron transfer reaction, oxygen transport and storage, oxygenations of organic substrates and the reduction of oxygen and hydrogen peroxide [58].

ADH-HOPG, MP-11-HOPG and FePP-HOPG electrodes

ADH (A3263, Sigma) solution was made by dissolving 5 mg of ADH in 1 mL of 100 mM phosphate buffer solution (PBS) at pH 7.8. 10 mM NAD^+ (N7004, Sigma) solution was prepared in deionized water. ADH molecules were immobilized on the edge plane of HOPG. A 0.1 ml drop of the ADH solution was deposited on the HOPG surface, which was then incubated at room temperature for 10 hours. The electrode was rinsed with deionized water. The attachment of NAD^+ to ADH was carried out by contacting the ADH-immobilized electrode with 10 mM NAD^+ solution followed by rinse with de-ionized water. MP-11 (M6756, Sigma) solution was made by dissolving 1 mg of MP-11 in 1 mL of 100 mM PBS at pH 7. 10 mM sodium borate buffer solution (SBS) at pH 10 was used to prepare 100 μM FePP (H9039, Sigma) solution. A 0.1 ml drop of MP-11 solution for a MP-11-immobilzied electrode and FePP solution for a FePP-immobilized electrode was deposited on the edge plane of HOPG surface, which was then incubated at room temperature for 10 hours. All the solutions were prepared using deionized water (18.2 MΩ-cm, Direct Q3, Millipore). Other chemicals used in this work (*β*-D(+)glucose with 97% purity, ethanol with > 99.9% purity, sodium phosphate with > 99.95% purity and sodium borate > 99% purity) were purchased from Sigma-Aldrich and were used as received. Hydrogen peroxide (H_2O_2, H352) were purchased from Fisher and used as received.

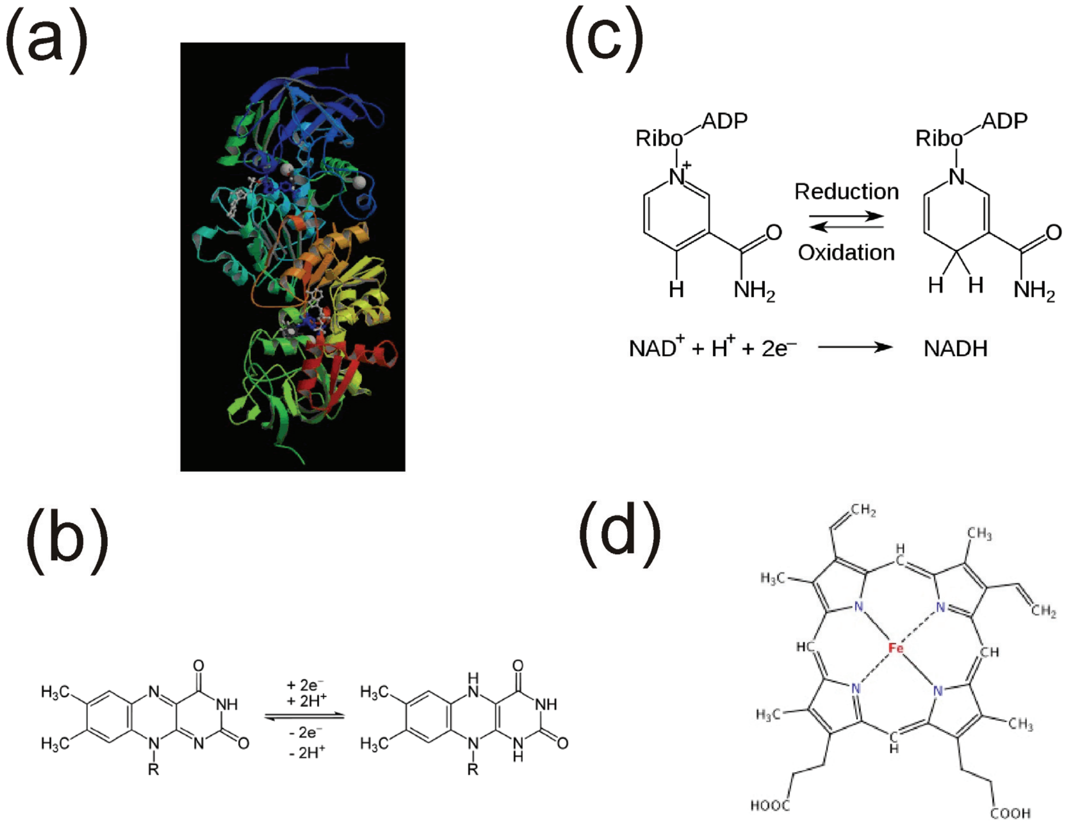

Figure 4.1 schematic diagrams of biomolecules (a) Three-dimensional structure of ADH which has two binding sites for NAD^+ and ethanol [127]. (b) Chemical structure of FAD/$FADH_2$, a cofactor of GOx. FAD is reduced to $FADH_2$ and the $FADH_2$ can be re-oxidized back to FAD by molecular oxygen [128]. (c) Chemical structure of NAD^+/NADH, a cofactor of ADH. NAD^+ is reduced in the form of NADH by accepting an electron and hydrogen and then NADH can be oxidized to NAD^+ by donating an electron and hydrogen [129]. (d) Chemical structure of FePP [92]. An iron ion at the center of a porphyrin ring can be oxidized (Fe^{3+}) or reduced (Fe^{2+}) in the electron transfer reactions.

4.2.2 Methods

Figure 4.2(a) is a schematic illustration of the enzymatic detector. It consists of a conventional three-electrode electrochemical cell modified with additional gating electrodes for applying an external voltage V_G to the working electrode, upon which molecules of a redox enzyme are immobilized. Enzymes and redox molecules are immobilized and confined within a working area of 1 mm × 1 mm defined by an insulating mask on the bare edge-plane of a HOPG electrode. A piece of 0.5 mm-diameter copper wire coated with a thin layer of insulator (enamel) (278-1345B, Radio Shack, TX) was used as the gaiting electrode. The wire was bent to form a U-shaped structure, which was attached on the working electrode next to the immobilized enzyme molecules using nonconductive epoxy (Dexter Corp., NJ) as shown in Figure 4.2(a). An alternative method was to selectively evaporate gold on an insulating layer formed on the working electrode next to the immobilized enzyme molecules. Both methods produced similar effects in this work. Enzyme immobilization on the edge plane of HOPG, as described previously [96], results in the formation of a sub-monolayer of enzyme on the electrode as revealed by atomic force microscopy (AFM) in Figure 4.2(b). It was shown that when GOx is immobilized on bare edge-plane of HOPG, its enzymatic activity is preserved [96]. Figure 4.2(c) shows the cross section profile of the location as indicated by the line in Figure 4.2(b), indicating the presence of the sub-monolayer of enzyme molecules.

Electrochemical measurements were controlled by an electrochemical workstation (CH Instrument 660C, Austin, USA). The enzyme-immobilized electrode and the

FePP-immobilized electrode were used as the working electrode. A commercial Ag/AgCl (saturated KCl) electrode was used as the reference electrode, and a platinum wire was used as the counter electrode. Cyclic voltammograms (CV) was obtained at various scan rates, pH values and buffer solutions. The buffer solution, if it needed, was deaerated by purging with pure nitrogen gas. Chronoamperometric measurement was performed at constant electrode potential as function of time. Control experiments performed with bare HOPG working electrode, the reference electrode and the platinum counter electrode showed no electrochemical response to the analyst such as glucose, ethanol, hydrogen peroxide and oxygen from a potential -1 V up to a potential as high as 1 V. Note that the results of electrochemical measurements presented in this work have been produced with several electrodes in repeated experimental runs and therefore reflect the typical characteristics of the electrodes used in making the corresponding measurements. The determination of detection limit was made according to signal/noise = 3.

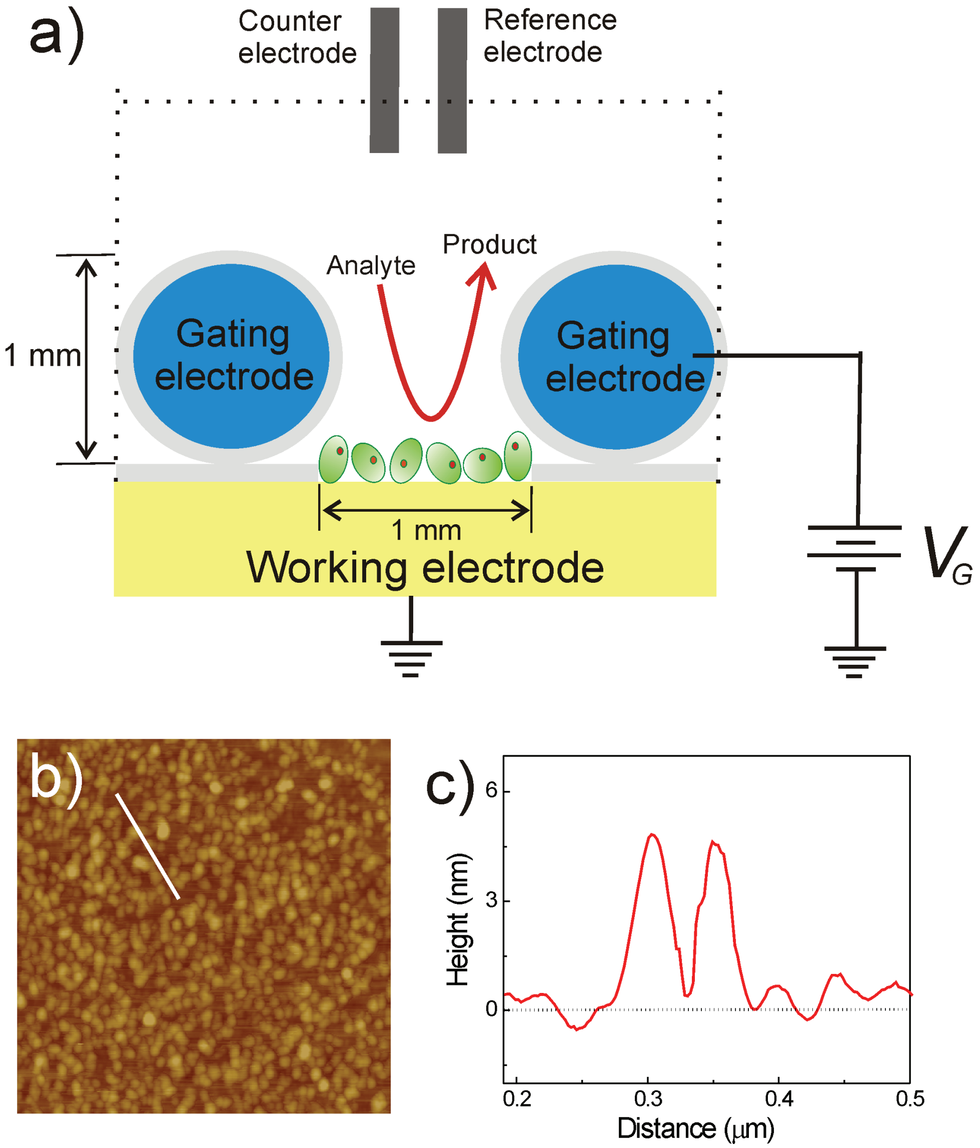

Figure 4.2 Schematic description of the enzyme transistor. (a) Each elliptical structure represents an enzyme molecule immobilized on the working electrode (not drawn to scale). The enzyme's active center is indicated by the smaller circle within a molecule. The gating electrode is indicated by thin insulator coated wires, which consist of a copper wire represented by the blue circles and the thin insulator indicated by the shaded shells. V_G is a voltage source used to produce an electric field at the interface between the sample solution and the working electrode (b) AFM image (1 μm × 1 μm) of a GOx-immobilized HOPG electrode, showing a sub-monolayer of GOx with scattered molecules forming the second layer. The molecule appears to be about three times larger than its actual size due to tip-induced convolution. (c) Cross-section profile of the location as indicated by the line in (b). The profile shows two GOx molecules and the electrode surface, indicating the presence of a sub-monolayer of enzyme molecules.

4.3 Results and discussions

4.3.1 Voltage-controlled bioelectro-oxidation of substrates – The field-effect enzymatic amplifying detector with pico-molar detection limit

The detection technique has been applied to two well-known enzyme systems. The GOx-glucose system plays an essential role in the making of glucose biosensors for the determination of glucose in blood, plasma and serum. The cyclic voltammograms (CV) in Figure 4.3(a) show the oxidation of glucose brought about by a GOx-immobilized electrode. The black CV is the background signal (electrode in phosphate buffer solution (PBS) only) and the red CV is the electrode's response to 3 mM of glucose, both CVs being obtained with $V_G = 0$ V. The inset shows two glucose calibration curves of the electrode obtained with $V_G = 0$ V but under different conditions (See below). The current values are evaluated at the potential of 0.8 V and the background has been subtracted from the data points so that the data points show the glucose oxidation current. The curves indicate the Michaelis-Menten kinetic behavior of the biocatalytic process. The glucose detection limit of the electrode is 200 μM, a typical value for glucose biosensors [96]. When V_G was increased from zero, the glucose oxidation current was found to increase significantly. The green CV and the blue CV of Figure 4.3(a) were obtained with $V_G = 0.02$ V in the absence of glucose and in the presence of 3 mM of glucose, respectively. Figure 4.3(a) shows that when V_G is applied, the CV of the electrode shows an increased charging current due to the double-layer capacitance of the electrode. In general, when the electrode potential is scanned at a given rate, the charging current is independent of the electrode potential within the potential range used here [38]. However, the observed fast increase in the electrode current as the potential is increased indicates that the major component of the electrode current is the biocatalytic current due to the oxidation of glucose. Figure 4.3(b) shows the relation between the glucose oxidation current (the detector's output signal current obtained by subtracting the background from the electrode's anodic current) and V_G. With 8 mM of glucose, the glucose oxidation current undergoes a 23-fold increase (amplification in the output current) as V_G is increased from 0 to a critical value (V_c) of 0.02 V. As V_G is increased beyond V_c, the current starts to decrease. It was observed that, for a given analyte, the value of V_c increases as the range of analyte concentration is lowered.

The applied voltage did not produce permanent or irreversible detrimental effect on the catalytic activity of the immobilized GOx. In the inset of Figure 4.3(a), the blue curve shows the electrode's response to glucose with V_G turned off after having been increased to 0.1 V. The blue curve almost coincides with the pink curve, which was obtained before applying V_G to the GOx molecules. The reversibility of the effect produced by the voltage on the bioelectrochemical detection is also reflected in Figure 4.3(b), where the arrows indicate the direction of varying V_G. This reversible characteristic is another manifestation that the field did not produce permanent detrimental effect on the enzyme. Note that the segment indicating the decreasing output current will be discussed below in Section 4.3.2.

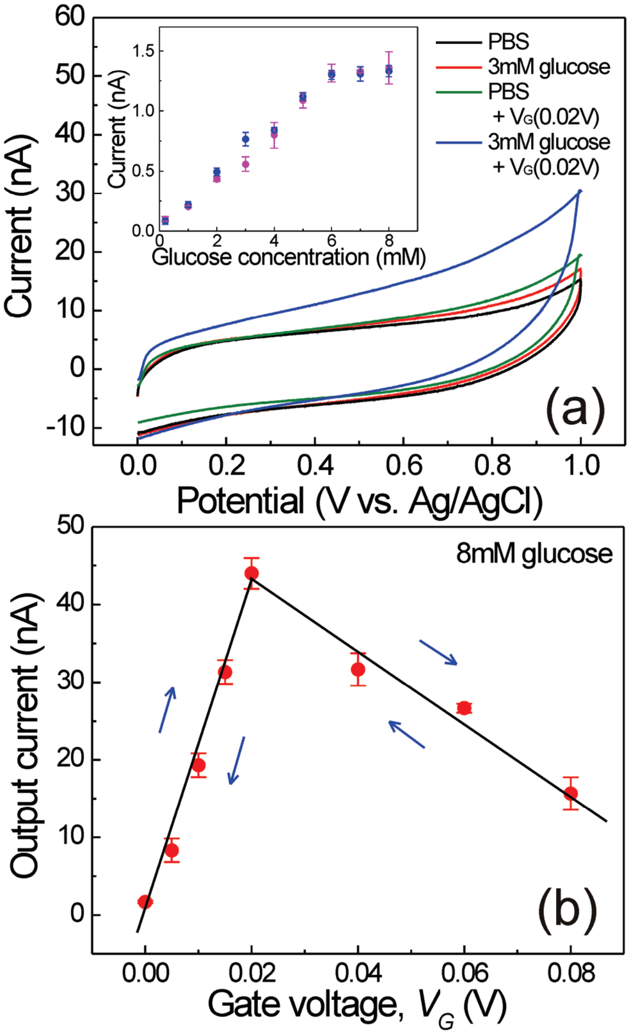

Figure 4.3 Electrochemical response of a GOx-immobilized electrode to glucose. (a) The black CV is the electrode's behavior in PBS. The red CV shows the electrode's response to 3 mM glucose. These CVs were obtained in the absence of the applied electric field ($V_G = 0$). The green CV and the blue CV were obtained with $V_G = 0.02$ V in the absence of glucose and in the presence of 3 mM of glucose, respectively. The inset shows two calibration curves of the electrode. The pink curve was obtained before applying any electric field to the GOx molecules. The blue curve was obtained with $V_G = 0$ after V_G has been increased to 0.1 V and returned to 0 V. The current values are evaluated at the potential of 0.8 V and the background has been subtracted from the data points so that the data points show the glucose oxidation current. (b) The relation between the glucose oxidation current and V_G at 8 mM of glucose. The currents were evaluated at a potential of 0.8 V. The background current has been subtracted. The arrows indicate the directions of the variation in V_G. The critical voltage V_c occurs at about 0.02 V.

The signal amplification allowed us to detect glucose at progressively lower concentration below the milli-molar range by increasing V_G. Figure 4.4(a) shows CVs of the electrode with $V_G = 0.04$ V. The black CV is the background signal and the red CV is the electrode's the response to 200 nM of glucose. Both CVs are obtained with $V_G = 0.04$ V. The inset of Figure 4.4(a) shows the glucose calibration curve in the nano-molar range with a detection limit 20 nM. In Figure 4.4(b), the black CV is the behavior of the electrode in PBS with $V_G = 0.06$ V and the red CV is the electrode's response to 500 pM glucose with $V_G = 0.06$ V. The inset of Figure 4.4(b) shows the glucose calibration curve in the pico-molar range obtained with $V_G = 0.06$ V. The calibration curve shows a detection limit of 100 pM with a detection resolution of 100 pM, which is demonstrated by the distinctive current values caused by increments of 100 pM in glucose concentration. The current values in the calibration curves as shown in Figure 4.4 are evaluated at the potential of 0.8 V. To estimate the observed detection limit, we estimate the magnitude of the oxidation current at the pico-molar glucose level, assuming that the two electrons released due to the oxidation of a glucose molecule can readily reach the electrode. The total charge transferred $Q = nFN$, where $n = 2$, F is the Faradaic constant, and N is the number of mole electrolyzed [35]. For 100 pM of glucose, $Q = 2 \times 10^{-8}$ C. The faradaic current ($i = \mathrm{d}Q / \mathrm{d}t$) is estimated to be 3.33 nA, using a time interval of 0.6 second, during which the anodic current increases noticeably as a result of scanning the cell potential from 0.5 V to 0.8 V. This is the maximum extractable current. The actual current should be much smaller than the estimated value, since the protein barrier reduces the tunnel rate.

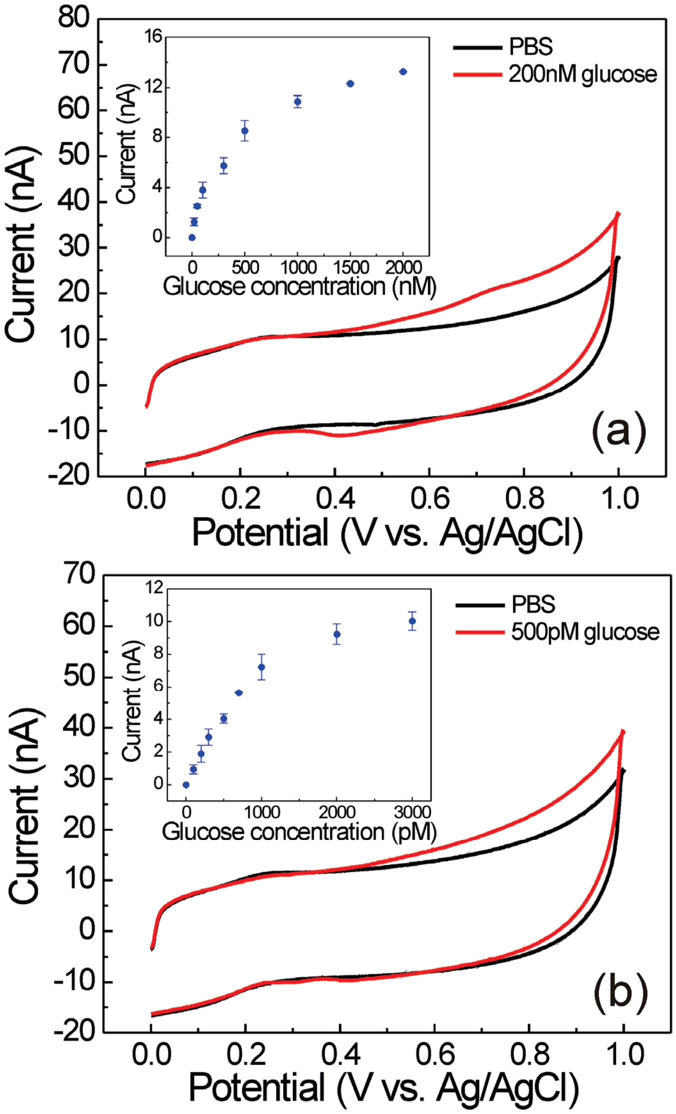

Figure 4.4 Field-induced enhancements in analyte detection. (a) The black CV is the electrode's behavior in PBS. The red CV shows the electrode's response to 200 nM glucose. These CVs are obtained with V_G = 0.04 V. The inset is the glucose calibration curve in the nano-molar range, which is evaluated at potential of 0.8 V (b) The black CV shows the background signal of the electrode in PBS and the red CV shows the electrode's response to 500 pM glucose with V_G = 0.06 V. The inset shows the glucose calibration curve in the pico-molar range, which is evaluated at the potential of 0.8 V

For enzymes immobilized on an electrode as shown in Figure 4.2(b), quantum mechanical tunneling gives rise to interfacial electron transfer [130]. It is known that the electronic energy profile of an insulating material can be modified by an electric field [131], and this effect has recently been used to construct a field-effect transistor using a non-electroactive protein as the active material [132]. The enhanced biocatalytic current due to V_G observed here is consistent with the scenario that the electronic energy profile of the tunnel barrier at the enzyme-electrode interface is modified by an electric field so that the tunneling rate is enhanced. In our experimental setup, V_G induces charge distributions at the interface between solution and the enzyme molecules as shown in Figure 4.5. For the oxidation of the analyst, when V_G is positive, negative charges are induced on the surface of the HOPG electrode and positive ions are induced at both the interface between the solution and the enzyme molecules and the interface between the solution and the bare electrode. However, only the positive charges distributed on the enzyme establish electric fields within the enzyme since the active site carries a negative charge due to the electron to be transferred. Figure 4.5 shows the fields associated with the arrangement of the induced charges. In Figure 4.5, only the ions that produce the fields relevant to the observed effect are shown. All other possible ion arrangements are irrelevant to the present discussion. Note that the strength of the field increases with the amount of induced charges, which in turn increases with the magnitude of V_G. Also, the induced ions are distributed on the electrode surface with a spatial dependence that is determined by the distribution of the potential caused by V_G on the electrode surface. The experimental conditions bear resemblance to that of the ion-selective field-effect transistor (ISFET), a standard sensing scheme for ions and biomolecules [116], in which the applied voltage between the reference electrode and the semiconductor substrate induces positive ions at the solution-membrane interface to form a capacitor structure with the negative charge induced within the semiconductor. The redox active site of an electroactive enzyme, i.e. the flavin adenine dinucleotide (FAD) of GOx or the NAD^+ of ADH, is surrounded by a polypeptide network, which reduces the rate of tunneling between the active site and the electrode. An electric field with the correct direction reduces the effective height of the tunnel barrier and therefore enhances the rate of tunneling [131]. In our experiment, the field established within the enzyme caused by applying a positive V_G to the gating electrode with respect to the working electrode lowers the effective height of the tunnel barrier (the polypeptide maze) as shown in Figure 4.5 and therefore increases the electron tunnel rate.

Figure 4.5 shows a conceptual electronic energy-band diagram of the enzyme-electrode interface. At equilibrium, no electron transfer occurs between the active site and the electrode, since the most probable energy of the occupied quantum state of the active site, E_{red}, is below the Fermi energy E_F of the electrode. When the cell potential of the electrode is raised, oxidation of the enzyme occurs as electrons are energetically allowed to be transferred from the E_{red} to the electrode. The electrode-active site system can be considered as a acceptor-donor pair, and, according to the Marcus theory of electron transfer [51], the electron transfer rate constant k_{et} depends critically on the distance d between the electrode and the active site as $k_{et} \propto \exp(-\beta d)$.

In general, this distance is large due to the thick tunnel barrier of the polypeptide network, which makes electron transfer rate negligibly small. However, the rate constant also depends on the value of the electron-coupling constant, β, which is determined by the effective height of the tunnel barrier. When V_G is turned on, the electric field caused by the induced charges described above distorts the top of the tunnel barrier (see the red dashed curve in Figure 4.5), reducing the effective height of the barrier and, therefore, resulting in a smaller value of β and a larger value of k_{et}. Thus, the observed enhancement in the oxidation current of the analytes (glucose and ethanol) and hence their significantly improved detection limits are likely to the result of the field-induced modification of the energy barrier for tunneling. Note that, to provide additional support for the proposed model described above, we have reversed the polarity of V_G and observed no glucose oxidation current even in the milli-molar range. This phenomenon corresponds to an increased effective tunnel barrier.

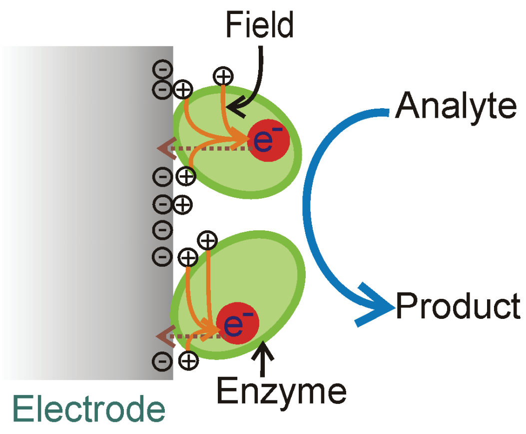

Enzyme-catalyzed oxidation of analyte

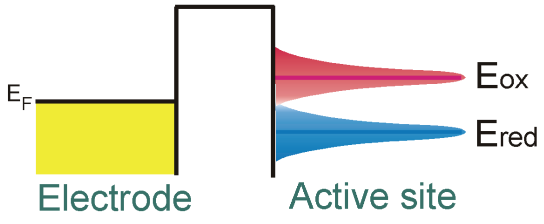

Electrode at equilibrium

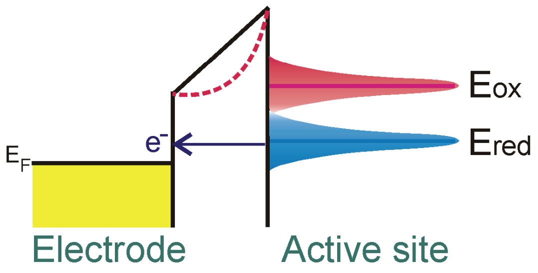

Electrode subjected to positive
cell potential and applied field

Figure 4.5 The effect of cell potential and induced electric field on interfacial electron transfer. The red dot is the active site of the enzyme. The induced charges are located on opposite sides of the enzyme to set up the field. The enzyme catalyzes the oxidation of the analyte, resulting in electrons e^- transferred to the active site. E_{red} and E_{ox} are respectively the most probable energies for the occupied and unoccupied quantum states of the active site. The Gaussian-shaped regions are the distributions associated with these energies. A positive cell potential raises E_{red} above E_F, energetically allowing electrons to be transferred to the electrode. The induced field distorts the tunnel barrier as indicated by the red dotted curve, resulting in enhanced transfer of electrons

To show that the enhanced analyte detection also occurs with other systems, we have applied it to the ethanol-ADH system. ADH is used as the sensing element of alcohol biosensors [133]. Figure 4.6(a) shows CVs of the ADH-immobilize HOPG edge-plane electrode. The black CV is the background signal and the red CV is the electrode's the response to 2 nM of ethanol. Both CVs are obtained with $V_G = 0.08$ V. The inst of Figure 4.6(a), the red dot is the ethanol calibration curve obtained with the electrode with $V_G = 0$ V. The detection of ethanol is in the milli-molar range with a detection limit of 0.6 mM. The blue dot is the calibration curve of ethanol in the nano-molar concentration range with a detection limit of 0.5 nM achieved with $V_G = 0.08$ V. Above the detection limit, increments of 0.5 nM in ethanol concentration result in distinguishable current values. Figures 4.3, 4.4 and 4.6 show that, by using V_G, the current level of the detection signal for the wide range of analyte concentration studied can be controlled in the nano-ampere range for convenient electronic signal processing.

The field-enhanced glucose detection in the presence of physiological interfering substances has been carried out in order to show that the substance selectivity of GOx is not compromised by the presence of the field. Figure 4.6(b) shows that, with the field produced by $V_G = 0.06$ V, the response of a GOx-immobilized electrode to 500 pM of glucose (the blue CV) is almost indistinguishable from that for which 1 μM of ascorbic acid (AA) and 1 μM of uric acid (UA), which are major interfering substances in the body fluid for glucose detection, are present with the 500 pM glucose in the cell (the red CV). Thus, the substance selectivity of GOx (enzyme's specificity for its analyte) has not been affected by the electric field in the presence of interfering substances, whose concentration are 10^3 times higher than that of glucose (the analyte). Note that at the physiological level, the ratio of these interfering substances to glucose is less than unity [134].

In summary, we have constructed an enzymatic detector, which provides voltage-controlled current amplification, and demonstrated its application in ultrasensitive biological detection [135]. The application of the technique to two enzymatic systems indicates that this technique can be used as a generalized approach to achieve ultrasensitive amperometric biodetection. The fact that the detector's output current is controlled by a voltage applied at a third electrode suggests that the detector is a field-effect transistor, whose current-generating mechanism is the conversion of an analyte to a product using an enzyme as catalyst. In a more general sense, our results show that a redox enzymatic reaction can be controlled externally. Our study echoes with a recent study on using hydrostatic pressure to control hydrogen tunneling in enzymes [136].

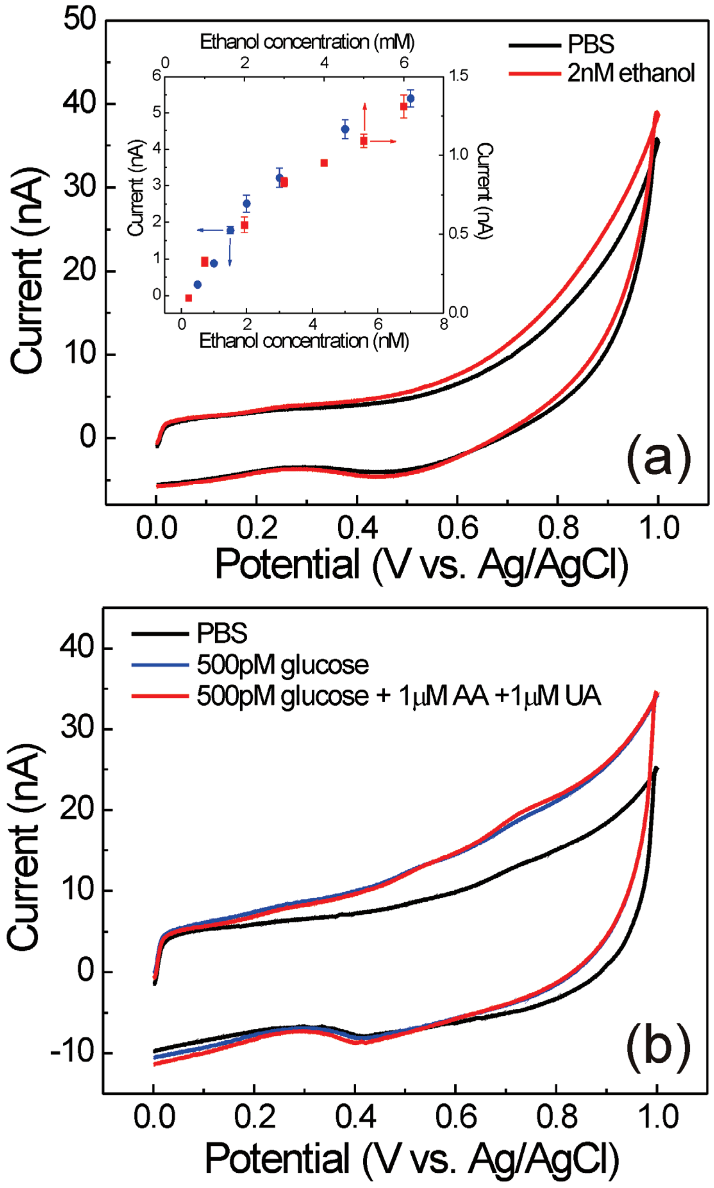

Figure 4.6 The field-enhanced ethanol and glucose detection (a) CVs of the ADH-immobilize HOPG edge-plane electrode. The black CV is the background signal and the red CV is the electrode's the response to 2 nM of ethanol. Both CVs are obtained with V_G = 0.08 V. The ethanol calibration curves of the electrode as shown in the inset obtained with V_G = 0 V (red dot) and V_G = 0.08 V (blue dot). The current values are evaluated at a cell potential of 0.8 V. (b) The black CV is obtained using the GOx-immobilized electrode in PBS with V_G = 0.06 V. The blue CV shows the electrode's response to 500 pM of glucose in PBS and the red CV shows the electrode's response to 500 pM of glucose in the presence of 1 μM of AA and 1 μM of UA. Both the blue and red CVs were obtained with V_G = 0.06 V.

4.3.2 Voltage-controlled ultrasensitive biodetection beyond pico-molar range

The field-induced enhancement in analyte detection at extremely low concentration up to zepto-molar range was studied by further increasing V_G. Figure 4.7(a) shows the field-induced glucose detection in the atto-molar (10^{-18} M) range with the field produced by $V_G = 0.12$ V. The calibration curve in the inset shows that the detection limit under this particular condition is 5 aM. Above the detection limit, increments of 5 aM, 10 aM, 20 aM and 30 aM in glucose concentration result in distinguishable current values. Detection of glucose in the zepto-molar (10^{-21}M) concentration range was obtained with $V_G = 0.15$ V as shown in Figure 4.7(b). The calibration curve in the inset shows a detection limit of 50 zM with a detection resolution of 50 zM. The error bars show that the current of each data point distinctively represents the corresponding concentration. Figure 4.7(c) shows the temporal dependence of the electrode's response to several glucose concentrations. The rates of the current decay are qualitatively consistence with the amount of glucose in the cell. In particular, the 1/e level is reached in 1 s, 1.2 s and 1.4 s for 100 zM, 300 zM and 500 zM, respectively. These short time constants reflect the minute amounts of glucose in the sample.

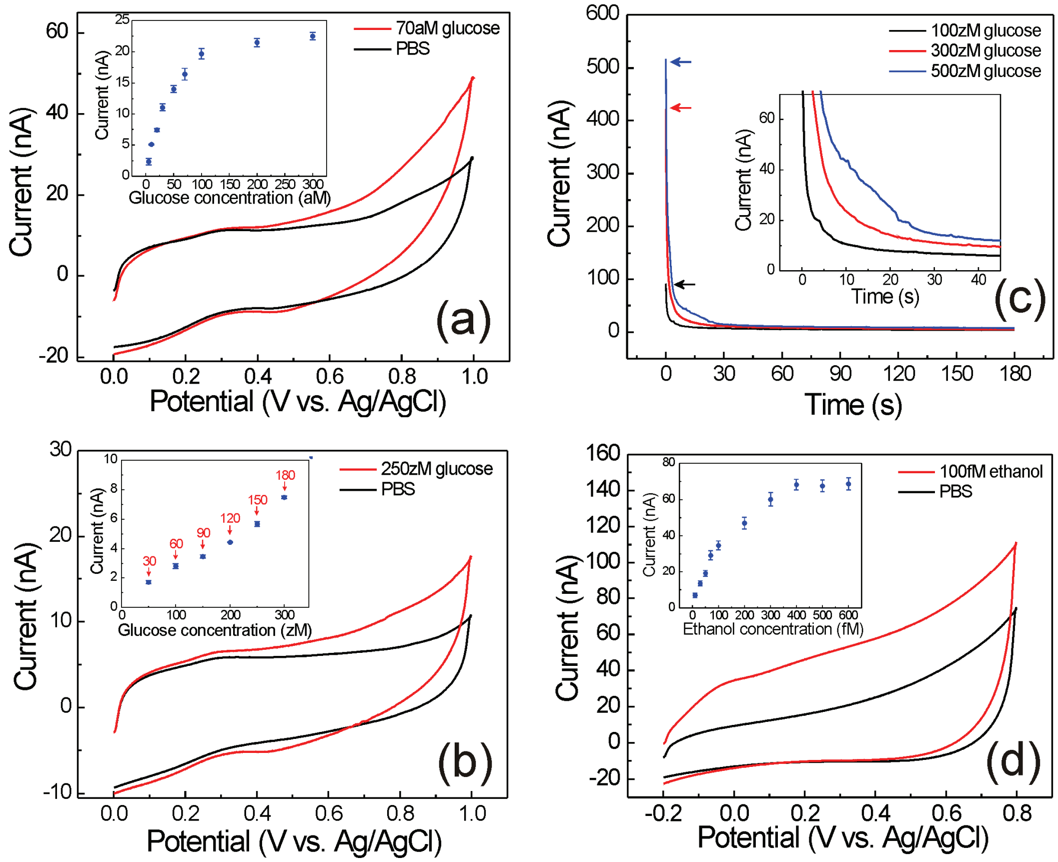

Figure 4.7 Field-induced analyte detection in extremely low concentration. (a) The black CV is the electrode's behavior in PBS. The red CV shows the electrode's response to 70 aM glucose. These CVs are obtained with V_G = 0.12 V. The inset shows the calibration curve of the electrode in the atto-molar range. The current values are evaluated at potential of 0.9 V (b) The black CV shows the background signal of the electrode in PBS and the red CV shows the electrode's response to 250 zM glucose with V_G = 0.15 V. The inset shows the glucose calibration curve in the zepto-molar range, which is evaluated at the potential of 0.9 V (c) The current of the electrode as in (a) is monitored in the time in different glucose concentration in the zepto-molar range at a potential of 0.8 V and with V_G = 0.15 V. The arrows indicate the initial current for each glucose concentration. The inset shows the details of the temporal decays. (d) Femto-molar detection of ethanol using ADH-immobilized HOPG electrode with V_G = 0.15 V. The inset is the electrode's calibration curve for ethanol obtained at a potential of 0.7 V

To show that the field-induced detection at extremely low concentration does not only occur with the glucose-GOx system, we have applied this technique to the ethanol-ADH system. Figure 4.7(d) shows the detection of ethanol using ADH-immobilized edge plane HOPG electrode in the femto-molar (10^{-15} M) concentration range achieved with $V_G = 0.15$ V. The calibration curve in the inset indicates an ethanol detection limit of 10 fM. Above the detection limit, increments of 25 fM in ethanol concentration result in distinguishable current values.

The applied electric field used did not produce permanent or irreversible detrimental effect on the catalytic activity of the GOx, and it is likely that the conformation of the enzyme remained unaltered. However, we noticed that the applied field can produce a temporary reduction in the catalytic current. In Figure 4.8, the glucose oxidation currents of a GOx-immobilized electrode are plotted versus V_G for atto-molar range detection. The plot shows that the current increases to a maximum value at $V_c = 0.12$ V, after which it decreases with further increase in V_G. When V_G is reversed, the currents follow almost the same path to the original value as indicated by the arrows. This phenomenon also appears in other glucose concentration ranges (see Figure 4.3 (b)). This effect suggests that a certain amount of the GOx molecules can be temporarily "disabled" by the field due to an unknown mechanism, which occurs when the field becomes high enough. Nevertheless, this reversible characteristic is a manifestation that the field did not produce permanent detrimental effect on the enzyme.

The calibration curves in the insets of Figures 4.7(a) and 4.7(b) show current saturation due to the Michaelis-Menten kinetics. According to Figure 4.3(a), saturation should not occur at such low analyte concentration. Here, we present a possible scenario, in which this peculiar effect could be the result of the mechanism for the temporary loss of enzymatic activity described above. Since the enzymes carry charges on their surfaces [84,121], the field may re-orient them or change their conformation so that they are "disabled" in carrying out their enzymatic activities, the result of which is diminished catalytic activity or interfacial tunneling or both. This is referred to as the "unfavorable effect". Assuming the enzyme molecules have different state of immobilization in terms of orientation and flexibility on the electrode surface, which is likely to occur with the method of immobilization used here, the "unfavorable effect" may "disable" the molecules with different field strengths produced by V_G. Before the "unfavorable effect" shows pronounced effect, the "favorable effect", which is the field-induced modification of the tunnel barrier, still enhances the oxidation current. As the field is increased, the tunnel current increases due to the "favorable effect". When the field is increased beyond V_c, a certain amount of enzyme molecules are "disabled" due to the "unfavorable effect" and the number of functioning enzyme molecules on the electrode is reduced. In the milli-molar range of glucose detection, V_c occurs at about 0.02 V as shown in Figure 4.3(b). Suppose that the analyte concentration is now reduced to a lower range. If the field is further increased, more enzyme molecules will be "disabled". However, for the molecules that are not affected, the "favorable effect" still induces the enhancement in the tunnel current with the functioning enzyme molecules, and under the condition that the analyte concentration is low enough, a continuation of the region, in which the oxidation current increases with increasing V_G, will occur beyond the V_c until a new and higher value of V_c is reached. Figure 4.8 shows that in the atto-molar range of glucose detection, the new V_c is about 0.12 V. Now, if the analyte concentration is increased, saturation in the oxidation current occurs due to the much reduced number of enzyme molecules.

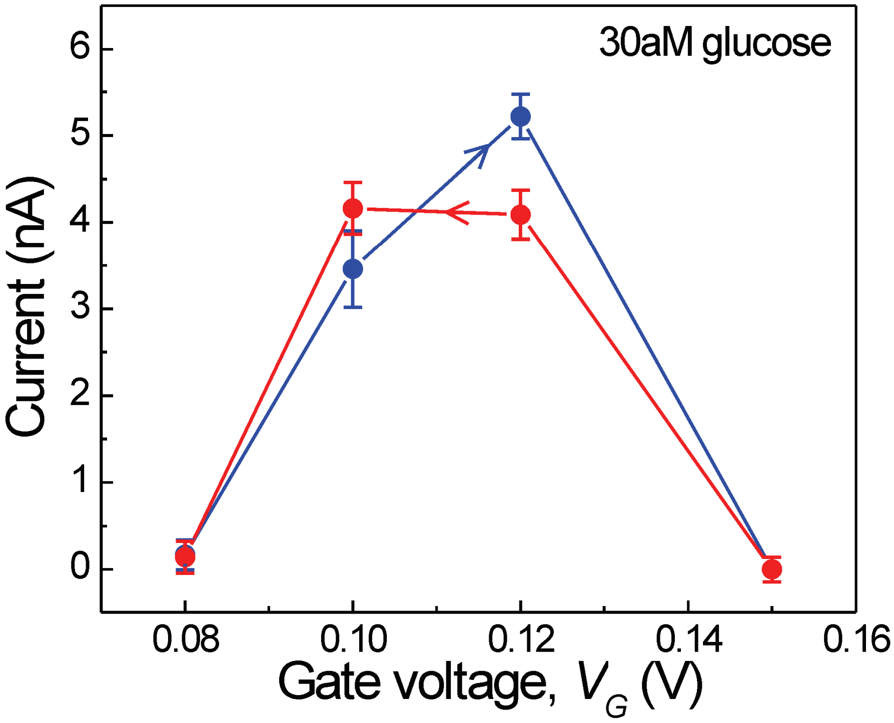

Figure 4.8 The reversible effect of field on oxidation current. The glucose oxidation current is plotted versus V_G for 30 aM of glucose. The critical voltage V_c occurs at about 0.12V.

The field-induced improvement of detection limit can be expected with general nanoscale electroactive objects. However, in enzymatic biosensing, substance selectivity should not be compromised by any detection maneuver. It was observed that the selectivity of GOx for glucose in the presence of an electric field is retained even in extreme low glucose concentrations. Figure 4.9 shows that, with the field produced by $V_G = 0.12$ V, the response of a GOx-immobilized electrode to 100 aM of glucose (the blue CV) is almost indistinguishable from that for which 1nM of ascorbic acid (AA) and 1 nM of uric acid (UA), which are interfering substances in the body fluid, are present with the 100 aM glucose in the cell (the red CV). Thus, the substance selectivity of GOx (enzyme's specificity for its analyte) has not been affected by the electric field in the presence of interfering substances, whose concentration are 10^7 times higher than that of glucose (the analyte). Note that at the physiological level, the ratio of these interfering substances to glucose is less than unity [134,137].

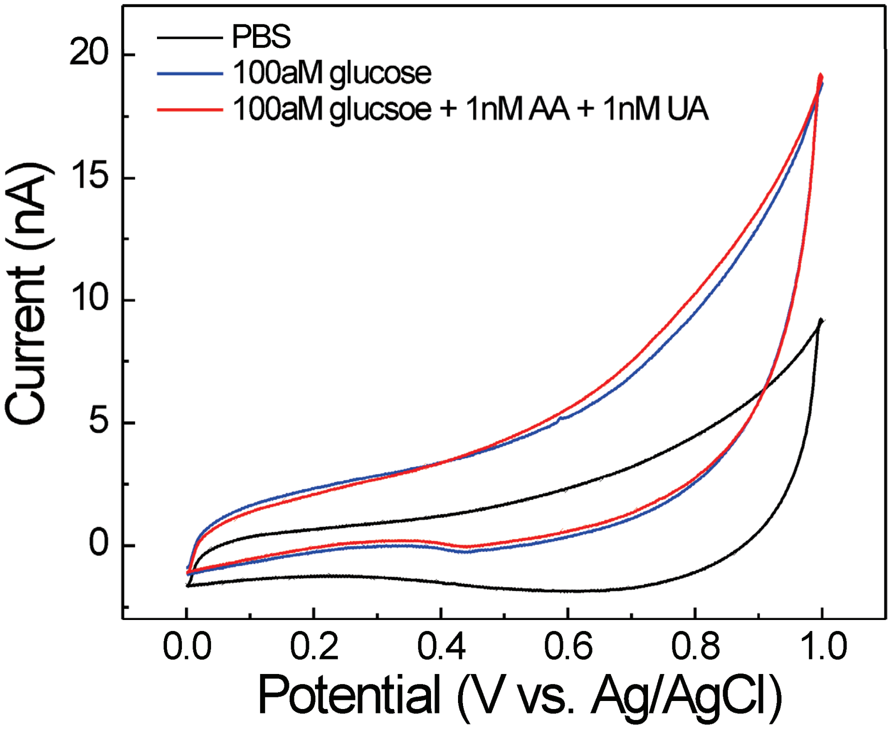

Figure 4.9 The preserved enzymatic selectivity of GOx under the influence of field. The CVs of a GOx-immobilized electrode were obtained with $V_G = 0.12$ V. In addition to producing biocatalytic currents in response to the presence of 100 aM of glucose (the blue CV), the electrode also shows the selectivity for glucose in the presence of 1 nM of AA and 1 nM of UA (the red CV).

In this section, we have demonstrated the field-induced ultrasensitive biodetection of glucose and ethanol at extremely low concentrations. The calibration curves in Figures 4.7(a) and 4.7(b) clearly indicate that, in the atto and zepto molar analyte concentration range, the detector's output current changes as the analyte concentration is changed. However, an experimental condition raises contradiction. In Figure 4.7 (b), each data point is associated with the number of glucose molecules in the cell caused by the corresponding glucose concentrations as indicated by the red numbers in the inset. In particular, the system was able to detect a minimum of 30 glucose molecules present in the cell and showed response to each incremental change in the unit of 30 glucose molecules in the cell. The total charge transferred Q is estimated to be 10^{-17} C by 30 glucose molecules in the cell so that the current is estimated to be 2.5 aA, using a time interval of 0.4 second during which the anodic current increases noticeably as a result of scanning the cell potential from 0.8 V to 1.0 V. However, the detection current observed up to zepto-molar range is on the nA level. A possible explanation for this contradiction is that the field-induced glucose oxidation reaction at higher V_G (~ 0.15 V) may become complex. First, higher V_G causes large downward distortion of the barrier so that the electron transfer rate from the active site of the enzyme to the electrode is high. When being oxidized, glucose instantaneously forms glucono lactone. Since FAD is also a cofactor for oxidation of glucono lactone [138] and the FAD is readily available (due to the high rate of electron transfer from the FAD to the electrode) to carry out the oxidation of glucono lactone, more current will be produced. A second possible scenario involves stripping electrons directly from glucose. At higher V_G (~ 0.15 V), the conductance between the active site and the electrode becomes larger so that the active site is in effect electrically connected to the electrode. Therefore, the active site and the electrode form a complex, which is capable of stripping electrons from glucose. Previous observation shows that 18 electrons can be extracted [139]. These possible processes individually or combined may contribute the observed enhanced oxidation current. The last possible scenario is a cyclic reaction of gluconic acid to glucono lactone as shown in Figure 4.10(a). GOx and glucose form a GOx-glucose complex before the reaction. Glucose is oxidized to glucono lactone which remains the complex form due to the high rate of electron transfer from the FAD to the electrode. Glucono lactone in the complex is hydrolyzed to gluconic acid spontaneously and then gluconic acid undergoes lactonization into glucono lactone [140]. Thus, the cyclic reaction of gluconic acid to glucono lactone could take place in the complex, which generates enhanced oxidation current. During the cyclic reaction, the complex act as a molecular machine supplying continuous electrons [141].

The ethanol detection current observed up to femto-molar range is on the nA level. Similarly, the field-induced ethanol oxidation reaction at higher V_G (~ 0.15 V) may involve stripping electrons directly from ethanol as explained above. Previous observation shows that 12 electrons can be extracted [61]. The cyclic reaction of ethanol is also suggested as shown in Figure 4.10(b). In an ADH-ethanol complex, ethanol is oxidized to acetaldehyde. In some part of ADH and unoccupied ADH, acetaldehyde can be reduced to ethanol by a streochemically cryptic reduction reaction of ADH [142]. Therefore, the cyclic reaction of ethanol to acetaldehyde may occur, which produces enhanced oxidation current. These possible processes individually or combined may contribute the observed enhanced oxidation current. Further investigation on electrooxidation of glucose and ethanol at extremely low concentration is needed to elucidate the measured enhanced current.

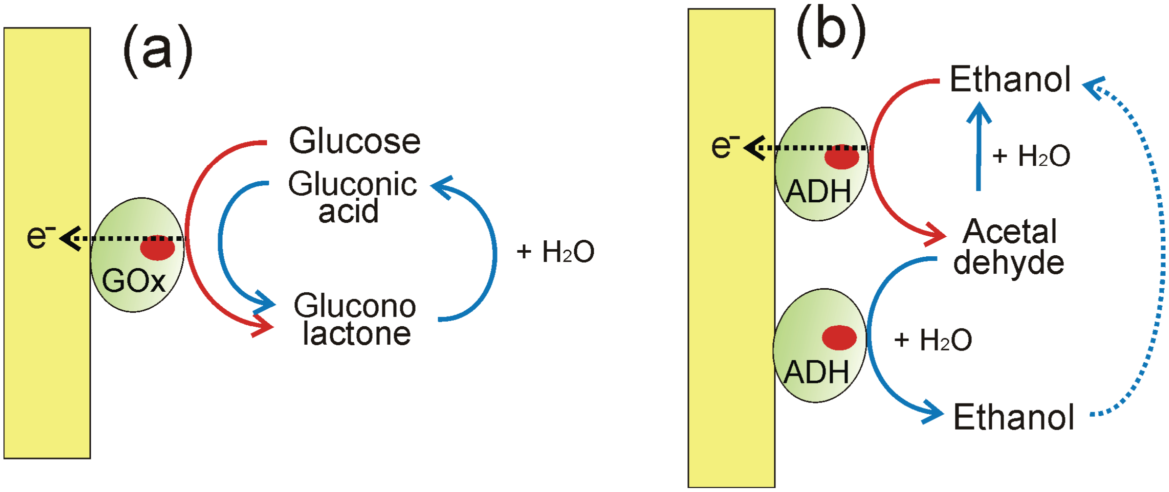

Figure 4.10 The possible mechanism for enhanced oxidation current of glucose and ethanol. (a) The cyclic reaction of gluconic acid to glucono lactone. The red dot is the active site of the enzyme. Glucose is oxidized to glucono lactone which remains the complex form. Glucono lactone in the complex is hydrolyzed to gluconic acid spontaneously and then gluconic acid undergoes lactonization into glucono lactone. Thus, the cyclic reaction of gluconic acid to glucono lactone generates enhanced oxidation current. (b) The cyclic reaction of ethanol. In an ADH-ethanol complex, ethanol is oxidized to acetaldehyde. In some part of ADH and unoccupied ADH, acetaldehyde can be reduced to ethanol by a streochemically cryptic reduction reaction of ADH. Therefore, the cyclic reaction of ethanol to acetaldehyde may occur, which produces enhanced oxidation current.

4.3.3 Voltage-controlled bioelectro-reduction of hydrogen peroxide - controlling electron transfer and reaction kinetics of the biological catalytic systems

Electron transfer is a fundamental process for important biological phenomena such as photosynthesis, respiration and metabolism. Effectively controlled electron transfer is one of the primary regulation mechanisms in biology and biomolecular machines [143,144], while efficiently controlled reaction kinetics of biological catalysis is an essential requirement for viable renewable and green energy processes [145]. Long-range electron transfer (LRET) occurs over a distance on the order of 10 Å in biological systems [47], where electrons tunnel between electroactive donors and acceptors through polypeptide networks. The rate constant of tunneling between a pair of weakly coupled donor and acceptor k_{et} depends critically on two quantities as [50],

$$k_{et} \propto \exp(-\beta d) \qquad (4.1)$$

where d is the distance through the insulating barrier between the donor and the acceptor and β is the attenuation coefficient which is proportional to the square root of the tunnel barrier height ($\beta \propto (\Phi_o)^{1/2}$) [50]. The LRET formalism is used in the pathway model of electron transfer in the biological systems to describe the strength of both through-bond [52] and through-space [47] coupling routes from donor to acceptor [53]

In Sections 4.3.1 and 4.3.2, it is shown that applying V_G to immobilized enzymes results in enhanced interfacial electron transfer. In this section, interfacial electron transfer is studied systematically. First, the effect of V_G on the redox property of FePP, a common redox organic molecule, is studied in order to show that the tunnel barrier at the enzyme-electrode interface indeed can be modulated by V_G. FePP has an electrocatalytic property for reducing oxygen [126]. In addition, FePP as a heme (Fe^{2+}/Fe^{3+}) forms a prosthetic group of a number of proteins such as hemoglobin and cytochrome c that are often encountered in biological electron transfer processes [126]. These heme-containing proteins exhibit a wide range of biological functions, including simple electron transfer reactions, oxygen transport and storage, oxygen reduction to the level of hydrogen peroxide or water, and the reduction of hydrogen peroxides [90].

Then, the effect of V_G on the electron transfer associated with the reduction of hydrogen peroxide (H_2O_2) catalyzed by microperoxidase-11 (MP-11), a redox biomolecule, is studied. MP-11 and H_2O_2 is an important bio-catalytic system. MP-11 is a heme-containing oligopeptide that consists of the active site microenvironment of cytochrome c, an electron transfer protein for many redox enzymes. H_2O_2, a strong oxidizing agent, is produced in organisms as a byproduct of oxygen metabolism. MP-11 catalyzes the reduction of hydrogen peroxide to water [90] and therefore reduces oxidative stress. The most important conclusion of this work is the nonlinear dependences of the kinetic parameters of the catalysis on the voltage, implying an efficiently controlled substance conversion process.

The redox reaction of FePP immobilized on an electrode has been intensively studied [146]. CVs of a HOPG electrode immobilized with FePP were obtained under different conditions as shown in Figure 4.11(a). The CVs were obtained in 10 mM SBS at pH 10. The green dotted lines are used to indicate the baselines of the peaks and the peak heights. The black CV, obtained with $V_G = 0$ V, shows a pair of redox peaks with a formal potential of $E^0 = -0.5$ V (vs. Ag/AgCl), indicating the molecule's reversible electron transfer (redox) reaction with the electrode, in which Fe^{3+} is reversibly reduced to Fe^{2+} as previously reported [146]. When V_G is varied to 0.2 V, the corresponding red CV shows that the heights of the redox peaks are increased. The blue CV corresponds to a more positive V_G of 0.8 V. It shows further increases in the heights of the peaks. The inset shows this dependence of the peak heights on V_G. The double-arrowed line is used to indicate the reversibility of this dependence. Therefore, the inset shows the manipulation of the interfacial electron transfer.

The effect of V_G on the electrocatalytic property of FePP to oxygen is shown in Figure 4.11(b). The CVs are obtained in 10 mM SBS at pH 10. Figure 4.11(b) shows the electro-reduction activity of the FePP-immobilized electrode for O_2 in the absence and presence V_G. The black CV shows the electrode's behavior in the absence of O_2 and V_G. The red CV was obtained in the presence of O_2, indicating the electro-reduction of O_2 in the absence V_G. When V_G was turned on, the height of redox peak is increase as shown in the blue CV. In the presence of V_G and O_2, the reduction current further increased as reflected in the green CV. This effect is the result of the gating voltage which reduces the effective tunnel barrier height.

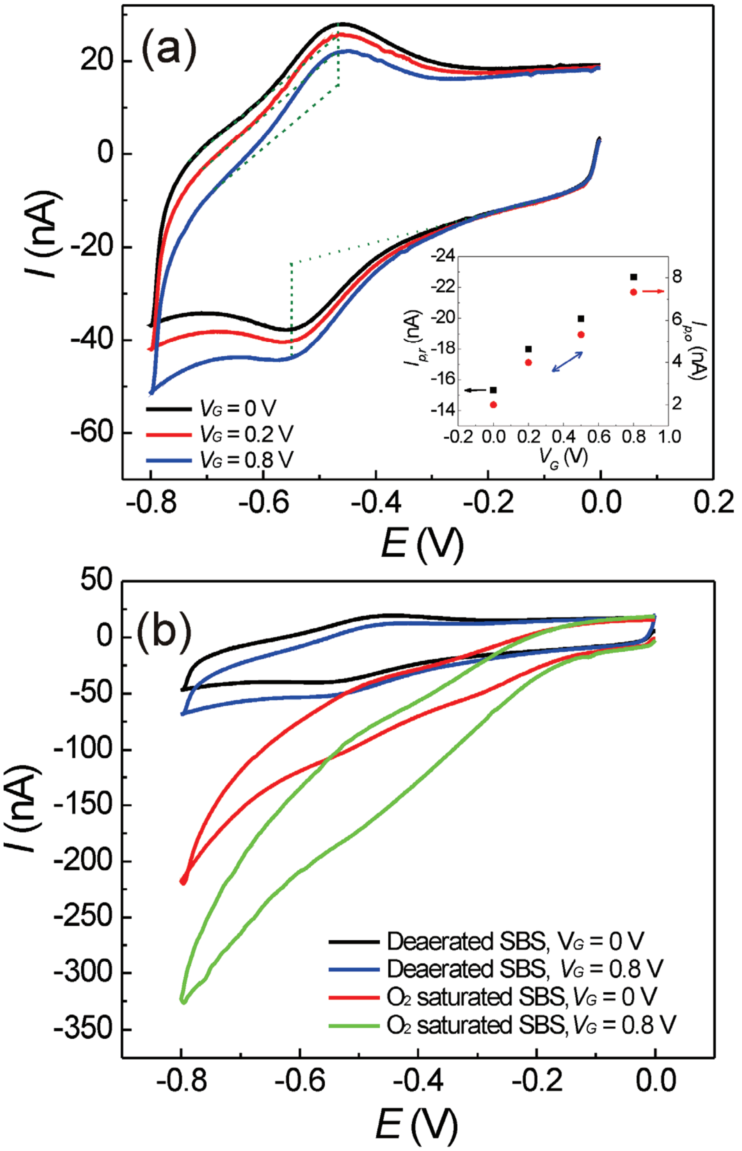

Figure 4.11 The effect of V_G on the redox properties of FePP immobilized on an electrode. (a) The CVs were obtained in 10 mM SBS at pH 10. The green dotted lines are used to indicate the baselines of the peaks and the peak heights. The inset shows the manipulation of the redox peak currents by varying V_G. $I_{p,o}$ and $I_{p,r}$ are the peak currents of the oxidation peak and the reduction peak, respectively (b) the Electro-reduction activity of the FePP-immobilized electrode. The black CV and blue CV show the redox peak of FePP in the absence and presence of V_G, respectively. The black CV and blue CV are obtained in deaerated 10 mM SBS at pH 10. The red CV and green CV show the electro-reduction of the electrode for O_2 in the absence and presence of V_G, respectively. The red CV and green CV are obtained in O_2 saturated 10 mM SBS at pH 10.

The enhanced redox peak currents due to V_G observed here is consistent with the scenario already described in Section 4.3.1 that the electronic energy profile of the tunnel barrier at the molecule-electrode interface is modified by an electric field so that the tunneling rate is enhanced. In this experimental setup, negative charges are induced on the surface of the HOPG electrode and positive ions are induced at both the interface between the solution and the molecules and the interface between the solution and the bare electrode as shown in Figure 4.12(a). However, only the positive charges distributed on the molecules establish electric fields within the molecule since the electrode carries negative charges induced by V_G. The active site of a redox molecule is usually surrounded by a molecular network, which is non-electroactive and therefore forms the tunneling barrier between the site and the electrode. An electric field with the correct direction reduces the effective height of the tunnel barrier and therefore enhances the rate of tunneling [131].

Figure 4.12(b) shows a conceptual electronic energy-band diagram of the molecule-electrode interface. At equilibrium, no electron transfer occurs between the active site and the electrode, since the most probable energy of the unoccupied quantum state of the active site, E_{ox}, is above the Fermi energy E_F of the electrode. When the potential of the electrode is lowered, reduction of the molecule occurs as electrons are energetically allowed to be transferred from the electrode to E_{ox}. The electrode-active site system can be considered as a acceptor-donor pair, and, according to the LRET formalism described above, $k_{et} \propto \exp(-\beta d)$. In general, d can be large so that electron transfer is diminished. The size of the non-electroactive part for FePP is about 5 Å , while that for MP-11 is about 12 Å (see below), which is long for LRET so that electron transfer is low. However, in our experiment, the electron-coupling constant, β, which is determined by the effective height of the tunnel barrier, can be reduced using the electric field created by the induced ions as the result of applying V_G as described above. The field distorts the top of the tunnel barrier (see the red dashed curve in Figure 4.12(b)), reducing the effective height of the barrier and, therefore, resulting in a smaller value of β and a larger value of k_{et}. Thus, the observed enhancement in the redox peak currents of the immobilized FePP, the reduction current of O_2 catalyzed by FePP and the reduction current of H_2O_2 catalyzed by MP-11 (see below) are likely to result in the field-induced modification of the energy barrier for tunneling.

To provide additional support for the model described above, we performed cyclic voltammetry of an HOPG electrode immobilized with FePP as shown in Figure 4.13(a). The black CV, obtained with $V_G = 0$ V, shows a pair of redox peaks, indicating the molecule's reversible electron transfer (redox) reaction, in which Fe^{3+} is reversibly reduced to Fe^{2+}. When V_G is varied to -0.05 V, the corresponding red CV shows that the heights of the redox peaks are decreased. The blue CV and the purple CV correspond to more negative V_G of -0.1 V and -0.4 V, respectively. Theses CVs show further decrease in the heights of the peaks. The Figure 4.13(b) shows this dependence of the peak heights on V_G. The peak currents of the redox peaks of FePP decrease as the magnitude of the reversed voltage increases, indicating an increased effective height of the tunnel barrier.

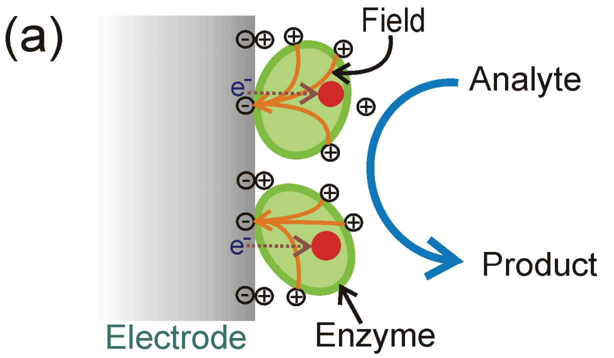

Enzyme-catalyzed reduction of analyte

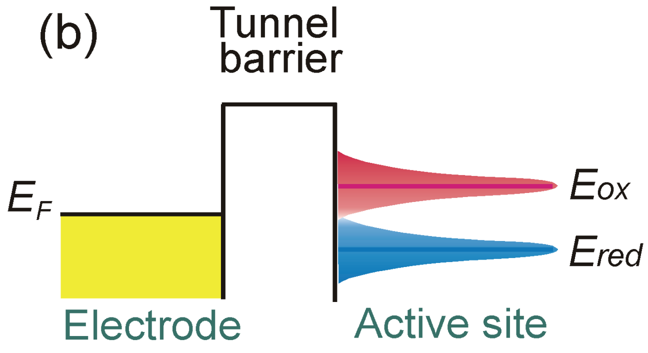

Electrode at equilibrium

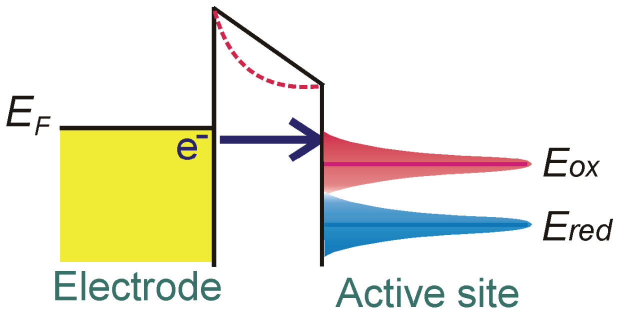

Electrode subjected to negative cell potential and postive field

Figure 4.12 Illustration of the principle of the field-modulation technique. (a) The ion-induced electric field at the solution-electrode interface. Each elliptical structure represents a redox molecule, whose active center is indicated by the smaller red circle within a molecule. (b) Energy profile of the molecule-electrode interface. E_{red} and E_{ox} are respectively the most probable energies for the occupied and unoccupied quantum states of the active site. The Gaussian-shaped regions are the distributions associated with these energies. E_F is the Fermi energy of the electrode. A negative cell potential raises E_F above E_{ox}, energetically allowing electrons to be transferred to the molecule. The induced field distorts the tunnel barrier as indicated by the red dotted curve, resulting in enhanced transfer of elect

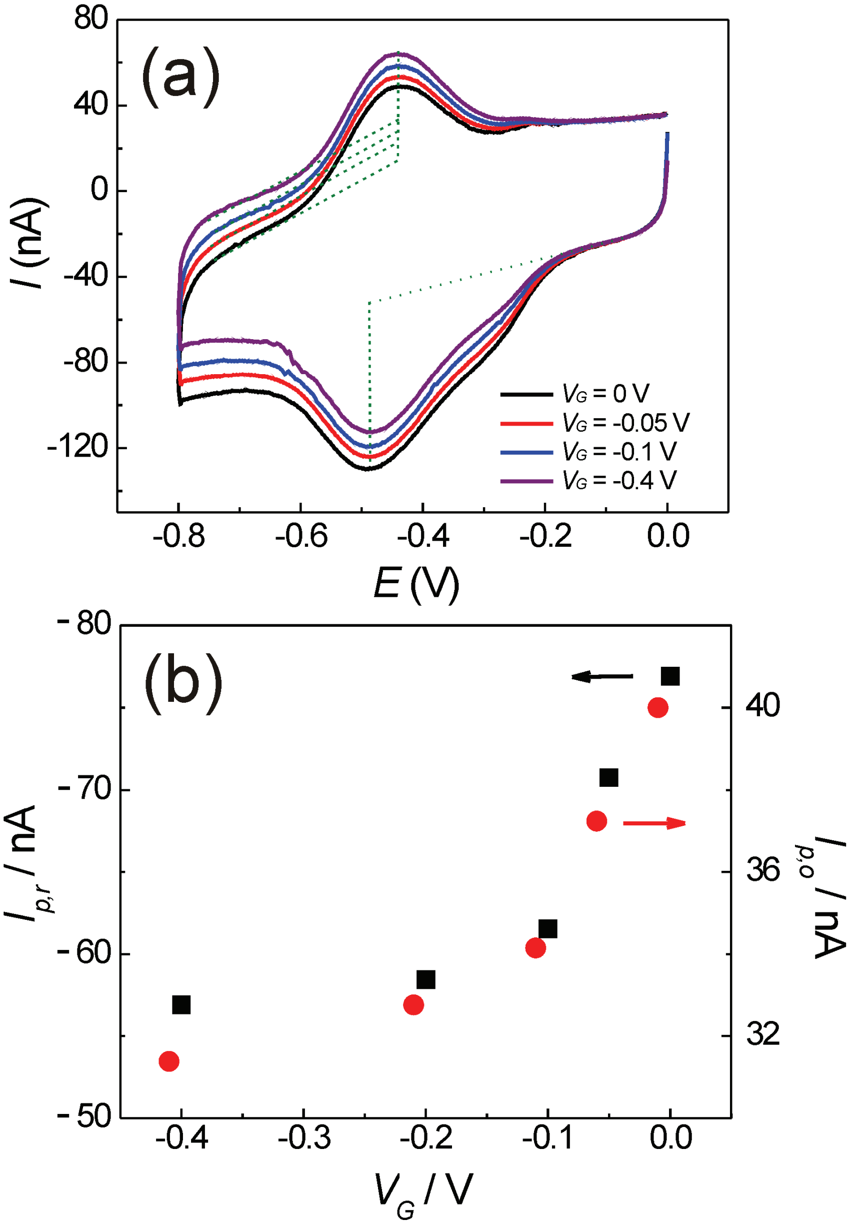

Figure 4.13 The effect of reversing the polarity of V_G on the redox properties of immobilized FePP. (a) The CVs were obtained in 10 mM SBS at pH 10 with V_G. The green dotted lines are used to indicate the baselines of the peaks and the peak heights. (b) The dependence of the peak heights on V_G. $I_{p,o}$ and $I_{p,r}$ are the peak currents of the oxidation peak and the reduction peak, respectively. The peak heights of the redox peaks of FePP decrease as the magnitude of the reversed voltage increases, indicating an increased effective height of the tunnel barrier.

The redox properties of MP-11 immobilized on an electrode was characterized. Figure 4.14(a) shows the CVs obtained with a MP-11-immobilized electrode at various scan rates of the potential in the absence of H_2O_2. The well-defined redox peaks indicate a formal potential of $E^0 = -0.31$ V (vs. Ag/AgCl) as observed in the literature [147]. The Figure 4.14(b) shows the dependence of the peak currents on the scan rate. With the scan rate increased from 10 mV/s to 200 mV/s, the redox peak currents show a linear dependence on the scan rate, indicating that the MP-11 molecules that were communicating electrically with the electrode were immobilized on the electrode [148]. The number of electrons exchanged, n, between the MP-11molecule and the electrode can be estimated using the Laviron equation, $I_{p,r} = (nFQv) / (4RT)$, where $I_{p,r}$ is reduction peak current, v is the scan rate, Q is the charge of an electron, and F is faraday constant [148]. Therefore, for the redox reaction of immobilized MP-11, the CVs in Figure 4.14 yield a value of $n = 1.09$, which is consistent with the single electron transfer process of $Fe^{3+} + e^- \rightleftharpoons Fe^{2+}$. The electrode's surface coverage by the MP-11 molecule, Γ, can be estimated by $\Gamma = (4I_{p,r}RT) / (n^2F^2Av)$ [35]. Measuring the reduction peak height from the CV in Figure 4.14(a) obtained at a scan rate of 100 mV/s and using an area of 1 mm^2 for the electrode surface area A, Γ was estimated to be 4.7266×10^{-11} mol/cm^2. Since the size of MP-11 is approximately 2.5 nm × 1.3 nm × 1.5 nm [89], the value of Γ corresponds to a monolayer.

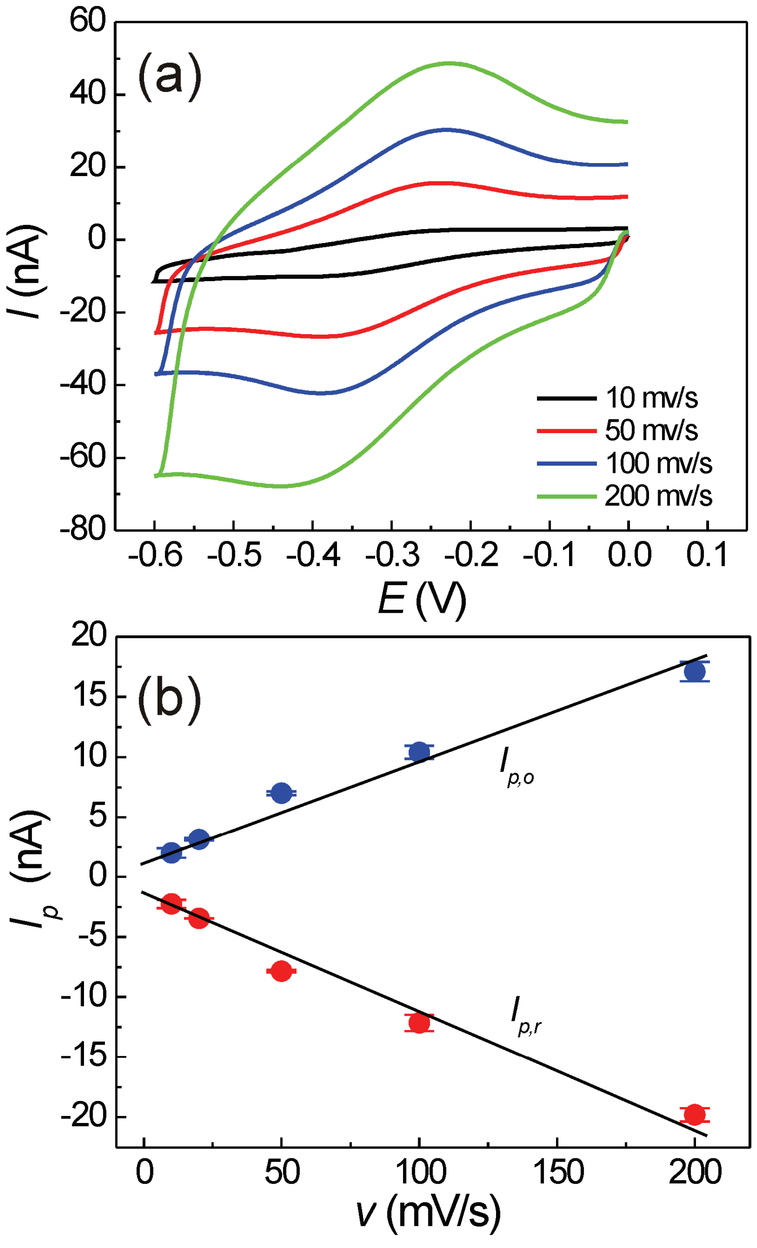

Figure 4.14 Electrochemical characterization of MP-11 immobilized electrode (a) CVs of MP-11 immobilized on the HOPG electrode obtained at different potential scan rates in 100 mM PBS at pH 7. (b) Plot of $I_{p,o}$ and $I_{p,r}$ on the potential scan rates from 10 to 200 mV/s. The peak currents show a linear dependence on the scan rate, indicating that the MP-11 molecules that were communicating electrically with the electrode were immobilized on the electrode

The effect of applying V_G on the bio-catalytic system of MP-11 and H_2O_2 is shown in Figure 4.15. Figure 4.15(a) shows the bio-catalytic activities of a MP-11-immobilized electrode for H_2O_2 in the absence and presence V_G. The black CV shows the electrode's behavior in the absence of H_2O_2 and V_G. The bio-catalytic nature of the electrode to H_2O_2 is reflected in the green CV, which was obtained in 20 μM of H_2O_2. The CV shows a large increase in the cathodic current, which is indicative of the reduction of H_2O_2 to water [147]. When V_G was turned on, the reduction current further increased as reflected in the blue and red CVs. This effect is consistent with Figure 4.12(b) and the discussion above on the reduced effective tunnel barrier height using a field.

The dependence of the reduction peak current $I_{p,r}$ on V_G at different concentrations of H_2O_2 was measured and is displayed in Figure 4.15(b). It is obvious that, at a given H_2O_2 concentration, increasing V_G causes $I_{p,r}$ to increase. Thus, Figure 4.15(b) shows the effect of voltage-controlled current amplification in the bio-catalytic process. Figure 4.15(c) shows the measured dependence of $I_{p,r}$ on H_2O_2 concentration for different values of V_G. The black curve is the electrode's intrinsic calibration curve for H_2O_2. It shows a linear dependence for low concentrations (10 ~ 50 mM) and a transition toward saturation at higher concentrations. This behavior indicates the Michaelis-Menten kinetics of the reduction process. The other curves obtained with non-zero V_G follow the same behavior with downward shifts.

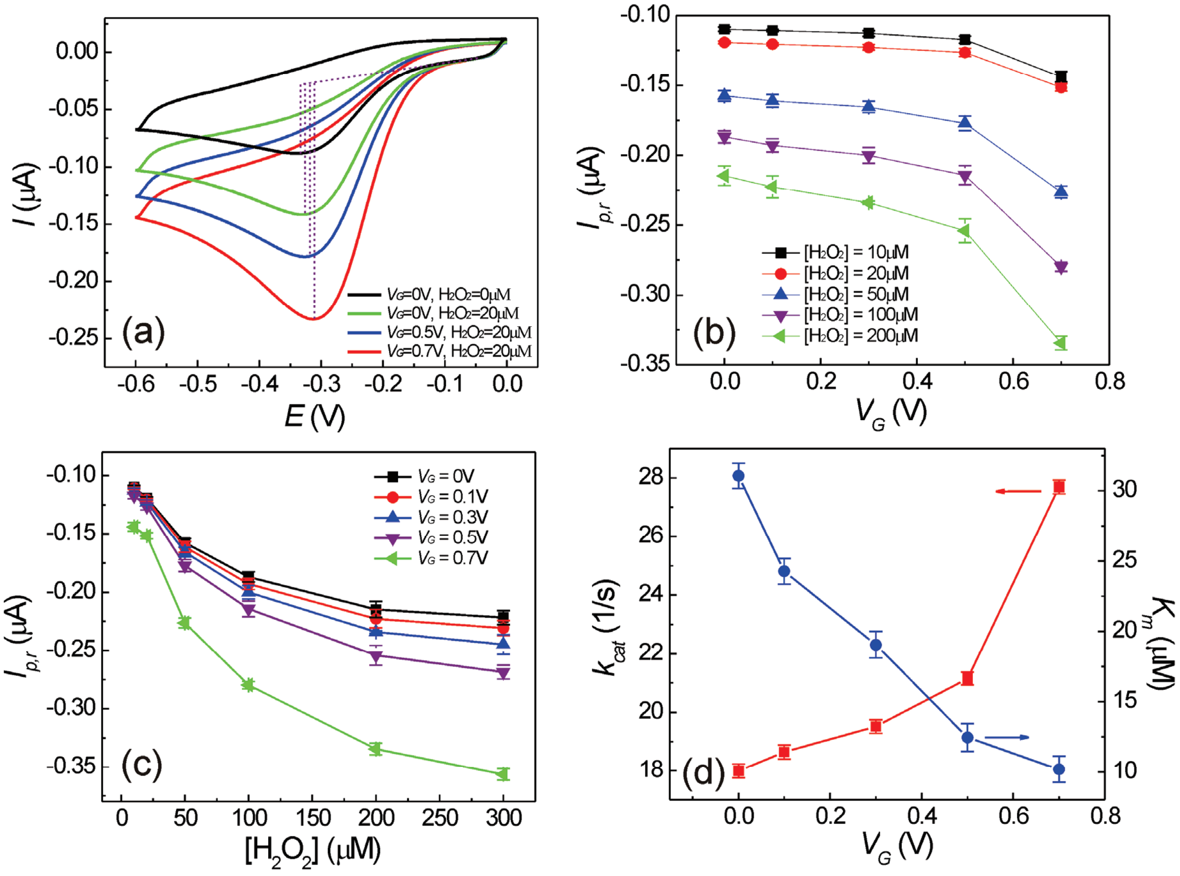

Figure 4.15 The effect of V_G on the reduction of H_2O_2 catalyzed by MP-11. (a) CVs of immobilized MP-11 were obtained in 100 mM PBS at pH 7 under different conditions. (b) The dependence of $I_{p,r}$ on V_G for different H_2O_2 concentrations. (c) The H_2O_2 calibration curves of the MP-11-immobilized electrode for different value of V_G. (d) The dependences of K_m and k_{cat} on V_G

To gain insight into the observed effect of V_G on the reduction reaction of H_2O_2, an investigation on the kinetic properties of the reaction has been made. The kinetics of the bio-catalytic conversion occurring at the electrode can be characterized using two parameters, namely, k_{cat} and K_m, where k_{cat}, the turnover rate constant, is the maximum number of H_2O_2 molecules that can be converted to water per second per active site and K_m is the Michaelis constant, which is the H_2O_2 concentration required for effective catalysis to occur [149]. A low K_m indicates high bio-catalytic efficiency for the reduction of H_2O_2 [149,150]. The reduction peak current, $I_{p,r}$, is given in terms of k_{cat} and K_m by the Lineweaver-Burk (LB) equation [60],

$$1 / I_{p,r} = \{K_m / (nFAk_{cat}\Gamma[H_2O_2]) + 1 / (nFAk_{cat}\Gamma)\} \tag{4.2}$$

The equation shows that $1 / I_{p,r}$ has a linear dependence on $1 / [H_2O_2]$. Therefore, k_{cat} and K_m can be determined from the slope and the vertical intercept of the plot of the equation. These parameters in the presence of V_G are evaluated using the curves in Figure 4.15(c) and are shown in Figure 4.15(d). Figure 4.15(d) shows that k_{cat} increases and K_m decreases as V_G is increased. In general, a bio-catalytic reaction is described as $E + S \underset{k_{-1}}{\overset{k_1}{\rightleftharpoons}} ES \xrightarrow{k_2} E + P$, where E is the enzyme (or the catalyst), S the substrate, ES the enzyme-substrate complex and P the product, the second step is the catalytic step, in which the product is formed and the enzyme returns to its original state. Figure 4.15(d) shows that increasing V_G results in a faster conversion process from H_2O_2 to water for a MP-11 molecule. This is because electrons are required to initiate the second step. Therefore, an increased k_{et} at the MP-electrode interface results in a higher k_{cat} ($=k_2$) so that more water molecules are produced and the MP-11 molecule returns to its original state more quickly to be available for the next conversion process. In Figure 4.15(d), k_{cat} shows a faster increase starting at V_G = 0.5 V, indicating a nonlinear dependence on V_G. This nonlinearity is likely to be the result of the exponential dependence of k_{et} on β as shown in Equation 4.1. The voltage-enhanced reaction kinetics is qualitatively supported by the behavior of K_m as shown in Figure 4.15(d), where K_m decreases as V_G is increased, indicating higher bio-catalytic efficiency. Compared to k_{cat}, K_m shows a mild nonlinearity. Since K_m describes the entire bio-catalytic reaction, i.e. K_m depends on $k_{\pm 1}$ and k_2, the dissociation of ES to E and S (to MP-11 and H_2O_2) may be the cause for the mild nonlinearity.

The results described in this section show that the reduction of H_2O_2 to water catalyzed by MP-11 immobilized on an electrode can be controlled by applying the voltage V_G to the immobilized MP-11. In fact, the experimental setup illustrates the operation of a field-effect bio-catalytic transistor, in which the current-generating mechanism is the conversion of the analyte to the product. The most important observation of this work is that the kinetic parameters of the conversion process can be controlled using an external voltage V_G. We have observed a nonlinear dependence of the kinetic parameters on V_G due to the controlled interfacial electron transfer by V_G. The nonlinearity indicates the feasibility of effective controlling the efficiency of a bio-catalytic reaction or a conversion process using the voltage.

Chapter 5 Conclusions

Recent advances in nanotechnology have made it possible to produce varieties of nanoscale materials with novel properties and manipulate the properties of nanoscale materials, the proper utilization of which may provide solutions to the present pressing issues in energy and health. This dissertation demonstrates that ultrasmall colloidal silicon nanoparticles, a novel nanoscale material, behave as electrocatalysts for the electro-oxidation of renewable fuels such ethanol, methanol and glucose. The catalysis shows features that have not been observed in the conventional catalysis using platinum as catalyst. The prototype fuel cells constructed utilizing the particles as the anode catalyst indicate the potential of using the particles in fuel cell applications.

Further investigations on the catalytic property of the particles remain for the future. First of all, composite materials consisted of the particles and other nano materials such as carbon nanotubes [33] and an electrode on which the particles are entrapped with various conducting polymer [27] are suggested to enhance the catalytic activities of the particles. Second of all, studies of electrocatalytic activities of the particles to the biologically important substances including DNA [151], lactate [152], nitric oxide [153], neurotransmitter (dopamine, epinephrine, norepinephrine) [22,23], DJ-1 protein (Parkinson's disease) [154], ketones (diabetes : acetoacetate, beta-hydroxybutyrate, acetone) [155] , HbA1c (diabetes) [156] and amyloidogenic proteins (Alzheimers's disease) [157] are mainly suggested for the biomedical applications. Third of all, investigation on the reduction activities of the particles to oxygen is very important for the fuel cell application due to slow speed of oxygen reduction using Pt [17]. Lastly, study for light dependency of the particles may provide an enhanced performance of sensors and fuel cells construed using the particles as the catalyst.

This dissertation also shows a technique for controlling the properties of nanoscale biological systems. As a new technique for detection of biomolecules and manipulation of reaction kinetics of biomolecular system, a field-effect bio-catalytic transistor is demonstrated. The transistor shows operations of ultra-sensitive, highly-selective and fast-responsive bio-detection for extremely low concentration of the analyte and current generation of the conversion of the analyte to the product.

Ultra-sensitive bio-detection techniques for the detection of extremely low analyte concentration have been intensively studied for many areas such as biomedical and environmental applications [55]. Our technique can be directly applied to the study of Alzheimer's disease [4,157], Parkinson's disease [154], diabetes [155], bioassay of antibodies [5], and environmentally important substances including oxygen, carbon dioxide, acidity, salinity, nitrate, calcium and fluoride [113]. Furthermore, an polarized gate electrode in the detection setup can be integrated with microfluidic systems (biochips and biosensors) based on Micro-Electro-Mechanical Systems (MEMS) technology which handle nano and pico liter volumes of sample so that the integrated system is able to detect extremely small amount of analyte in the sample and therefore to diagnose many diseases. In addition, as an effective parameter in the catalysis reaction of the biological system, the technique can be used for studying the mechanism of enzyme catalysis in which the rate of the reaction is determined by the barrier of the reaction heights [136]. The long-range electron tunneling mechanism in many biological oxidation-reduction systems can be investigated by controlling the electron tunneling and reaction kinetics of the system [50].

References

1 Xia, Y. *et al.* One-Dimensional Nanostructures: Synthesis, Characterization, and Applications. *Adv. Mater.* **15**, 353-389 (2003).

2 Whitesides, G. M. The 'right' size in nanobiotechnology. *Nat. Biotechnol.* **21**, 1161-1165 (2003).

3 Rolison, D. R. Catalytic nanoarchitectures - the importance of nothing and the unimportance of periodicity. *Science* **299**, 1698-1701 (2003).

4 Georganopoulou, D. G. *et al.* Nanoparticle-based detection in cerebral spinal fluid of a soluble pathogenic biomarker for Alzheimer's disease. *Proc. Natl. Acad. Sci. U.S.A.* **102**, 2273–2276 (2005).

5 Yu, F., Persson, B., Lofas, S. & Knoll, W. Attomolar sensitivity in bioassays based on surface plasmon fluorescence spectroscopy. *J. Am. Chem. Soc.* **126**, 8902-8903 (2004).

6 Mano, N. & Heller, A. Detection of glucose at 2 fM concentration. *Anal. Chem.* **77**, 729-732 (2005).

7 Shipp, G. Ultrasensitive Measurement of Protein and Nucleic Acid Biomarkers for Earlier Disease Detection and More Effective Therapies. *Biotech. Healthcare*, 35-40 (2006).

8 Iwasita, T. in *Handbook of Fuel Cells- Funfamentals, Technology and Applications* Vol. 2 eds W. Vielstich, H. A. Gasteiger, & A. Lamm) 603-624 (John Wiley & Sons, 2003).

9 Wang, H., Jusys, Z. & Behm, R. J. Ethanol Electrooxidation on a Carbon-Supported Pt Catalyst: Reaction Kinetics and Product Yields *J. Phys. Chem. B* **108**, 19413-19424 (2004).

10 Cohen, J. L., Volpe, D. J. & Abruna, H. D. Electrochemical determination of activation energies for methanol oxidation on polycrystalline platinum in acidic and alkaline electrolytes. *Phys. Chem. Chem. Phys.* **9**, 49–77 (2007).

11 Tripkovic, A. V. *et al.* Methanol electrooxidation on supported Pt and PtRu catalysts in acid and alkaline solutions. *Electrochim. Acta* **47**, 3707-3714 (2002).

12 Vielstich, W., Gasteiger, H. A. & Lamm, A. *Handbook of fuel cells - fundamentals, technology and applications*. Vol. 2 (John Wiley & Sons, 2003).

13 Jusys, Z., Kaiser, J. & Behm, R. J. Composition and activity of high surface area PtRu catalysts towards adsorbed CO and methanol electrooxidation. *Electrochim. Acta* **47**, 3693-3706 (2002).

14 Shao, Z.-G., Zhu, F., Lin, W.-F., Christensen, P. A. & Zhang, H. PtRu/Ti anodes with varying Pt:Ru ratio prepared by electrodeposition for the direct methanol fuel cell. *Phys. Chem. Chem. Phys.* **8**, 2720-2726 (2006).

15 Wang, H., Jusys, Z. & Behm, R. J. Ethanol electro-oxidation on carbon-supported Pt, PtRu and Pt_3Sn catalysts: A quantitative DEMS study. *J. Power Sources* **154**, 351–359 (2006).

16 Chalk, S. G. & Miller, J. F. Key challenges and recent progress in batteries, fuel cells, and hydrogen storage for clean energy systems. *J. Power Sources* **159**, 73-80 (2006).

17 Bashyam, R. & Zelenay, P. A class of non-precious metal composite catalysts for fuel cells. *Nature* **443**, 63-66 (2006).

18 Appleby, A. J. Electrocatalysis of aqueous dioxygen reduction. *J. Electroanal. Chem.* **357**, 117-179 (1993).

19 Wang, B. Recent development of non-platinum catalysts for oxygen reduction reaction. *J. Power Sources* **152**, 1-15 (2005).

20 Liu, S.-Q., Xu, J.-Q., Sun, H.-R. & Li, D.-M. Meso-Tetrakis(4-Nbenzylpyridyl)-porphyrin and its supramolecular complexes formed with anionic metal-oxo cluster: spectroscopy and electrocatalytic reduction of dioxygen. *Inorg. Chim. Acta* **306**, 87-93 (2000).

21 Xiao, Y. & Li, C. M. Nanocomposites: From Fabrications to Electrochemical Bioapplications. *Electroanalysis* **20**, 648-662 (2008).

22 Tu, X., Xie, Q., Jiang, S. & Yao, S. Electrochemical quartz crystal impedance study on the overoxidation of polypyrrole-carbon nanotubes composite film for amperometric detection of dopamine *Biosens. Bioelectron.* **22**, 2819-2826 (2007).

23 Selvaraju, T. & Ramaraj, R. Electrochemically deposited nanostructured platinum on Nafion coated electrode for sensor applications. *J. Electroanal. Chem.* **585**, 290-300 (2005).

24 Wang, J. Carbon-Nanotube Based Electrochemical Biosensors: A Review. *Electroanalysis* **17**, 7-14 (2005).

25 Wu, J., Suls, J. & Sansen, W. The glucose sensor integratable in the microchannel. *Sens. Actuators, B* **78**, 221-227 (2001).

26 Merchant, S. A. *et al.* High-Sensitivity Amperometric Biosensors Based on Ferrocene-Modified Linear Poly(ethylenimine). *Langmuir* **25**, 7736-7742 (2009).

27 Wang, K., Xu, J.-J., Sun, D.-C., Wei, H. & Xia, X.-H. Selective glucose detection based on the concept of electrochemical depletion of electroactive species in diffusion layer. *Biosens. Bioelecron.* **20**, 1366-1372 (2005).

28 Wu, B.-Y. *et al.* Amperometric glucose biosensor based on layer-by-layer assembly of multilayer films composed of chitosan, gold nanoparticles and glucose oxidase modified Pt electrode. *Biosens. Bioelecron.* **22**, 838-844 (2007).

29 Xiao, Y., Patolsky, F., Katz, E., Hainfeld, J. F. & Willner, I. “Plugging into Enzymes”:Nanowiring of Redox Enzymes by a Gold Nanoparticle. *Science* **299**, 1877-1881 (2003).

30 Huang, Y., Zhang, W., Xiao, H. & Li, G. An electrochemical investigation of glucose oxidase at a CdS nanoparticles modified electrode. *Biosens. Bioelecron.* **21**, 817-821 (2005).

31 Zhang, S., Wang, N., Yu, H., Niu, Y. & Sun, C. Covalent attachment of glucose oxidase to an Au electrode modified with gold nanoparticles for use as glucose biosensor. *Bioelectrochemistry* **67**, 15-22 (2005).

32 Deng, L. *et al.* Electrochemiluminescence detection of NADH and ethanol based on partial sulfonation of sol–gel network with gold nanoparticles. *Biosens. Bioelecron.* **24**, 2273-2276 (2009).

33 Patolsky, F., Weizmann, Y. & Willner, I. Long-Range Electrical Contacting of Redox Enzymes by SWCNT Connectors. *Angew. Chem. Int. Ed.* **43**, 2113-2117 (2004).

34 Wang, J. & Musameh, M. A Reagentless Amperometric Alcohol Biosensor Based on Carbon-Nanotube/Teflon Composite Electrodes. *Anal. Lett.* **36**, 2041-2048 (2003).

35 Bard, A. J. & Faulkner, L. R. *Electrochemical Methods*. 2 edn, (John Wiley & Sons, 2001).

36 Kemp, T. J. *Instrumental methods in electrochemistry*. (Ellis horwood limited, 1985).

37 Schoning, M. J., Gluck, O. & Thust, M. in *Measurement, instrumentation, and sensors* (ed John G. Webster) Ch. 70, (CRC Press, 1998).

38 Saveant, J.-M. *Elements of Molecular and Biomolecular Electrochemistry*. (John Wiley & Sons, 2006).

39 Fowler, R. H. & Nordheim, L. Electron Emission in Intense Electric Fields. *Proc. R. Soc.* **119**, 173-181 (1928).

40 Choi, Y., Wang, G. & Yau, S.-T. Electronic composite of sulfonated tetrafluorethylene copolymer with potassium ferricyanide exhibiting room-temperature negative differential resistance. *Appl. Phys. Lett.* **89**, 233116 (2006).

41 Fujimaru, K. & Matsumura, H. Theoretical consideration of a new nanometer transistor using metal/insulator tunnel-junction. *Jpn. J. Appl. Phys.* **35**, 2090-2094 (1996).

42 Fujimaru, K., Sasajima, R. & Matsumura, H. Nanoscale metal transistor control of Fowler-Nordheim Tunneling currents through 16 nm insulating channel. *J. Appl. Phys.* **9**, 6912-6916 (1999).

43 Simmons, J. G. Generalized formula for the electric tunnel effect between similar electrodes separated by a thin inulating film. *J. Appl. Phys.* **34**, 1793-1803 (1963).

44 Fujimaru, K. & Matsumura, H. Theoretical consideration of a new nanomber transistor using metal/insulator tunnel-junction. *Jpn. J. Appl. Phys.* **35**, 2090-2094 (1996).

45 Snow, E. S. *et al.* A metal/oxide tunneling transistor. *Appl. Phys. Lett.* **72**, 3071-3073 (1998).

46 Moser, C. C., Keske, J. M., Warncke, K., Farid, R. S. & Dutton, P. L. Nature of biological electron transfer. *Nature* **355**, 196-802 (1992).

47 Beratan, D. N., Onuchic, J. N., Winkler, J. R. & Gray, H. B. Electron-tunneling pathways in proteins. *Science* **258**, 1740-1741 (1992).

48 Davidson, V. L. Chemically Gated Electron Transfer. A Means of Accelerating and Regulating Rates of Biological Electron Transfer. *Biochemistry* **41**, 14633-14636 (2002).

49 Barton, S. C., Gallaway, J. & Atanassov, P. Enzymatic Biofuel Cells for Implantable and Microscale Devices. *Chem. Rev.* **104**, 4867-4886 (2004).

50 Page, C. C., Moser, C. C., Chen, X. & Dutton, P. L. Natural engineering principles of electron tunnelling in biological oxidation-reduction. *Nature* **402**, 47-52 (1999).

51 Marcus, R. A. & Sutin, N. Electron transfer in chemistry and biology. *Biochim. Biophys. Acta* **811**, 265-322 (1985).

52 Smalley, J. F. *et al.* The kinetics of electron transfer through ferrocene-terminated alkanethiol monolayers on gold. *J. Phys. Chem.* **99**, 13141-13149 (1995).

53 Pande, V. S. & Onuchic, J. N. Electron Transport in Disordered Polymeric and Biological Systems. *Phys. Rev. Lett.* **78**, 146-149 (1997).

54 Mann, B. & Kuhn, H. Tunneling through Fatty Acid Salt Monolayers. *J. Appl. Phys.* **42**, 4398-4405 (1971).

55 Eggins, B. R. *Chemical sensors and biosensors*. (John Wiley & Sons, 2002).

56 Wilner, I. & Katz, E. *Bioelectronics*. (Wiley-VCH Verlag, 2005).

57 Willner, I., Katz, E., Patolsky, F. & Buckmann, A. F. Biofuel cell based on glucose oxidase and microperoxidase-11 monolayer-fundionalized electrodes. *J. Chem. Soc., Perkin Trans. 2*, 1817-1822 (1998).

58 Bertini, I., Sigel, A. & Sigel, H. *Handbook on metalloproteins*. (Marcel Dekker, 2001).

59 Voet, D. J. & Voet, J. G. *Biochemistry*. 2 edn, (Wiley, 1995).

60 Kumar, A. S. & Zen, J.-M. Electrochemical Investigation of Glucose Sensor Fabricated at Copper-Plated Screen-Printed Carbon Electrodes. *Electroanalysis* **14**, 671-678 (2002).

61 Lamy, C. & Belgsir, E. M. *Handbook of Fuel Cells - Fundamentals, Technology and Applications*. Vol. 1 (John Wiles & Sons, 2003).

62 Katz, E., Willner, I. & Kotlyar, A. B. A non-compartmentalized glucose vertical bar O-2 biofuel cell by bioengineered electrode surfaces. *J. Electroanal. Chem.* **479**, 64-68 (1999).

63 Cracknell, J. A., Vincent, K. A. & Armstrong, F. A. Enzymes as working or inspirational electrocatalysts for fuel cells and electrolysis. *Chem. Rev.* **108**, 2439-2461 (2008).

64 Logan, B. E. *Microbial Fuel Cells*. (John Wiley & Sons, 2007).

65 Bockris, J. O. & Srinivasan, S. *Fuel Cells*. (McGraw-Hill, 1969).

66 Bullen, R. A., Arnot, T. C., Lakeman, J. B. & Walsh, F. C. Biofuel cells and their development. *Biosens. Bioelectron.* **21**, 2015-2045 (2006).

67 Choi, Y., Wang, G., Nayfeh, M. H. & Yau, S.-T. A Hybrid Biofuel Cell Based on Electrooxidation of Glucose Using Ultra-Small Silicon Nanoparticles. *Biosens. Bioelectron.* **24**, 3103-3107 (2009).

68 Malea, K. B., Hrapovic, S., Liu, Y., Wang, D. & Luonga, J. H. T. Electrochemical detection of carbohydrates using copper nanoparticles and carbon nanotubes. *Anal. Chim. Acta* **516**, 35-41 (2004).

69 Cuia, H.-F. *et al.* Selective and sensitive electrochemical detection of glucose in neutral solution using platinum–lead alloy nanoparticle/carbon nanotube nanocomposites. *Anal. Chim. Acta* **594**, 175-183 (2007).

70 Kundu, A. *et al.* Micro-fuel cells—Current development and applications. *J. Power Sources* **170**, 67–78 (2007).

71 Kamarudin, S. K., Daud, W. R. W., Ho, S. L. & Hasran, U. A. Overview on the challenges and developments of micro-direct methanol fuel cells (DMFC). *J. Power Sources* **163**, 743–754 (2007).

72 Calabrese-Barton, S., Gallaway, J. & Atanassov, P. Emzymatic biofuel cells for implantable and microscale devices. *Chem. Rev.* **104**, 4867-4886 (2004).

73 Holmes, C. F. Electrochemical power sources and the treatment of human illness. *Electrochem. Soc. Interface* **12**, 26-29 (2003).

74 Rauschecker, J. P. & Shannon, R. V. Sending sound to the brain. *Science* **295**, 1025-1029 (2002).

75 Maynard, E. M. Visual prostheses. *Ann. Rev. Biomed. Eng.* **3**, 145-168 (2001).

76 Linden, D. & Reddy, T. B. *Handbook of Batteries*. 3rd ed. edn, (McGraw-Hill, 2002).

77 CalabreseBarton, S., Gallaway, J. & Atanassov, P. Enzymatic Biofuel Cells for Implantable and Microscale Devices. *Chem. Rev.* **104**, 4867-4886 (2004).

78 Wang, G., Mantey, K., Nayfeh, M. H. & T., Y. S. Enhanced amperometric detection of glucose using Si29 particles. *Appl. Phys. Lett.* **89** (2006).

79 Choi, Y., Wang, G., Nayfeh, M. H. & Yau, S.-T. Electro-oxidation of organic fuels catalyzed by ultrasmall silicon nanoparticles. *Appl. Phys. Lett.* **93**, 164103 (2008).

80 Belomoin, G., Therrien, J. & Nayfeh, M. Oxide and hydrogen capped ultrasmall blue luminescent Si nanoparticles. *Appl. Phys. Lett.* **77**, 779-781 (2000).

81 Rao, S. *et al.* Excited states of tetrahedral single-core Si_{29} nanoparticles. *Phys. Rev. B* **69**, 205319 (2004).

82 Nayfeh, M. H. *et al.* Second harmonic generation in microcrystallite films of ultrasmall Si nanoparticles. *Appl. Phys. Lett.* **77**, 4086-4088 (2000).

83 Nayfeh, M. H. *et al.* Observation of laser oscillation in aggregates of ultrasmall silicon nanoparticles. *App. Phys.Lett.* **80**, 121-123 (2002).

84 Hecht, H. J., Kalisz, H. M., Hendle, J., Schmid, R. D. & Schomburg, D. Crystal structure of glucose oxidase from aspergillus niger refined at 2.3 A resolution. *J. Mol. Biol.* **229**, 153-172 (1993).

85 Swoboda, B. E. P. & MASSEY, P. Purification and Properties of the Glucose Oxidase from Aspergillus niger. *J. Bio. Chem.* **240**, 2209-2215 (1965).

86 Wilson, R. & Turner, A. P. F. Glucose oxidase: An ideal enzyme. *Biosens. Bioelectron.* **7**, 165-185 (1992).

87 Maehly, A. in *Methods in Enzymology* Vol. 2 eds S. Colowick & N. Kaplan) (Academic Press, 1955).

88 Andreu, R., Ferapontova, E. E., Gorton, L. & Calvente, J. J. Direct electron transfer kinetics in horseradish peroxidase electrocatalysis. *J. Phys. Chem. B* **111**, 469-477 (2007).

89 Luo, Y. & Brayer, G. V. The Research Collabotatory for Structural Bioinformatics PDB. *J. Mol. Biol.* **214**, 585-595 (1990).

90 Turano, P. & Lu, Y. in *Handbook on Metalloproteins* eds Ivano Bertini, Astrid Sigel, & Helmut Sigel) (Marcel Dekker, 2001).

91 *HRP*, <http://chem.ps.uci.edu/~pfarmer/127i/hemepr.html>.

92 *HEME*, <http://en.wikipedia.org/wiki/Heme>.

93 Sanjoh, A., Tsukiharaa, T. & Gorti, S. Surface-potential controlled Si-microarray devices for heterogeneous protein crystallization screening *J. Cryst. Growth* **232**, 618 (2001).

94 Strauss, E., Thomas, B. & Yau, S.-T. Enhancing electron transfer at the cytochrome c – immobilized microelectrode and macroelectrode. *Langmuir* **20**, 8768-8772 (2004).

95 Armstrong, F. A., Bond, A. M., Hill, H. A. O., Psalti, I. S. M. & Zoski, C. G. A microscopic model of electron transfer at electroactive sites of molecular dimensions for reduction of cytochrome c at basal- and edge-plane graphite electrodes. *J. Phys. Chem.* **93**, 6485-6493 (1989).

96 Wang, G., Thai, N. M. & Yau, S.-T. Preserved enzymatic activity of glucose oxidase immobilized on an unmodified electrode. *Electrochem. Comm.* **8**, 987–992 (2006).

97 Kumar, A. S. & Zen, J.-M. Unusual Redox Catalysis in a Ruthenium Oxide-Prussian Blue Combined Material. *ChemPhysChem* **5**, 1227-1231 (2004).

98 Slade, S., Campbell, S. A., Ralph, T. R. & Walshc, F. C. Ionic Conductivity of an Extruded Nafion 1100 EW Series of Membranes. *J. Electrochem. Soc.* **149**, A1556-A1564 (2002).

99 Kokoh, K. B., Leger, J.-M., Benden, B. & Lamy, C. "On-Line" chromatographic analysis of the products resulting form the electrocatalytic oxidation d-glucose on Pt, Au, and adatoms modified Pt electrode Part I. *Electrochim. Acta* **37**, 1333-1342 (1992).

100 Biswa, P. C. & Enyo, M. Electro-oxidation of methanol on graphite-supported perovskite-modified Pt electrodes in alkaline solution. *J. Electroanal. Chem.* **322**, 203-220 (1992).

101 Vigier, F., Coutanceau, C., Perrard, A., Belgsir, E. M. & Lamy, C. Development of anode catalysts for a direct ethanol fuel cell. *J. Appl. Electrochem.* **34**, 439-446 (2004).

102 Therrien, J. Size dependence of the electrical characteristics of silicon nanoparticles. *Ph. D. Dissertation, University of Illionis* (2002).

103 Mathews, C. K., Hold, K. E. v. & Ahern, K. G. *Biochemistry*. 3rd ed. edn, (Addison Wesley Longman, Inc., 2000).

104 Markovic, N. M., Schmidt, T. J., Stamenkovic, V. & Ross, P. N. Oxygen Reduction Reaction Pt and Pt Bimetallic Surfaces:A Selective Review. *Fuel cells* **1**, 105-116 (2001).

105 Li, X. *Principles of Fuel Cells*. 1st edn, (Taylor & Francis, 2006).

106 Mano, N., Mao, F. & Heller, A. A miniature biofuel cell operating in a physiological buffer. *J. Am. Chem. Soc.* **124**, 12962-12963 (2002).

107 Mueller, S., Riedel, H.-D. & Stremmel, W. Determination of Catalase Activity at Physiological Hydrogen Peroxide Concentrations. *Aanl. Biochem.* **245**, 55-60 (1997).

108 Ramanavicius, A., Kausaite, A. & Ramanavicius, A. Biofuel cell based on direct bioelectrocatalysis. *Biosens. Bioelectron.* **20**, 1962-1967 (2005).

109 Barton, S. C., Gallaway, J. & Atanassov, P. Enzymatic Biofuel Cells for Implantable and Microscale Devices. *Chem. Rev.* **104**, 4867-4886 (2004).

110 Drillet, J.-F. *et al.* Oxygen reduction at Pt and $Pt_{70}Ni_{30}$ in H_2SO_4/CH_3OH solution. *Electrochim. Acta* **47**, 1983-1988 (2002).

111 Habrioux, A. *et al.* Activity of platinum-gold alloys for glucose electrooxidation in biofuel cells. *J. Phys. Chem. B* **111**, 10329-10333 (2007).

112 Katz, E., Filanovsky, B. & Willner, I. A biofuel cell based on two immiscible solvents and glucose oxidase and microperoxidase-11 monolayer-functionalized electrodes. *New J. Chem.* **5**, 481-487 (1999).

113 Behnisch, P. A. Biodetectors in environmental chemistry - Are we at a turning point? *Environ. Int.* **27**, 441-442 (2001).

114 Gooding, J. J., Praig, V. G. & Hall, E. A. H. Platinum-Catalyzed Enzyme Electrodes Immobilized on Gold Using Self-Assembled Layers. *Anal. Chem.* **70**, 2396-2402 (1998).

115 Zhang, L., Xu, Z., Sun, X. & Dong, S. A novel alcohol dehydrogenase biosensor based on soild-state electrogenerated chemiluminescence by assembling dehydrogenase to $Ru(bpy)_3^{2+}$-Au nanoparticles aggregates. *Biosens. Bioelecron.* **22**, 1097-1100 (2007).

116 Bergveld, P. & Sibbald, A. *Analytical and Biomedical Aplications of Ion-Selective Field-Effect Transistors*. (Elsevier, 1988).

117 Yao, K., Zhu, Y., Yang, X. & Li, C. ENFET glucose biosensor produced with dendrimer encapsulated Pt nanoparticles. *Mat. Sci. Eng. C* **28**, 1236-1241 (2008).

118 Wang, X., Chen, Y., Gibney, K. A., Erramilli, S. & Mohnty, P. Silicon based nanochannel glucose sensor. *Appl. Phys. Lett.* **92**, 013903 (2008).

119 Pogorelova, S. P. *et al.* Analysis of NAD(P)$^+$/NAD(P)H Cofactors by Imprinted Polymer Membranes Associated with Ion-Sensitive Field-Effect Transistor Devices and Au-Quartz Crystals. *Anal. Chem.* **75**, 509-517 (2003).

120 Anh, D. T. V., Olthuis, W. & Bergveld, P. Electroactive Gate Materials for a Hydrogen Peroxide Sensitive ^{E}MOSFET. *IEEE Sens. J.* **2**, 26-33 (2002).

121 Sund, H. & Theorell, H. in *The Enzymes* Vol. VII eds P. Boyer, B.Nardy, & K. Myrback) (Academic Press, 1963).

122 Christie, S. M. H., Kenner, G. W. & Todd, A. R. Total Synthesis of Flavin-adenine-dinucleotide. *Nature* **170**, 924 (1952).

123 Bourdillon, C., Demaille, C., Moiroux, J. & Saveant, J. M. New insights into the enzymic catalysis of the oxidation of glucose by native and recombinant glucose oxidase mediated by electrochemically generated one-electron redox cosubstrates. *J. Am. Chem. Soc.* **115**, 2-10 (1993).

124 Zayats, M., Katz, E. & Willner, I. Electrical Contacting of Glucose Oxidase by Surface-Reconstitution of the Apo-Protein on a Relay-Boronic Acid-FAD Cofactor Monolayer. *J. Am. Chem. Soc.* **124**, 2120-2121 (2002).

125 Yan, Y.-M., Yehezkeli, O. & Willner, I. Integrated, Electrically Contacted NAD(P) Dependent Enzyme–Carbon Nanotube Electrodes for Biosensors and Biofuel Cell Applications. *Chem. Eur. J.* **13**, 10168-10175 (2007).

126 Tao, N. J. Probing Potential-Tuned Resonant Tunneling through Redox Molecules with Scanning Tunneling Microscopy. *Phys. Rev. Lett.* **76**, 4066-4069 (1996).

127 *ADH*, <http://www.rcsb.org/pdb/explore.do?structureId=1HLD>.

128 *FAD*, <http://en.wikipedia.org/wiki/FAD>.

129 *NAD*, <http://en.wikipedia.org/wiki/NADH>.

130 Csoregi, E., GAspAr, S., Niculescu, M., Mattiasson, B. & Schuhmann, W. in *Physics and Chemistry of Biotechnology* Vol. 7 eds M. De Cuyper & J. W. M. Bulte) 105-130 (Springer, 2001).

131 Tans, S. J., Verschueren, A. R. M. & Dekker, C. Room-temperature transistor based on a single carbon nanotube. *Nature* **393**, 49-52 (1998).

132 Yau, S.-T. & Qian, G. A prototype protein field-effect transistor. *Appl. Phys. Lett.* **86**, 103508 (2005).

133 Manso, J., Mena, M. L., Yanez-Sedeno, P. & M., P. J. Alcohol dehydrogenase amperometric biosensor based on a colloidal gold-carbon nanotubes composite electrode. *Electrochim. Acta* **53**, 4007-4012 (2008).

134 Ernst, H., Rob, B. & Knoll, M. Reliable glucose monitoring through the use of microsystem technology. *Anal. Bioanal. Chem.* **373**, 758–761 (2002).

135 Choi, Y. & Yau, S.-T. Field-Effect Enzymatic Amplifying Detector with Picomolar Detection Limit. *Anal. Chem.* **81**, 7123-7126 (2009).

136 Hay, S. *et al.* Barrier Compression Enhances an Enzymatic Hydrogen-Transfer Reaction. *Angew. Chem. Int. Ed.* **48**, 1452-1454 (2009).

137 Christison, G. B. & MacKenzie, H. A. Laser photoacoustic determination of physiological glucose concentrations in human whole blood. *Med. Boil. Eng. Comp.* **31**, 284-290 (1993).

138 Salusjarvi, T., Kalkkinen, N. & Miasnikov, A. N. Cloning and Characterization of Gluconolactone Oxidase of Penicillium cyaneo-fulvum ATCC 10431 and Evaluation of Its Use for Production of D-Erythorbic Acid in Recombinant Pichia pastoris. *Appl. Environ. Microbiol.* **70**, 5503-5510 (2004).

139 Tominaga, M., Shimazoe, T., Nagashima, M. & Taniguchi, I. Electrocatalytic oxidation of glucose at gold nanoparticle-modified carbon electrodes in alkaline and neutral solutions. *Electrochem. Comm.* **7**, 189-193 (2005).

140 Zhang, Z. *et al.* Lactonization and Protonation of Gluconic Acid: A Thermodynamic and Kinetic Study by Potentiometry, NMR and ESI-MS. *J. Solution Chem* **36**, 1187-1200 (2007).

141 Ballardini, R., Balzani, V., Credi, A., Gandolfi, M. T. & Venturi, M. Artificial Molecular-Level Machines: Which Energy To Make Them Work? *Acc. Chem. Res.* **34**, 445-455 (2001).

142 Maconi, E., Griffini, A., Cavazzoni, V. & Aragozzini, F. Reduction of acetaldehyde to ethanol by some micro-organisms and its stereospecificity. *Biochem. J.* **250**, 929-932 (1988).

143 Onuchic, J. N., Kobayash, C., Miyashita, O., Jennings, P. & Baldridge, K. K. Exploring biomolecular machines: energy landscape control of biological reactions. *Phil. Trans. R. Soc. B* **361**, 1439–1443 (2006).

144 Nocek, J. M. *et al.* Theory and Practice of Electron Transfer within Protein-Protein Complexes: Application to the Multidomain Binding of Cytochrome c by Cytochrome c Peroxidase. *Chem. Rev.* **96**, 2459-2489 (1996).

145 Alcalde, M., Ferrer, M., Plou, F. J. & Ballesteros, A. Environmental biocatalysis: from remediation with enzymes to novel green processes. *Trends Biotechnol.* **24**, 281-287 (2006).

146 Shlgehara, K. & Anson, F. C. Electrocatalytic activity of three iron porphyrins in the reductions of dioxygen and hydrogen peroxide at graphite electrodes. *J. Phys. Chem.* **86**, 2776-2783 (1982).

147 Liu, Y. *et al.* Direct electron transfer and electrocatalysis of microperoxidase immobilized on nanohybrid film. *J. Electroanal. Chem.* **581**, 1-10 (2005).

148 Laviron, E. General expression of the linear potential sweep voltammogram in the case of diffusionless electrochemical systems. *J. Electroanal. Chem.* **101**, 19-28 (1979).

149 D. Voet, J. G. V. *Biochemistry*. 2 edn, (Wiley, 1995).

150 Kamin, R. A. & Wilson, G. S. Rotating ring-disk enzyme electrode for biocatalysis kinetic studies and characterization of the immobilized layer. *Anal. Chem.* **52**, 1198-1205 (1982).

151 Lellouche, J.-P. *et al.* Magnetically Responsive Carboxylated Magnetite-Polydipyrrole/Polydicarbazole Nanocomposites of Core-Shell Morphology. Preparation, Characterization, and Use in DNA Hybridization. *J. Am. Chem. Soc.* **127**, 11998-12006 (2005).

152 Zhiqiang, G. *et al.* Electrodeposition of Redox Polymers and Co-Electrodeposition of Enzymes by Coordinative Crosslinking. *Angew. Chem. Int. Ed.* **41**, 810-813 (2002).

153 Li, C. M. *et al.* Electrochemical Detection of Nitric Oxide on a SWCNT/RTIL Composite Gel Microelectrode. *Electroanalysis* **18**, 713-718 (2006).

154 Zhang, L. *et al.* Mitochondrial localization of the Parkinson's disease related protein DJ-1: implications for pathogenesis. *Hum. Mol. Genet.* **14**, 2063-2073 (2005).

155 Laffel, L. Ketone boides: a review of physiology, pathophysiology and application of monitoring to diabetes. *Diabetes Metab. Res. Rev.* **15**, 412-426 (1999).

156 Kim, K.-S., Kim, S.-K., Lee, Y.-K., Park, S.-W. & Cho, Y.-W. Diagnostic value of glycated haemoglobin (HbA1c) for the early detection of diabetes in high-risk subjects. *Diabet. Med.* **25**, 997-1000 (2008).

157 Herland, A. *et al.* Electroactive luminescent self-assembled bio-organic nanowires: integration of semiconducting oligoelectrolytes within amyloidogenic proteins. *Adv. Mater.* **17**, 1466-1471 (2005).